Trends in low-temperature fuel cell catalysis

A computational study

Tritsaris, Georgios

Publication date:
2011

Document Version
Early version, also known as pre-print

Thesis for the degree of Doctor of Philosophy in Physics

Trends in low-temperature fuel cell catalysis

A computational study

Georgios A. Tritsaris

Department of Physics
Technical University of Denmark
Lyngby, Denmark • 2011

Trends in low-temperature fuel cell catalysis - a computational study

Georgios A. Tritsaris
George.Tritsaris@fysik.dtu.dk

Supervisor: Jan Rossmeisl • Co-supervisor: Jens K. Nørskov

Center for Atomic-Scale Materials Design
Department of Physics
Technical University of Denmark

Lyngby, Denmark • February 2011

Part of the study was carried out at SLAC National Accelerator Laboratory, Stanford, US.

The *Neo Sans*™ font family by Monotype Imaging was used for the layout.

Abstract

Density functional theory simulations and theoretical materials modeling are used to study the electrochemical oxygen reduction and methanol oxidation reactions occurring on low-temperature fuel cell electrodes. Transition metal elemental and bimetallic alloys and transition metal chalcogenides are studied. Their electro-catalytic performance is evaluated in terms of activity, selectivity and stability. Atomistic models are constructed that describe flat and stepped surfaces, surface defects and nanoparticles.

The catalytic performance of transition metal surfaces modified with selenium and sulfur is evaluated for their use as cathode catalysts. The effect of the chalcogen on the catalytic performance is discussed. Trends in surface reactivity, stability and tolerance to methanol oxidation are identified. A descriptor of the catalytic activity is established, i.e. the adsorption energy of OH. Ruthenium selenium alloys are found to exhibit enhanced performance for the oxygen electro-reduction reaction compared to the unmodified ruthenium surfaces.

Transition metal based elemental surfaces and bimetallic alloys are evaluated as direct methanol fuel cell anode catalysts. Trends in surface reactivity are identified. The adsorption energies of CO and OH are used as reactivity descriptors. A procedure is developed for screening for bimetallic alloys of enhanced performance. Platinum copper alloys are suggested as promising electro-catalysts for the methanol oxidation reaction, which are found to outperform elemental platinum.

Particle size effects for the oxygen electro-reduction reaction on platinum nanoparticles are studied. A model for nanoparticle catalysts for fuel cells is developed, which accounts for surface irregularities. The model reproduces the experimentally observed trends in both the specific and mass activities. Mass activity is verified to be maximized for particles of a diameter in the range of 2-4nm in agreement with experiments.

Resume

Simuleringer med tætheds funktional teori og teoretiske modelleringer af materialer anvendes til at undersøge de elektrokemiske reaktioner af ilt reduktion og methanol oxidation, som foregår ved elektroderne af lav temperatur brændselsceller. Overflader af rene overgangsmetaller, samt legeringer af overgangsmetaller og overgangsmetal chalcogenides er undersøgt. Deres elektro-katalytiske egenskaber er vurderet ved henholdsvis deres aktivitet, selektivitet og stabilitet. Atomare modeller af overflader er konstrueret for at beskrive flade og under-koordinerede overflader, overflade defekter og nanopartikler.

Den katalytiske ydeevne for overflader af overgangsmetaller modificeret med selen og sulfur er evalueret for deres anvendelse som katode katalysatorer. Virkningen af chalcogen på katalytiske resultater er diskuteret. Tendenser i overflade-reaktivitet, stabilitet og tolerance over for methanol, er identificeret. En deskriptor af den katalytiske aktivitet er etableret, dvs. adsorptions energien af hydroxyl (OH). Rutenium selen legeringer, som har en forbedret aktivitet for den elektrokemiske reduktion af ilt i forhold til den umodificerede rutenium overflade.

Rene overgangsmetal overflader og legeringer af to overgangsmetaller er vurderet som katalysatorer for anoden i den direkte methanol brændselscelle. Tendenser i overflade reaktiviteten er identificeret, hvor adsorptions energierne af CO og OH anvendes som reaktivitet deskriptorer. En procedure er udviklet til screening for legeringer (af to overgangsmetaller) med forbedret ydeevne. Platin kobberlegeringer er foreslået som lovende electro-katalysatorer for methanol oxidationsreaktion, der er fundet til at overgå ren platin.

Virkningerne af partikelstørrelse er undersøgt for elektro-reduktions af ilt reaktionen på platin nanopartikler. En model for nanopartikle katalysatorer til brændselsceller er udviklet, som implementere uregelmæssigheder på overfladen. Den model gengiver eksperimentelt observerede tendenser for aktiviteten per aktive site og for aktiviteten per masse. Det er vist at masse aktiviteten er maksimal for partikler med en diameter i intervallet 2-4nm, som er i overensstemmelse med eksperimenter.

■ I am very thankful to Jakob Howalt for the translation of the abstract.

Acknowledgements

I thank my supervisors, Jan Rossmeisl and Jens K. Nørskov for the three years of support and guidance through the PhD labyrinth. They shared their knowledge with me and helped me to grow as a researcher. The collective consciousness of CAMd has been like a third supervisor to me. It taught me science and it has motivated me by keeping the standards high. Financial support by the International Graduate School of Science and Engineering (IGSEE) is acknowledged.

It has been a great pleasure collaborating with Jeff Greeley and Andreas Møgelhøj. I sincerely thank them for sharing their enthusiasm for research with me.

I am also grateful to Jens K. Nørskov for giving me the opportunity to spend three months in the SUNCAT group at Stanford. My stay there was a truly inspiring experience. A warm thanks to all the people in SUNCAT for their support in my applying for a postdoc position. Thank you for being there during the most stressful period of my PhD.

During my PhD, Office 259 has been the base of operations for my intellectual pursuits in science. I would like to thank all the people I shared it with through the years, Mikkel, Egill, Hai-Jan, Jón, Vladimir, Marco, Nonni and Jakob. I greatly enjoyed all our discussions on science and trivia.

Special thanks go to the IT people, Ole Nielsen, Marcin Dułak and Jens Jørgen Mortensen. Research in CAMd would have been impossible without the technical skills of these excellent scientists. I am also thankful to Marianne Ærsøe, Stavroula Nielsen and Helle Wellejus (now at Stanford), who have always done their best to keep the paperwork I had to do to the minimum. I much appreciate it.

I am indebted to all the scientists who commented on this thesis, M. Vanin, V. Tripković, D. Landis, P. Zawadzki, M. Dułak, J. Yan, J. Howalt, A. H. Larsen, T. Jiang, M. Björketun and L. Grabow. Each one has provided me with invaluable feedback on my research. A big thanks also goes to Isabella for her sympathy (and chocolate) during the writing period of the thesis.

Mother, father, thank you.

Finally, I would like to thank my friends in Greece, who have always been next to me. I can only believe I am privileged when in the company of such beautiful people.

Thank you all, for you have profoundly shaped my research and life.

Overview

The production of hydrogen-based fuels from sustainable energy sources and their use in fuel cells (FCs) offer a possible route towards carbon-neutral power. Efficient catalysis is vital for the success of hydrogen technology. Low-temperature FCs are considered among the most suitable solutions for mobile applications and for replacing combustion engines in vehicles. Improvement of the catalytic performance of low-temperature FC electrodes has proved a major materials science challenge. Both fundamental and development-oriented research is essential for the identification of novel and efficient electro-catalysts.

In this thesis, *catalytic performance* is evaluated with respect to three catalyst properties: activity, selectivity and stability. Low-cost, highly active and selective, durable electrodes are needed for the large-scale application of FCs.

In principle, the properties of a material derive from its electronic structure. By controlling the composition and morphology of a surface, its catalytic functionality can be tuned. Recent progress in the development of techniques for the controlled synthesis of materials at the nanoscale has opened new opportunities for tailoring catalysts atom-by-atom. The challenge lies in how the engineering of the structure of a surface should be directed towards desired catalytic functionality.

The problem of identifying and designing FC catalysts of enhanced performance is formulated below as a set of two questions:

1. What are the electro-catalytic properties of a material of specified composition and physical structure?
2. What is the composition and physical structure of an electro-catalyst exhibiting a set of desired (or optimal) properties?

Evaluation of the catalytic performance of a given structure can be computationally demanding but it is a tractable problem. The challenge lies in the inverse problem described by the second question. The configuration space can be enormous. Evaluating every candidate catalyst is impractical unless constraints exist that narrow down the number of candidates significantly. Physical insight deriving from identified trends in catalysis guides the search. An intermediate layer of descriptors may be introduced between surface structure and catalytic functionality. This way, the evaluation of catalytic performance is accelerated allowing for the study of more extended sets of candidate catalysts.

List of publications

Included publications

Paper I **Tuning the electro-catalytic performance of transition metal surfaces by alloying with chalcogen atoms**

Tritsaris G. A., Nørskov J. K., Rossmeisl J. In preparation.

Abstract

It is shown how the inclusion of chalcogen atoms in a transition metal surface can be used as a means to tune electro-catalytic performance. We use density functional theory calculations to evaluate the performance of model transition metal surfaces, both elemental and modified with selenium or sulfur, as cathode catalysts for low-temperature fuel cells. With ruthenium selenium as starting point, we study the effect of the chalcogen on the stability of the modified surfaces. An upper bound for their oxygen reduction reaction activity is established. We investigate their tolerance to methanol oxidation by simple thermodynamic considerations. The strength of the effect of the chalcogen is reflected on the strength of OH binding which assumes the role of a descriptor for the surface reactivity.

Contribution

I had the responsibility in planning the project and performing the calculations. My supervisors provided my with a constant flow of ideas and suggestions for the data analysis. I had the main responsibility in writing the paper with contributions from the co-authors.

II **Methanol electro-oxidation catalysis on elemental and bimetallic transition metals surfaces**

Tritsaris G. A., Rossmeisl J. In preparation.

Abstract

We develop a framework for the study of the methanol electro-oxidation reaction (MOR) for direct methanol fuel cells using density functional calculations and theoretical materials modeling. Under a unified methodology, we discuss trends in reactivity of a set of monometallic and bimetallic transition metal model surfaces, flat and stepped, including non-precious

alloys, overlayer structures and modified edges. All are found susceptible to the same upper limit of activity. A bi-functionality model is employed to screen for novel alloys of enhanced activity and we investigate a family of PtCu surfaces identified as promising catalysts by evaluating their reactivity and stability. In the same time, we try to expand the current molecular-level understanding of size effects in MOR catalysis by demonstrating the importance of modeling low-coordinated active sites such as steps in bridging the structure gap between studies of single crystal surfaces and realistic nanoparticles.

Contribution

The initial idea came from my supervisor for the study of methanol electro-oxidation on stepped platinum surfaces. I had the responsibility in planning the project, performing the calculations and analyzing the data. Insightful comments from my supervisor and valuable feedback from the people of the SUNCAT group during my visit to Stanford kept the project going. I had the main responsibility in writing the paper with contributions from my supervisor.

III **Atomic-scale modeling of particle size effects for oxygen reduction reaction on Pt**

Tritsaris G. A., Greeley J., Rossmeisl J., Nørskov J. K. Submitted.

Abstract

We estimate the activity of the oxygen reduction reaction on Pt nanoparticles of sizes of practical importance while explicitly accounting for the presence of surface irregularities and their effect on the activity of neighboring active sites. The proposed model effectively reproduces the experimentally observed trends in both the specific and mass activities for particles in the range between 2-30 nm. The latter is shown to maximize for particles of a diameter in the range of ca. 2-4nm. Our study demonstrates how an atomic-scale description of the surface microstructure is a key component in understanding particle size effects on the activity of catalytic nanoparticles.

Contribution

The initial idea came after discussion with my supervisors. I had the responsibility in planning the project and in performing the calculations. I had the main responsibility in analyzing the data and writing the paper with contributions from all the co-authors.

Other publications

Paper IV

Bifunctional Anode Catalysts for Direct Methanol Fuel Cells
Rossmeisl J., Ferrin P., Tritsaris G. A., Nilekar A. U., Koh S., Bae S. E., Brankovic S., Strasser P., Mavrikakis M. In preparation.

Contribution

I contributed in the data analysis and the writing of the theoretical part of the paper. No calculations were performed by me.

V

Electronic structure calculations with GPAW: A real-space implementation of the projector augmented-wave method
Enkovaara J. et al. (Tritsaris G. A.) *Journal of Physics Condensed Matter* 2010, **22** (25), art. no. 253202.

Contribution

I was involved in extending the functionality of the GPAW software working mainly on the symmetries detection and finite-difference approximations part of the code. My contribution to the paper concerns part of the discussion on real-space grids and the implementation of finite-difference operators.

Contents

1. Introduction

Hydrogen energy

Fossil fuels are the dominant energy source used today [1]. A growing global concern for the shrinking availability of fossil fuels and the environmental degradation associated with their use has motivated the search for alternative energy sources. Renewable energy sources offer the possibility of solving or at least mitigating the problems. Quoting Lewis and Nocera: "The supply of secure, clean, sustainable energy is arguably the most important scientific and technical challenge facing humanity in the 21st century" [1].

Although abundant on earth, hydrogen is not readily usable as a fuel. It is produced by the chemical transformation of compounds such as water and hydrocarbons. Today, hydrogen production is mostly based on steam reforming of natural gas [2]. Hydrogen can serve as a clean energy carrier but only when produced with the use of renewable energy sources [2,3]. Hydrogen production is only one component of the so-called *hydrogen economy* [4]. It is an umbrella term for all the elements of the hydrogen fuel chain, i.e. the production of hydrogen, its storage, delivery and end use. Significant challenges are associated with each of them [5].

Low-temperature fuel cells

FCs are a key technology for hydrogen-based power and heat delivery [6,7]. Although hydrogen can also release its energy by combustion [8], FCs offer an opportunity for efficient energy conversion. They are electrochemical cells that directly convert the free energy of a chemical reaction into electrical energy (galvanic cells). W. Grove first demonstrated their use as power generators [9]. Although access to cheap fossil fuels hindered FC development, the increase in energy demands has renewed interest in FC technology. The associated cost and durability issues remain the main hurdle on the road for the effective commercialization of FCs [10-14].

There are a few ways of categorizing FCs:

1. by the type of electrolyte employed
2. by the fuel feed
3. by the operating temperature

The *polymer exchange (electrolyte) membrane fuel cell* (PEMFC) takes its name from the proton conducting membrane it uses. The *direct methanol fuel cell* (DMFC) [15,16] is named after the fuel fed into the cell, liquid methanol. The conductive medium of DMFCs is the same as in the PEMFCs. Alternatively, by considering the temperature of operation, a FC is categorized as low-temperature

or high-temperature. The PEMFC and DMFC are both low-temperature FCs (operating temperature of ca. 100°C). The upper limit of the temperature of operation for the PEMFC is dictated by the membrane. For the membrane to be conducting it has to be sufficiently humidified [17]. High-temperature FCs operate at much higher temperatures, in the range of 600-1000°C. The molten carbonate fuel cell (MCFC) and the solid oxide fuel cell (SOFC) belong to this class.

This thesis focuses on the low-temperature FCs. They are most suitable for mobile applications, such as powering vehicles, providing power where no electric grid is available and power consumer electronics [18]. At the most basic level of description, a low-temperature FC cell comprises two electrodes, separated by a proton exchange membrane (Fig. 1.1). The electrodes are connected to an external circuit. Each of the electrodes assumes the combined role of supplying the gas reactants to the catalyst and catalyzing the half-cell reaction. The electro-catalysis takes place on supported nanoparticles, dispersed on the electrode surface. The support acts as an electronic conductor. The catalytic nanoparticles are also in contact with the ionic membrane. The membrane, the catalyst layers and the gas diffusion layers make up together the *membrane electrode assembly* (MEA).

The overall reaction of an electrochemical cell is generally described as

$$a\,ox_1 + b\,red_1 \rightarrow c\,ox_2 + d\,red_2 \tag{1.1}$$

where *ox* and *red* are the oxidizing and reducing species. The cell voltage ΔU is determined from the following expression [19]

$$\Delta U = \Delta U^{o} - \frac{RT}{nF}\ln\frac{\left[ox_2\right]^{c}\left[red_2\right]^{d}}{\left[ox_1\right]^{a}\left[red_1\right]^{b}} \tag{1.2}$$

where n is the number of electrons transferred during the reaction, F the Faraday constant, R the Boltzmann constant and T the temperature. The brackets denote the activity of the species in solution. The standard potential is denoted by ΔU^{o}. At equilibrium, ΔU^{o} is related to the standard Gibbs free energy change ΔG^{o} via [19]

$$\Delta G^{o} = -nF\Delta U^{o} \tag{1.3}$$

On the anode hydrogen, methanol or any hydrogen-containing fuel is deprotonated. The anode half-reaction for a PEMFC is

$$H_2 \rightarrow 2H^{+} + 2e^{-} \tag{1.4}$$

The protons are transported to the cathode through the membrane. The electrons are channeled via the external circuit to the anode. On the cathode, the protons and electrons combine with oxygen-rich fuel (e.g. air)

$$½O_2 + 2(H^{+} + e^{-}) \rightarrow H_2O \tag{1.5}$$

The overall PEMFC reaction is

$$H_2 + ½O_2 \rightarrow H_2O \tag{1.6}$$

with ΔG^{o} = -237kJ/mol. The equilibrium potential for an ideal PEMFC is then calculated from Eqn. 1.3 as ΔU^{o} = 1.23V. Multiple cells are assembled together into FC stacks for multiplying the power generated [6,7].

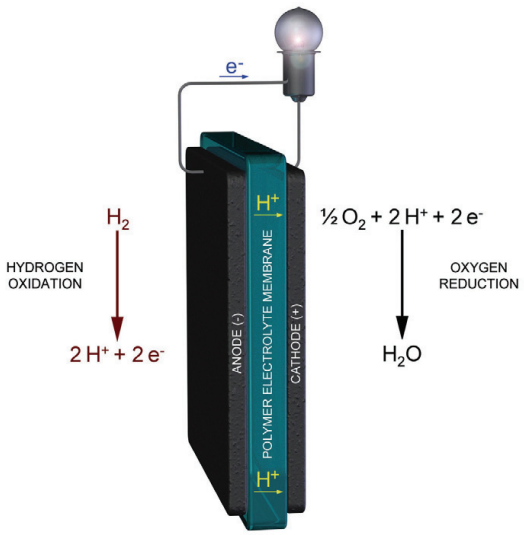

Fig. 1.1 Schematic of a polymer electrolyte hydrogen-oxygen fuel cell [20].

Key electrochemical reactions

Two chemical reactions are studied in this thesis:

- the electrochemical oxygen reduction reaction
- the electrochemical methanol oxidation reaction

Both the reactions are studied assuming acidic environment.

Oxygen reduction reaction

For the study of the electrochemical oxygen reduction reaction (ORR) [21,22], a direct 4-electron pathway is assumed

$$O_2 + 4(H^+ + e^-) \rightarrow 2H_2O \tag{1.7}$$

It comprises the following elementary steps:

$$\begin{aligned} &1.\quad O_2 + H^+ + e^- + * \rightarrow HOO* \\ &2.\quad HOO* + H^+ + e^- \rightarrow H_2O + O* \\ &3.\quad O* + H^+ + e^- \rightarrow OH* \\ &4.\quad OH* + H^+ + e^- \rightarrow H_2O + * \end{aligned} \tag{1.8}$$

A surface site is denoted by *. A different pathway for the ORR is through the formation of peroxide species (H_2O_2). First, oxygen is reduced to peroxide

$$O_2 + 2(H^+ + e^-) \rightarrow H_2O_2 \tag{1.9}$$

Peroxide is then either reduced to water

$$H_2O_2 + 2(H^+ + e^-) \rightarrow 2H_2O \tag{1.10}$$

or decomposed on the surface

$$H_2O_2 \rightarrow 2H_2O + O_2 \tag{1.11}$$

The direct 4-electron pathway is chosen to describe the FC cathode reaction since at ORR relevant potentials, peroxide formation is only small on platinum [23,24] and ruthenium selenium surfaces [25].

Methanol oxidation reaction

The theoretical half-cell voltage of an FC anode, which splits hydrogen molecules into protons and electrons, is zero. On Pt-based electro-catalysts, the hydrogen oxidation reaction (HOR) occurs readily but only when pure hydrogen is fed into the FC [26]. An alternative to the expensive pure hydrogen is the use of liquid methanol. The electrochemical methanol oxidation (MOR) is described by a 6-electron process [16,27]

$$CH_3OH + H_2O \rightarrow CO_2 + 6(H^+ + e^-) \qquad (1.12)$$

with $\Delta U^0 = 0.046V$.

The MOR proceeds through a complex reaction mechanism. A *dual-path* mechanism is generally recognized for the electrochemical oxidation of methanol, which comprises two different parallel paths [27-29]:

- The *direct* or *active intermediate* path where methanol oxidizes directly to CO_2 without passing through a poisoning intermediate such as CO (Fig. 1.2a).
- The *indirect* or *poisoning intermediate* path where the oxidation proceeds via the formation of poisoning species (Fig. 1.2b).

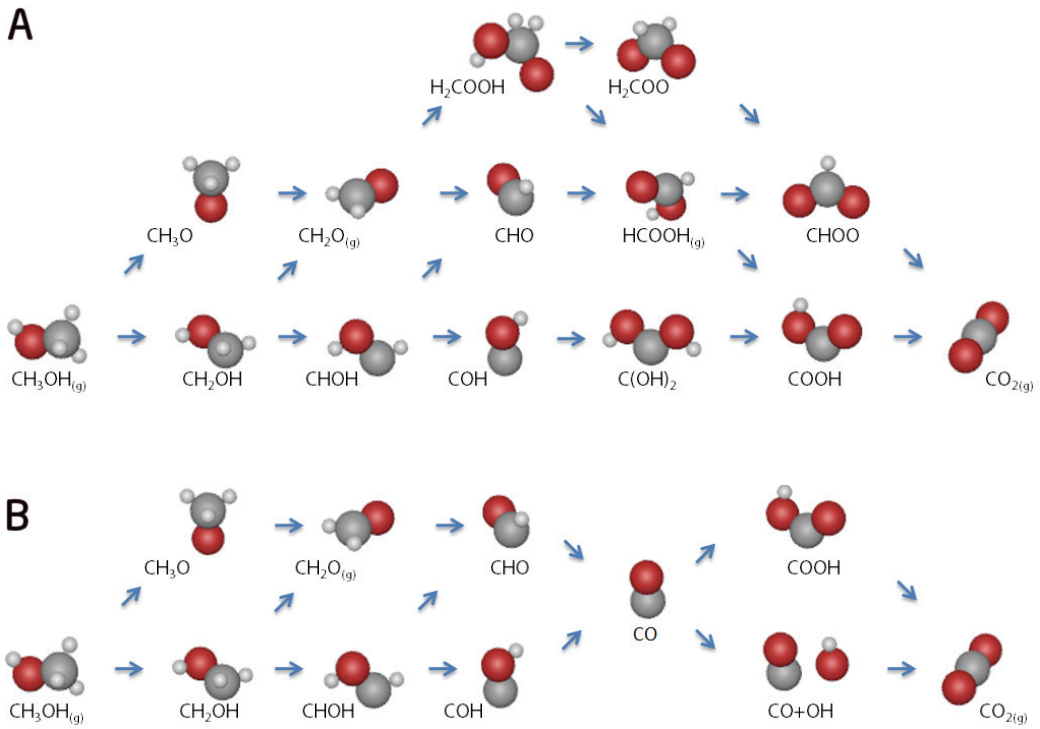

Fig. 1.2 The a) direct and b) indirect paths for the methanol electro-oxidation reaction mechanism.

The need for efficient catalysts

In reality, there is a great deviation between the ideal equilibrium potential and the measured *open circuit voltage* (OCV) [11]. The term *overpotential* is used to describe voltage losses that result from the combined effect of many parasitic processes [30,31]:

Activation losses A significant part of the cell voltage is consumed just for driving the reaction. The voltage drop in this case is non-linear. Increasing the roughness of electrodes, the reactant concentration, pressure and

	temperature, as well as using catalysts that are more efficient can reduce such losses.
Fuel cross-over	Voltage losses rise from the diffusion of fuel through the membrane. In the case of DMFCs, electro-osmotic drag of methanol can take place. The mixed potential caused by methanol reaching the cathode and its subsequent oxidation can be substantial. The methanol cross-over effect depends on factors such as the membrane permeability and thickness, concentration of methanol, FC operating temperature and the selectivity (tolerance to methanol oxidation) of the cathode catalyst.
Ohmic losses	Losses occur as electron transport through the electrodes and ionic transport through the electrolyte is met with resistance. The voltage losses are essentially linear. Using electrodes with high conductivity, cell interconnects of good design and making the electrolyte layer as thin as possible are ways to reduce the internal resistance of the cell.
Mass transport	Losses occur from the depletion of reactants at the electrode surface during the reaction. For example, this situation may arise from the mismatch in fuel supply and consumption when a reformer is used.

On the basis of the above analysis, the voltage ΔU of a PEMFC is written as [32]

$$\Delta U = \Delta U^{o} - \Delta U_{ohmic} - \eta_{ORR} - \eta_{tx} \qquad (1.13)$$

The terms ΔU_{ohmic}, η_{ORR} and η_{tx} describe the ohmic, ORR overpotential and mass transport losses, respectively. The performance of a state-of-the-art Pt-based MEA is shown in Fig. 1.3. The dashed line marks ΔU^{o}. Comparison between the lines marked by the circular and diamond symbols shows the increase in current density that can be achieved by reducing mass transport losses by 50%. Still, Fig. 1.3 shows that the ORR overpotential accounts for the largest part of the total voltage losses, measured ca. 400mV at 1.5A/cm^2.

DMFCs are characterized by even greater losses compared to PEMFCs. The theoretical standard Gibbs free energy change for both the MOR and HOR is close to zero. In real systems, significant potential losses are introduced by the complexity of the MOR mechanism, which involves many intermediate reaction steps (Fig 1.2). Moreover, even the current state-of-the-art MOR catalysts, exclusively Pt-based [33], are susceptible to surface poisoning by CO, a strongly binding reaction intermediate [34]. In that respect, catalysts with increased CO tolerance are desirable. Highly selective ORR catalysts are also desirable for the DMFC to prevent the combustion of methanol, should methanol reach the cathode electrode.

Another hindrance closely related to the commercialization of FC technology is the cost of the catalyst [32,33]. Pt is a rare and thus expensive metal. The MAE loading has been reduced to the point where an amount of 72-94gr of Pt is used for powering a 75kW automotive FC system [11]. Still, the associated cost and limited Pt supply render large-scale commercialization prohibitive [11]. A reduction in the precious metal loading is desired or, equivalently, catalysts of increased mass activity (activity per mass) are needed.

Several strategies have been identified for overcoming the aforementioned obstacles [35], including more efficient utilization of the precious metal by alloying [36-40] and the exploration of new non-precious metal catalysts [32,33,41,42]. For DMFCs, efforts in tailoring the morphology of the anode catalyst towards increased CO tolerance and enhanced activity have been

made [43-45]. Prominent examples of efficient DMFC anode catalysts are platinum ruthenium alloys [16,27,36,46], the most commercially successful DMFC anode catalyst, and platinum tin [16,47].

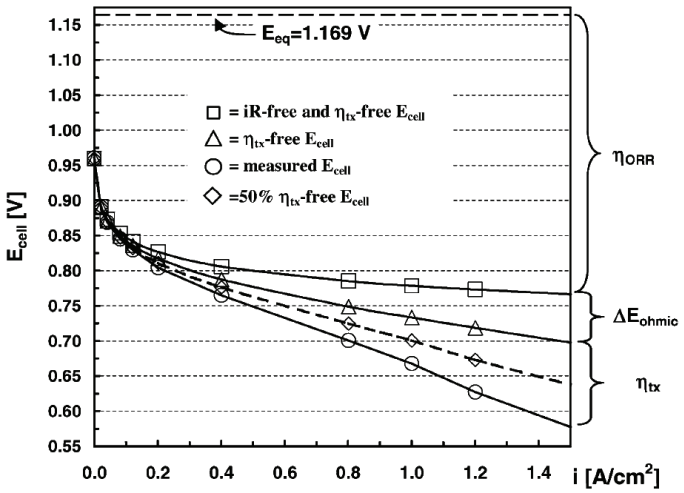

Fig. 1.3 The MEA performance in a 50cm^2 single cell using state-of-the-art components [32]. The oxygen reduction overpotential accounts for the largest part of the total voltage losses.

The computational catalysis approach

Computational materials science (CMS) links theory and experiment through the performance of computer simulations. Computer experiments offer insights into the underlying processes governing the properties of existing materials and assist in the design of novel structures [48-50]. The recent progress in the CMS field is inseparable from the ever-increasing availability of computational resources. Many computational method families have been developed for the study of a diverse range of systems over orders of magnitude in time and length scales [51-53].

Transferring a scientific or technological problem into the computer requires some intermediate steps [51]. A model is developed which describes the phenomenon under study in a simplified way, yet capturing all the necessary science. On the basis of this model, an approximate theory or a mathematical model is constructed. The latter is then translated into a numerical problem. Approximations are introduced. Computer simulation undertakes the final task of solving the approximate numerical problem in an efficient and accurate way.

Real systems spend most of their time in a state that is of no interest for the issue under investigation. For example, under the framework of collision theory a catalytic reaction is a rare event. Only a small fraction of all collisions between the catalyst surface and the reactants leads to product formation [19]. The strength of computer simulation lies in hiding such "idle" behavior in the carefully chosen assumptions and approximations of the models employed. Equivalently, even if the computational power available is enough to describe and study a real catalytic system in minute detail, the same resources may be allocated for the study of a more complex system based on simplified models. Alternatively, a set of less complex systems may be studied in search for general laws (trends) governing their behavior.

Surface science and catalysis experiments often raise questions that cannot be answered by experimental means alone. On the other hand, simulation of catalytic systems will give an answer for a set of input parameters, even for an unrealistic one. Moreover, the construction of an approximate theory requires a basic understanding of the catalytic process under study. By comparing results from accurate simulations with experimental observations, models are evaluated. By comparing between simulations and approximate theories, the validity of the latter is tested. Theoretical modeling complements experiments by providing tools for their qualitative interpretation. This synergy among theory, experiment and simulation allowed recent progress to be made in each of these areas of the catalysis field (Fig. 1.4).

Catalysis is inherently an atomistic phenomenon. During catalytic reactions, bonds are broken and formed between the catalyst atoms and the reaction atomic and molecular species. The importance of transition metals (TMs) in catalysis was early realized [54]. Electronic structure calculations have proved invaluable in bringing insight into the surface processes governing catalytic behavior [50]. In this thesis, density functional theory (DFT) is used to investigate the connection between structure of TM-based surfaces and their electro-catalytic functionality. Bridging directly the world of atoms and molecules with macroscopically observed behavior only by DFT modeling is impractical. The gap is closed by partitioning the time and length scale continuum into separate regions each one treated with the use of appropriate methods in a hierarchical fashion. DFT simulation coupled to techniques from statistical mechanics and thermodynamics essentially provides a multi-scale modeling approach to theoretical and computational catalysis. Ultimately, computational studies of atomistic model systems provide feedback to laboratory-scale studies and receive feedback from them [55].

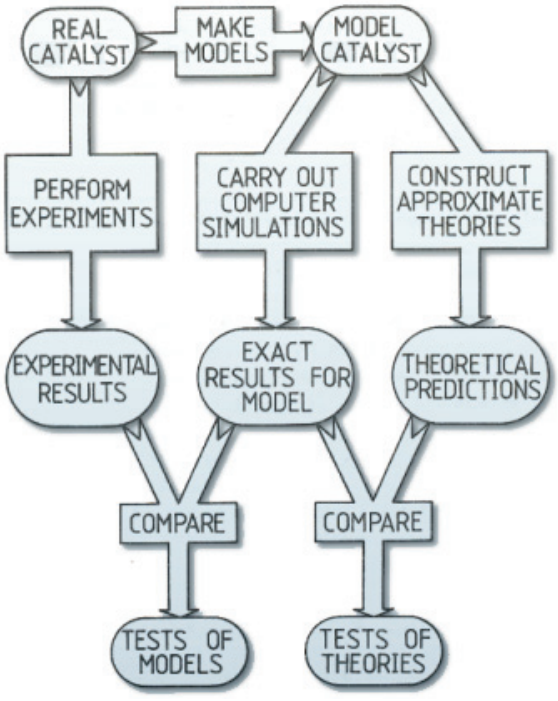

Fig. 1.4 Synergy among experiment, theory and computer simulation (adapted from Allen and Tildesley [56]).

Thesis outline

The outline of the thesis is the following:

Chapter 2 Electronic structure methods and adsorption models for the theoretical study of catalysis are introduced.

3 A methodology for the evaluation of electro-catalytic performance from electronic structure calculations is presented.

4 Methods and tools for managing scientific data sets.

5 The search for efficient, transition metal-based, oxygen reduction and methanol oxidation electro-catalysts. This chapter offers a look at the findings of the included Papers from multiple perspectives.

6 Summary and outlook.

2. Theory

The thesis studies chemical reactions catalyzed on the surface of FC electrodes. The main components of any of the catalytic systems studied are the electrode catalyst and the reaction intermediates. Computational treatment of such systems involves models for the catalyst surface, the atomic and molecular reaction species, as well as the interactions between them. An atomic-level approach. The catalyst is modeled, for example, as a slab of atomic layers. The interaction between the catalyst and any atomic or molecular species is described quantum mechanically. The electrode environment may be modeled as part of the catalytic system. Alternatively, its effect is included in the model as corrections on the properties of the surface and the species. For example, the fuel cell potential is included as a shift in the energy of the electrode electrons. The electrolyte is either explicitly modeled, for example as a bilayer of water molecules on the catalyst surface, or as a correction to the calculated adsorption energies that describe the stability of reaction intermediates on the surface.

This chapter introduces fundamental theory and models for a basic understanding of the catalytic systems studied in the thesis.

Density functional theory

DFT is a popular quantum-mechanical method used for computational studies [52,53]. The Schrödinger equation for electrons in the field of atom cores is treated by an approximate Hamiltonian. Quantum Monte Carlo (QMC) methods work directly with the correlated many-electron wavefunction (WF) and they are highly accurate (achieving total energy accuracies of the order of 10^{-4}eV). Because of significant computational burden their use is limited to calculations of small systems. Tight-binding (TB) methods on the other hand are among the fastest. They are suitable for structures of many thousands of atoms. Since they rely on the approximation of many terms of the Hamiltonian their accuracy is limited. In between, lies applied DFT that can handle, in reasonable time, systems with up to 10^2-10^3 atoms [57].

Methods based on DFT have been extensively used for the study of FC catalysis. Compiling a comprehensive list of successful study cases is an arduous task. Chemical reactions that have been studied include the ORR [24,58-61] and the MOR [62-65].

DFT is much more than an efficient method for electronic structure calculations. It provides an intuitive framework for treating the many-electron problem. Numerous resources exist on the subject [52,53,66]. In the following, only a sketch of the basic principles of DFT is attempted.

The Thomas-Fermi model

Under the *Born-Oppenheimer* or *adiabatic approximation*, the movement of nuclei is assumed not to induce excitations in the electronic system [67]. The nuclei are treated as fixed points in space. The (electronic) Schrödinger equation for an *N*-electron system in the field of heavy nuclei is described by an interacting Hamiltonian (in atomic units)

$$H = \sum_{i=1}^{N}\left(-\frac{\nabla_i^2}{2}\right) + \sum_{i=1}^{N} V_{\text{ext}}(r_i) + \sum_{i<j}^{N}\frac{1}{|r_i - r_j|} \tag{2.1}$$

where

$$V_{\text{ext}}(r_i) = -\sum_{a}\frac{Z_a}{|r_i - r_a|} \tag{2.2}$$

is the *external potential* acting on electron i at point r_i caused by the nuclei, each of charge Z_a positioned at point r_a. In the work of L. H. Thomas [68] and E. Fermi [69], the most rudimentary form of DFT was illustrated. The kinetic energy T_{TF} is approximated as an explicit functional of the electron density n(r)

$$T_{TF} = C_1 \int n(r)^{\frac{5}{3}}\, dr \tag{2.3}$$

with C_1 a constant. Because exchange and correlation (xc) effects among electrons are neglected, the accuracy of Thomas-Fermi theory implementations is limited.

The Hohenberg-Kohn framework

It was P. Hohenberg and W. Kohn, in their seminal work, who first showed that the ground state properties of a many-electron system can be uniquely determined by its density [70]. The Hohenberg-Kohn DFT is an exact theory for many-electron systems. Its comprises two theorems [53]:

Theorem I The external potential $V_{ext}(r)$ is determined, within a trivial additive constant, by the ground state electron density $n_0(r)$.
Since the Hamiltonian is fully determined, except for a shift in the energy, it follows that the many-electron WF for all states (ground and excited) are determined. Therefore all properties (every physical observable) of the system can be calculated, in principle exactly, from the ground state density $n_0(r)$.

II An energy functional can be defined for any external potential $V_{ext}(r)$. For any particular external potential $V_{ext}(r)$, the electron density $n(r)$ that minimizes the energy functional corresponds to the exact ground state density $n_0(r)$.
The minimization of the energy functional suffices to determine the exact ground state properties. Excited states are determined otherwise.

The Kohn-Sham auxiliary system

W. Kohn and L. J. Sham proposed an ansatz which translates the interacting many-electron problem into an auxiliary, non-interacting one [71]. The ansatz rests upon the assumption that the exact ground state density of an interacting many-electron system can be described by the ground state density of an auxiliary system of non-interacting electrons. The Hamiltonian of the auxiliary

system is chosen to have the usual kinetic operator and an effective potential $V_{eff}(r)$ acting on an electron.

For a system of N-independent electrons the density is given by

$$n(r) = \sum_{i=1}^{N} |\psi_i(r)|^2 \tag{2.4}$$

The expression for the energy functional E_{KS} assumes the following form

$$E_{KS} = T_S[n] + \int dr V_{ext}(r) n(r) + E_{Hartree}[n] + E_{xc}[n] \tag{2.5}$$

where T_s is the independent-particle kinetic energy an implicit functional of the electron density given in terms of the N single electron orbitals ψ_i

$$T_S = -\frac{1}{2}\sum_{i=1}^{N} \langle \psi_i | \nabla^2 | \psi_i \rangle = -\frac{1}{2}\sum_{i=1}^{N} \int dr^3 \psi_i^*(r) \nabla^2 \psi_i(r) \tag{2.6}$$

$E_{Hartree}$ is the classical Coulomb interaction energy given by

$$E_{Hartree} = \frac{1}{2}\int dr^3 dr'^3 \frac{n(r)n(r')}{|r - r'|} \tag{2.7}$$

Finally, the xc energy E_{xc} describes the many-electron effects of the interacting system. The above analysis can be generalized to introduce spin [53]. The Kohn-Sham approach opens the path to practical total energy calculations. The Kohn-Sham system is solved for the ground state iteratively. For a given $V_{ext}(r)$ an initial guess for the density n(r) is made. Then

1. the effective potential $V_{eff}(r)$ is constructed

   $$V_{eff} = V_{ext} + V_{Hartree} + V_{xc} \tag{2.8}$$

   For $V_{Hartree}$ and V_{xc}, $V = \delta E / \delta n$.
2. the N single electron equations are solved for the ψ_i orbitals
3. the electron density is calculated on the basis of the new ψ_i
4. the above procedure is repeated until the difference between the input and new electron density meets a given convergence criterion(typically of the order of 1meV)

Exchange and correlation functionals

Exchange is a manifestation of the Pauli exclusion principle. Correlation describes the remaining many-electron effects of the interacting system. The exact form of the xc functional E_{xc} is unknown. If such a functional was known, all properties of a system could be calculated precisely. In the same time, the complexity of the initial many-electron problem would be entirely restored, together with computational burden associated with its numerical solution [72].

The strength of the DFT for practical calculations lies in the approximate character of the xc functionals. Different functionals allow for different balance between speed and accuracy. There are two main approaches to the development of functionals:

1. Climbing the so-called "Jacob's ladder" of DFT functionals, advanced by J. P. Perdew [73,74] The philosophy behind the approach is to increase accuracy by systematically improving less accurate functionals.
2. Designing empirical functionals. Empirical functionals rely on fitted parameters, sacrificing physical insight for accuracy [75]. They are widely used by the chemical community.

In the first approach, the bottom rung of the DFT ladder is the local density approximation (LDA) [71]. It treats the interaction among electrons at the limit of the homogeneous electron gas. Under this assumption, E_{xc} is written as

$$\begin{aligned} E_{xc}^{LDA}[n] &= \int dr^3 n(r)\,\varepsilon_{xc}^{hom}(n(r)) \\ &= \int dr^3 n(r)\left[\varepsilon_x^{hom}(n(r)) + \varepsilon_c^{hom}(n(r))\right] \end{aligned} \tag{2.9}$$

The exchange part is given by

$$\varepsilon_x^{hom} = \frac{3}{4}\left(\frac{3}{\pi} n(r)\right)^{1/3} \tag{2.10}$$

Accurate values for ε_c^{hom} are available from QMC calculations [76]. LDA favors densities that are more homogeneous than the exact ones. Binding energies and cohesive energies are usually overestimated.

The next rung holds generalized-gradient approximations (GGAs) [77] where the gradient of the density $|\nabla n(r)|$ is also taken into consideration, rendering the functional semi-local

$$E_{xc}^{GGA} = \int dr^3 n(r)\,\varepsilon_{xc}^{GGA}\left(n(r), |\nabla n(r)|\right) \tag{2.11}$$

Such functionals provide accuracy of the order of 0.1eV. GGAs significantly improve total energies of atoms and binding energies compared to LDA. For TMs, they give better estimation of lattice constants and cohesive energies.

Even higher accuracy is achieved by meta-GGAs which depend on the kinetic energy (third rug) [78], non-local functionals which include the exact exchange (fourth rug) [79], and so on.

For all the calculations in the thesis, the RPBE [80] flavor of GGA was chosen. RPBE was developed as revision of the Perdew-Burke-Ernzerhof (PBE) functional [81]. RPBE was used for it is commonly considered to improve the calculation accuracy of chemisorption energies.

Limitations

Despite the widespread acceptance of the Kohn-Sham DFT for electronic structure calculations, none of its implementations are without limitations. Failures in calculated properties are not an intrinsic flaw of the DFT. They rather emerge from the shortcomings of the approximate nature of the xc functionals employed and their violation of the requirements of the exact functional [82-84].

An illustrative example is this of H_2^+. As the protons are stretched, crossing the dissociation limit will result in an unrealistically low energy structure comprising two distinct hydrogen atoms with half an electron each. A consequence relevant to computational catalysis is the underestimation of reaction barriers. The extended form of transition states resembles the stretched H_2^+ with electrons delocalized over more than one center. No transition states are modeled in this thesis.

The stretching of closed-shell H_2 exemplifies an error of different nature. The covalent bond in H_2 is well described. However, close to dissociation each hydrogen atom will have half a spin-up and half a spin-down electron. Generally, the problem characterizes situations with degeneracy or near-degeneracy as in strongly correlated systems.

Implementation

Modern DFT-based methods provide different levels of compromise between speed of calculation and accuracy of results.

All total energy calculations in this thesis were performed with the GPAW electronic structure code, a DFT implementation based on the projector-augmented wave (all-electron, frozen core approximation) method [85], using real-space uniform grids and multigrid methods [86,87]. GPAW also supports calculations based on the linear combination of atomic orbitals (LCAO) method, which uses a basis set of atomic orbital-like functions instead of grid-based WFs [88]. In the following, various implementation aspects of DFT relevant to GPAW are presented.

The PAW formalism and the frozen core approximation

The *projector augmented wave* (PAW) formalism developed by Blöchl is an extension of augmented wave methods and the pseudopotential approach [85]. Within the system, different levels of accuracy are required to describe the atomic valence and core regions. The requirement of orthogonality introduces rapid oscillations in the WFs of the core electrons. On the other hand, the WFs of valence electrons are smoother.

In the pseudopotential approach the rapid oscillations in the core region are eliminated by introducing an effective, smooth potential to describe the core electrons [89,90]. When constructing such pseudopotentials, attention is paid so the effect of the core on the valence electrons is reproduced [91]. One disadvantage of this approach is that all the fine features of the all-electron wavefunction (AEWF) close to the nucleus are lost.

On the other hand, the PAW method treats core and valence electrons independently. Formally, the full information about the AEWF is retained. PAW is based on a linear transformation T between smooth valence (pseudo) WFs $\tilde{\psi}_n$ and the AEWFs ψ_n

$$\left|\Psi_n\right\rangle = T\left|\tilde{\Psi}_n\right\rangle \tag{2.12}$$

with n denoting the state index. The transformation operator T is expressed as

$$T = 1 + \sum_a \sum_i \left(\left|\varphi_i^a\right\rangle - \left|\tilde{\varphi}_i^a\right\rangle\right)\left\langle \tilde{p}_i^a\right| \tag{2.13}$$

where a is the atomic index and i is an index for the combination of the principal, angular momentum, and magnetic quantum numbers. The set of φ_i^a, $\tilde{\varphi}_i^a$ and $\tilde{p}_i^a$ functions are the basic ingredients of the PAW formalism (Fig. 2.1):

- The AEWF ψ_n is expanded inside an atom-centered augmentation sphere which is defined by a radius r_c^a. No two spheres overlap. The basis is the atom-centered AE partial waves φ_i^a. The partial waves are constructed as solutions to the AE (scalar-relativistic) calculation of the isolated, spherically symmetric atom.
- The corresponding smooth partial waves $\tilde{\varphi}_i^a$ coincide with the AE partial waves φ_i^a outside the augmentation region

  $$\varphi_i^a(r) = \tilde{\varphi}_i^a(r) \text{ for } \left|r - R^a\right| > r_c^a \tag{2.14}$$

  Inside the augmentation sphere, they are smooth functions. They serve as a basic set for $\tilde{\psi}_n$.

- The projector functions $\tilde{p}_i^a$, dual to the partial waves, are localized inside the augmentation sphere. They are orthogonal to the smooth partial waves

$$\left\langle \tilde{p}_{i_1}^a \middle| \tilde{\varphi}_{i_2}^a \right\rangle = \delta_{i_1 i_2} \tag{2.15}$$

The core electrons are localized inside the augmentation. In the *frozen core approximation* the Kohn-Sham core states are described by the core states corresponding to atoms in isolation [92]. Under this assumption, there is no need to treat the WFs that correspond to core electrons during the self-consistent solution of the Kohn-Sham system.

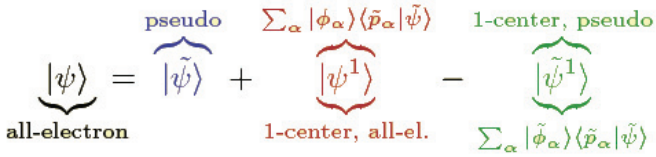

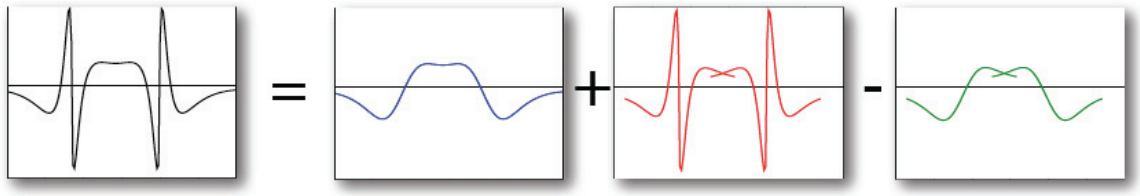

Fig. 2.1 Schematic of the projector augmented wave transformation (as presented by Blöchl).

Real-space grids and finite-difference approximations

In GPAW, WFs, potentials and densities are represented by values on discrete points of a 3-d real-space grid (mesh) [93]. When real-space grids are employed, energies and forces become dependent on the relative position of atoms with respect to the grid points, the so-called *egg-box effect* [94]. In this thesis, all the model structures were treated in an orthorhombic unit cell. Convergence of the values of properties of interest was tested against the spacing of the grid to ensure that egg-box effects are negligible.

Finite-difference (FD) methods are used for the calculation of derivatives [95]. The Laplacian is discretized as

$$\nabla^2 f(r) = \sum_{a=1}^{3} \sum_{n=-N}^{N} \frac{1}{h_i^2} c_n^N f(r + n h_i) + O\left(h_i^{2N}\right) \tag{2.16}$$

where h_i are vectors generating the grid. The coefficients c_n^N represent the N-th order FD coefficients for the second derivate expansion [96]. The accuracy of the discretization is determined by the grid spacing h_i and the order of approximation N.

For example, the expression for the kinetic part of the PAW pseudo energy is given as

$$\tilde{E}_{kin} = -\frac{1}{2} \sum_n f_n \int dr \tilde{\psi}_n^*(r) \nabla^2 \tilde{\psi}_n(r) \tag{2.17}$$

where f_n are the occupation numbers (between 0 and 2). The kinetic energy is discretized as

$$\tilde{E}_{kin} = -\frac{1}{2} \sum_n f_n \sum_g \tilde{\psi}_{ng} \sum_{g'} \tilde{L}_{g'} \tilde{\psi}_{ng'} \tag{2.18}$$

$L_{g'}$ represents the FD Laplacian operator centered on grid point g'.

All calculations were performed with a cross-shaped stencil comprising 19 points for the evaluation of the kinetic energy. The Poisson equation is solved in a similar manner with a multigrid method [97]. A compact Mehrstellen stencil was employed in that case [93].

Integration in k-space

For periodic structures, evaluation of quantities such as the total energy and density requires integration over the Brillouin zone (BZ). For practical implementations, integration is performed by sampling the BZ over only a finite set of points. The points are selected in such a way that the approximation is accurate. The method employed here was proposed by Monkhorst and Pack [98]. It uses a uniform mesh of points generated by vectors of the form

$$k_{n_1,n_2,n_3} \equiv \sum_{i}^{3} \frac{2n_i - N_i - 1}{2N_i} G_i \qquad (2.19)$$

where G_i are the primitive vectors of the reciprocal lattice.

The smallest fraction of the BZ that is sufficient for the estimation of the integral is the *irreducible Brillouin zone* (IBZ). All other k-points outside the IBZ are mapped onto at least one point in the IBZ through symmetry operations. Even in the case where the crystal structure has no symmetry, it is possible to work with an IBZ half the size of the BZ, on the grounds of the time-reversal symmetry that any system has in the absence of magnetic fields (invariance of the Hamiltonian under a $k \rightarrow -k$ transformation) [53].

Fermi surface smearing

For metallic structures, instability may rise during the self-consistent solution caused by fluctuations of the occupation numbers of the states around the Fermi level (charge sloshing). Introducing temperature benefits calculations by replacing the zero Kelvin Heaviside energy distribution with a softer Fermi-Dirac distribution, making convergence less sensitive to such effects. For calculations of TM-based surfaces, an electronic temperature in the range of 0.10-0.15eV was used for smearing the occupation numbers. All calculated total energies were then extrapolated to zero electronic temperature [99].

Eigensolvers

GPAW supports three different iterative eigensolvers, the *residual minimization method-direct inversion in iterative subspace* (RMM-DIIS) [100], the *conjugate gradient* (CG) method [101] and the *Davidson method* [102]. The RMM-DIIS was the eigensolver of choice for its efficiency. Since it minimizes the norm of a residual vector instead of the energy, it effectively converges to a state close to the input trial one. A good initial guess for the WFs is required. GPAW constructs the initial electron density of the Kohn-Sham self-consistent scheme using LCAO with the minimal "single-zeta" basis (one orbital per valence electron). Still, convergence problems may rise if the structure corresponds to an unphysical configuration. In this case, the CG eigensolver was employed. CG stands as a robust eigensolver although noticeably slower than the RMM-DIIS when large systems are calculated. It attempts a descent to the energy minimum building on all previous search directions. Finally, the Davidson eigensolver was the primary choice for all spin-polarized calculations.

Geometry optimization

The calculations in this thesis concern exclusively optimized structures. Geometry optimization was performed by the minimization of the inter-atomic forces. Forces were calculated on the basis of the Hellmann-Feynmann theorem [103,104] and fed into a Broyden-Fletcher-Goldfarb-Shanno (BFGS) optimizer [105]. The atom positions were relaxed to the upper limit of 0.045 eV/Å for the forces.

Adsorption models

As in heterogeneous catalysis, an electro-catalyst increases the rate of an electrochemical reaction without undergoing any chemical change itself [19]. Catalysis on surfaces involves a range of different phenomena such as adsorption of reactants on the catalyst surface, their dissociation and the formation of product species. All the aforementioned processes involve the formation and breakage of chemical bonds. Understanding chemical bonding is essential for an atomistic understanding of catalytic processes. In the following, a theoretical framework for modeling adsorption on metal surfaces is presented.

Tight-binding approximation

In the TB approximation, two atomic states $|a\rangle$ and $|b\rangle$ with energy levels ε_A and ε_B give upon interaction two new energy levels, one bonding and one antibonding. For an heteronuclear molecule ($\varepsilon_A \neq \varepsilon_B$) described by the Hamiltonian H, the bond energy is

$$\Delta E = -2S_{ab}V_{ab} - \sqrt{4V_{ab}^{\,2} + \left(\varepsilon_B - \varepsilon_A\right)^2} \qquad (2.20)$$

where $S_{ab} = \langle a|b\rangle$ and $V_{ab} = \langle a|H|b\rangle$ are the *overlap matrix element* and the *coupling matrix element* respectively (with $S_{ab}V_{ab} < 0$). The first term of Eqn. 2.20 describes repulsion caused by overlap of the states and the second attraction caused by hybridization.

Basic features of the electronic structure of solids are described by TB theory. The density of states (DOS) of a TM is shown in Fig. 2.2. The Fermi level crosses both the half-filled s-band and the d-band. The occupancy of the d-band varies among TMs. The coupling of the localized d-electrons is weak, described by a small matrix element V. The respective DOS is described by a narrow band. On the other hand, the delocalized nature of the s-p electrons is reflected on a larger matrix element V. A broader DOS distribution describes the respective bands.

The Newns-Anderson model

The Newns-Anderson model describes chemisorption on metal surfaces [106,107]. An adsorbate with a single valence state $|a\rangle$ of energy ε_a approaches and interacts with a surface, which is described by a continuum of one-electron states $|k\rangle$ of energies ε_k. The basis set $\{|a\rangle, |k\rangle\}$ is used to expand the states $|n\rangle$ of the Hamiltonian H of the combined surface-adsorbate system. The basis is assumed complete and orthonormal. The states of the combined system are expressed as

$$|n\rangle = c_a|a\rangle + \sum_k c_k|k\rangle \qquad (2.21)$$

with c the coefficients of the linear combination. The projection $g_a(\varepsilon)$ of the DOS on the adsorbate state maps out the development of the state as the adsorbate approaches the surface

$$g_a(\varepsilon) = \sum_n \left|\langle n|a\rangle\right|^2 \delta(\varepsilon - \varepsilon_n) \tag{2.22}$$

where ε_n is the energy of the n-th eigenstate of the interacting system. After mathematical manipulation, which involves the use of the Green's function, the projected density of states (PDOS) is rewritten as [106,107]

$$g_a(\varepsilon) = \frac{1}{\pi} \frac{\Delta(\varepsilon)}{\left(\varepsilon - \varepsilon_a - \Lambda(\varepsilon)\right)^2 + \Delta(\varepsilon)^2} \tag{2.23}$$

where

$$\Delta(\varepsilon) = \pi \sum_k V_{ak}^2 \delta(\varepsilon - \varepsilon_k) \tag{2.24}$$

and

$$\Lambda(\varepsilon) = \frac{\wp}{\pi} \int d\varepsilon' \frac{\Delta(\varepsilon')}{\varepsilon - \varepsilon'} \tag{2.25}$$

$\wp$ denotes the principal value and $V_{ak} = \langle a|H|k\rangle$. $\Delta(\varepsilon)$ can be considered as the coupling matrix element between the adsorbate state and the metal states.

Fig. 2.3 shows the bond formation process between atomic oxygen and a Pt surface. Upon interaction with the surface, the oxygen 2p state feels the combined effect of the Pt s-p and d-bands. Both of the bands are assumed nearly constant. Under this assumption, the matrix element V_{ak} is also constant and the shape of $\Delta(\varepsilon)$ reflects the shape of the band (Eqn. 2.24). The bond formation can be described as a two-step process:

1. First, interaction with the broad s-p band leads to the broadening of the atomic state. This corresponds to the limiting case of *weak chemisorption* of the Newns-Anderson model ($V_{ak} \leq W$, where W is the width of the band). The PDOS $g_a(\varepsilon)$ assumes the form a broad Lorentzian. The coupling with the s-p states makes the biggest contribution to the bond energy. It has also the biggest effect on the bond length and geometry of the adsorbate.
2. Switching on the interaction between the narrow d-band and the renormalized atomic state leads to the splitting of the latter into two narrow bonding and antibonding states. This situation corresponds to the *strong chemisorption* limit of the Newns-Anderson model ($V_{ak} \geq W$). The interaction can be roughly viewed as a two-level coupling.

Interaction between molecular species and metal surface is treated in a similar fashion. For example, for CO, bonding is described by treating the interaction between the metallic states and the 5σ and 2π orbitals of CO separately (Fig. 2.4). The 5σ and 2π states shift down in energy and broaden upon interaction with the s-p band of an Al surface. The renormalized molecular states split into bonding and antibonding levels upon interaction with the d-band of a Pt surface. There is a small contribution from the 5σ state to the Pt-CO bond as there are only a few states above the Fermi level. On the other hand, the contribution of the 2π state is significant with only its bonding region to be occupied.

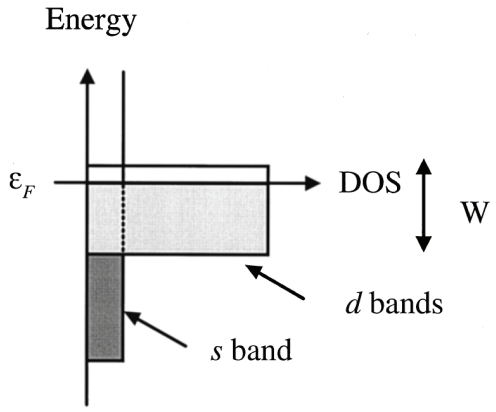

Fig. 2.2 Schematic illustration of the density of states of a transition metal. The broad s band and the narrow d-bands (of width W) are filled up to the Fermi level, ε_F [108]..

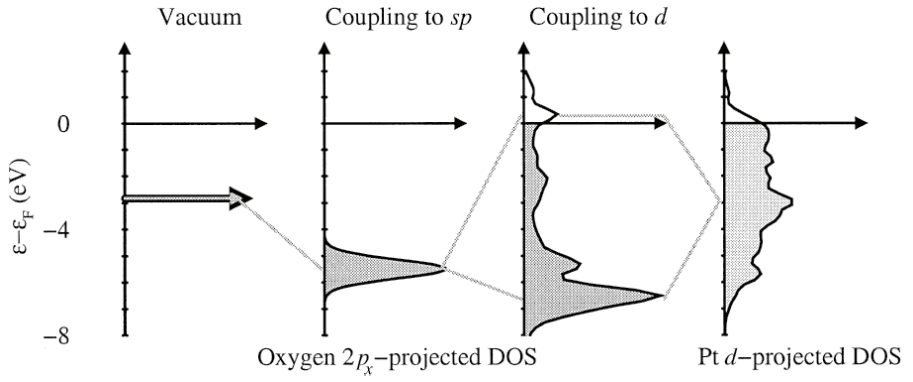

Fig. 2.3 Schematic illustration of the change in local electronic structure at an oxygen atom upon adsorption on Pt fcc(111) [108].

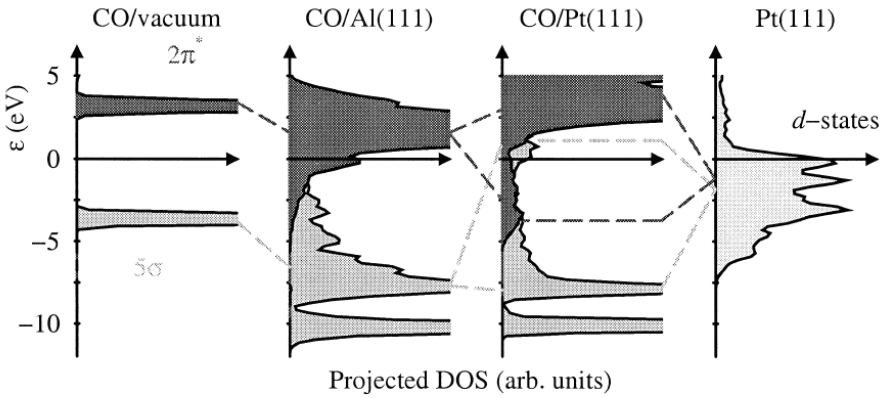

Fig. 2.4 The self-consistent electronic DOS projected onto the 5σ and 2π* orbitals of CO, in vacuum and on Al fcc(111) and Pt fcc(111) surfaces [108].

The d-band model

Fig. 2.5 illustrates how chemisorption varies from one TM to the next. The d-band model is used to relate change in chemisorption with change in the energy center of the d-band [109-115].

The coupling with the s-p states varies only slightly among the TMs. The energy contribution caused by the coupling with the d-electrons is expressed by [111]

$$E_{d-hyb} = -2(1-f)\frac{V^2}{|\varepsilon_d - \varepsilon_a|} + 2(1+f)aV^2 \quad (2.26)$$

For deriving the above expression, it was assumed that $S = -aV$ (on the grounds of the exponential decay of the WFs). The constant a is assumed to be metal-independent. Eqn. 2.26 demonstrates that the d-band center ε_d, the coupling matrix element V and the d-band fractional filling f are properties which control the interaction between the d-states and the renormalized (by the s-p interaction), adsorbate state ε_a.

DFT calculations demonstrate that the d-band can largely be characterized by its center (Fig. 2.6) [108]. In this thesis, the d-band center is calculated from atomic orbital PDOS. The general expression for the DOS $n(\varepsilon)$ of a system is

$$n(\varepsilon) = \sum_n \langle \psi_n | \psi_n \rangle \delta(\varepsilon - \varepsilon_n) \quad (2.27)$$

The sum runs over all WFs. Under the PAW formalism, the surface DOS is projected onto the all electron partial waves φ_i^a that correspond to the d-orbitals of a surface atom a [87]

$$g_d^a(\varepsilon) = \sum_i \sum_n \left| \langle \varphi_i^a | \psi_n \rangle \right|^2 \delta(\varepsilon - \varepsilon_n) \quad (2.28)$$

The d-band center ε_d and width W_d are calculated as the first and second moment of the distribution

$$\varepsilon_d = I^{-1} \int d\varepsilon g_d^a(\varepsilon) \varepsilon \quad (2.29)$$

and

$$W_d = I^{-1} \int d\varepsilon g_d^a(\varepsilon) (\varepsilon - \varepsilon_d)^2 \quad (2.30)$$

where

$$I = \int d\varepsilon g_d^a(\varepsilon) \quad (2.31)$$

For example, the d-band centers ε_d for W, Ru and Pt are calculated with GPAW as -0.50eV, -1.65eV and -2.18eV with respect to the Fermi level (Table S2 in Paper I Sup. Inf.) The trend in the calculated centers reflects the gradual filling of the d-band when moving from left to right along the periodic table [108].

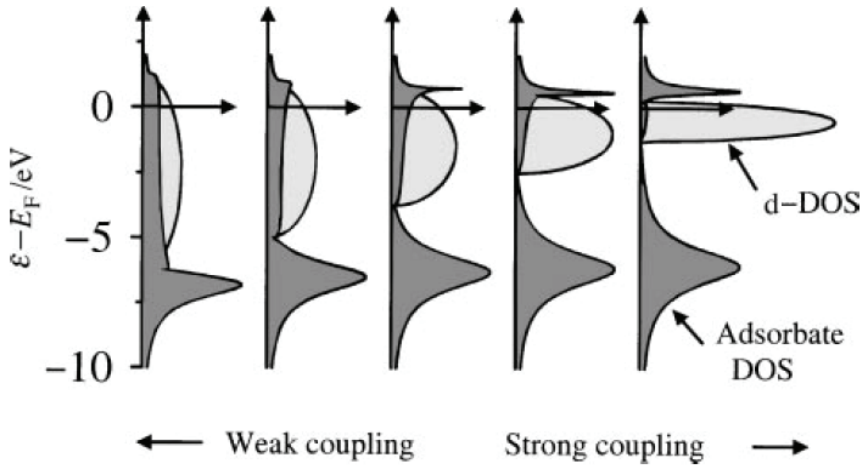

Fig. 2.5 The local density of states projected onto an adsorbate state interacting with the d-band [116].

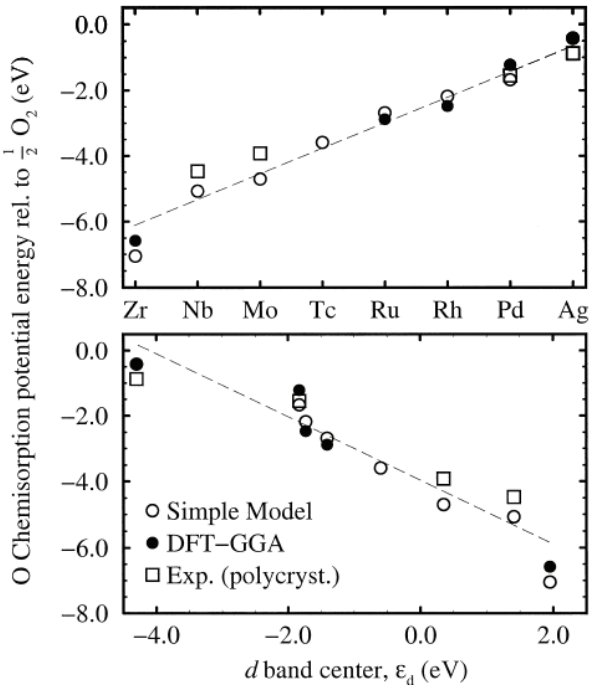

Fig. 2.6 Trends in surface reactivity [108].

3. Evaluating electro-catalytic performance

This chapter builds on the models and fundamental theory presented in Chapter 2. It presents methods for the evaluation of electro-catalytic performance using electronic structure calculations. Approximations and assumptions are discussed.

Model fuel cell electrodes

Model flat, stepped and kinked surfaces [34,117,118], bulk, surface and near-surface alloys [39,119,110,120,121], clusters and nanoparticles [58,122], have been used for modeling catalyst structures. The model structures constructed for the purposes of this thesis are presented below.

Nanoparticles

In Paper III, the ORR is studied on catalytic nanoparticles. The nanoparticles were modeled as clusters of atoms. The Wulff construction is a model for clusters of equilibrium shape [123]. It is based on the idea that the optimal shape is the one that minimizes of the surface free energy Φ. The function to be minimized is

$$\Phi = \int_f \gamma^f dA \qquad (3.1)$$

where γ^f represents the surface free energies of the individual particle facets f. The Wulff theorem suggests that the optimal shape is achieved when the distance of each facet from the center of the particle is inversely proportional to the corresponding surface free energy.

Complete knowledge of the orientation dependence of the free energy is difficult and an assumption is made on which families of surface planes bound the cluster. The morphology of real nanoparticles hardly matches the ideal Wulff construction (Fig. 3.1). Real nanoparticles exhibit features such as steps, kinks and other irregularities [10,124-126], which the Wulff construction does not describe.

Catalytic activity depends on the microstructure of the surface [38,45,127,128]. A model was presented in the work of Greeley et al. [58] for the study of particle size effects for the ORR on Pt. Catalytic nanoparticles were modeled as ideal Wulff constructions. In Paper III, the previous model is refined by considering the presence of surface defects. Nanoparticles were modeled as

truncated octahedra (TO) with only the <100> and <111> facets present. The value for the ratio between the respective surface free energies of $\gamma^{100}/\gamma^{111}$ = 1.189 was taken from the work of Vitos et al. [129] Given that the equilibrium dissolution potential and the coordination number of dissolving atoms are correlated [130], every Pt atom on the particle surface was considered to be an active site with the exception of the edge and corner atoms which are expected to dissolve in solution at relatively low potentials. Two step sites were then assumed for each dissolved atom. Model nanoparticles with a diameter ranging from ca. 2nm to 30nm were generated with use of the ASE environment [131]. No support effects on the particle size were considered [132].

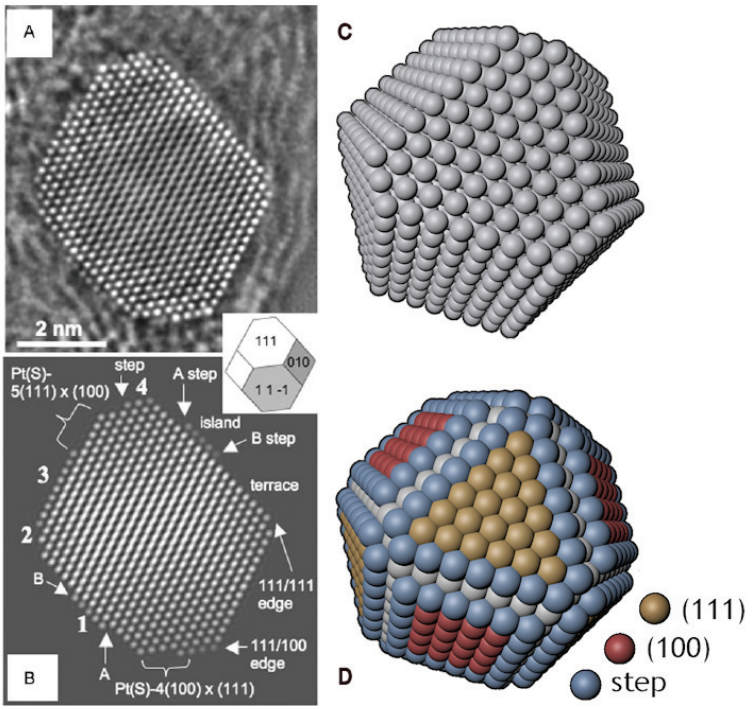

Fig. 3.1 a) High-resolution transmission electron microscopy image of a 6nm Pt particle [125], b) best-fitting simulated phase [125], c)Wulff construction with <100> and <111> facets and d) the Wulff construction used in Paper III, with the active sites considered shown.

Surfaces

The Wulff construction-based model was used only as a geometrical model for estimating the population of the different active sites (Table S1 in Paper III Sup. Inf.) No calculations of the clusters were performed. Because of the electrostatic screening of the metal electrons, any one facet has generally no effect on the energetics of any other. This allows for treating each facet independently. Calculations of extended surfaces are performed instead [58]. This way, the computational burden is greatly reduced. The number of atoms per unit cell needed to construct such model structures is smaller compared to this of one cluster. For comparison, a Pt TO particle of a diameter of 4nm comprises ca. 6500 atoms whereas its activity was calculated on the basis of model 3-layer slabs of 12 atoms only (see Paper III). Slab models were used to describe all the catalytic surfaces in Papers I and II.

Bulk structures

Calculation of bulk structures of TMs and TM-based alloys were performed in connection with the calculation of lattice parameters later used to construct model surfaces of the same material. Table 3.1 summarizes the optimized lattice constants a_0 of bulk TMs, calculated with use of the RPBE xc functional. For the hcp metals the axial ratio (c/a) was fixed to the experimental value of 1.63. The magnetic moments for Co, Ni and Fe were calculated 1.73, 0.70 and 2.35, respectively.

	Ru	Co	Pt	Ni	Pd	Rh	Ag	Cu	Au	Ir	W	Mo	Fe
Lattice	hcp	hcp	fcc	fcc	fcc	fcc	fcc	fcc	fcc	fcc	bcc	bcc	bcc
a_0(Å)	2.75	2.53	4.00	3.55	3.99	3.88	4.22	3.69	4.21	3.91	3.22	3.18	2.89

Table 3.1 Calculated (RPBE) lattice constants of bulk transition metals.

Gas-phase molecular species

Calculation of gas-phase molecules were performed in unit cells, large enough (typically 8-10Å) to ensure the smooth decay of the WFs. No periodic boundary conditions were imposed. For closed-shell molecules containing a O-C-O backbone (as in the case of HCOOH and CO_2) the calculated energy was corrected by +0.45eV, an empirical correction based on a number of reactions studied with the RPBE functional [133].

Estimating activity

In the following, the example study of ORR on Pt and other TM closed-packed surfaces demonstrates the procedure of estimating electro-catalytic activity.

Computational hydrogen electrode

For a chemical reaction occurring on the surface of an electrode, applied electrical potential affects the free energy of the reaction. An intuitive concept for modeling the effect of potential has been introduced by Nørskov et al. [60], referred as the *computational hydrogen electrode* (CHE). The CHE serves as the computational analogue of the *standard hydrogen electrode* (SHE). The SHE is the primary reference electrode for measuring the potential of all other electrodes. It is defined through the electrode reaction

$$H^+ + e^- \rightarrow \tfrac{1}{2}H_{2(g)} \qquad (3.2)$$

$H_{2(g)}$ is at unit fugacity and H^+ is at unit activity. The chemical potential of a proton-electron pair $\mu(H^+) + \mu(e^-)$ is related to the chemical potential $\mu(H_2)$ of gaseous hydrogen through the expression

$$\mu(H^+) + \mu(e^-) = \frac{1}{2}\mu(H_2) \qquad (3.3)$$

The potential of the SHE is defined to be zero at standard conditions. The absolute potential of the SHE is estimated 4.44±0.02V at 298K [134].

The atomic-scale simulation needed to calculate the free energy of solvated protons is not well defined [135]. This technicality is circumvented by use of the CHE. For an electrochemical reaction that involves the transfer of n proton-electron pairs

$$R + n(H^+ + e^-) \rightarrow P \qquad (3.4)$$

the free energy ΔG of the reaction is expressed as

$$\begin{aligned}\Delta G &= \mu(\mathrm{P}) - \mu(\mathrm{R}) - n\left[\mu(\mathrm{H}^+) - \mu(\mathrm{e}^-)\right] \\ &= \mu(\mathrm{P}) - \mu(\mathrm{R}) - \frac{n}{2}\mu(\mathrm{H_2}) \\ &= \Delta G^o - neU + 2.303RT\mathrm{pH}\end{aligned} \tag{3.5}$$

with ΔG^0 denoting the standard free energy of the reaction. The second term in the right part of Eqn. 3.5 describes the effect of the potential U of the half-cell on the chemical potential of the electrode electrons. The energy is shifted down by eU for each electron involved in the process. The last term describes the dependence of the reaction free energy on the concentration of solvated protons in the electrolyte. The CHE enables the computational study of the electrochemical reaction occurring on each of the FC electrodes in isolation.

Calculation of reaction and adsorption free energies

Quoting Trasatti: "...electrocatalysis can be expressed, to a first approximation, in terms of bond strength between the electrode surface and reaction intermediates" [136]. The adsorption free energy quantifies the strength of the surface-adsorbate bond. The CHE was routinely used to calculate reaction and adsorption free energies in this thesis. For demonstrating the methodology, the free energy of one intermediate step of the ORR will be calculated. The reduction of hydroxyl (OH) to water is described by the reaction

$$\mathrm{OH^* + H^+ + e^- \rightarrow H_2O_{(l)} + *} \tag{3.6}$$

Using the CHE, the adsorption free energy of OH is calculated from the free energy of the reaction

$$\mathrm{H_2O_{(l)} + * \rightarrow OH^* + \tfrac{1}{2}H_{2(g)}} \tag{3.7}$$

and vice versa. The adsorption energy ΔE_{OH} of OH is calculated as

$$\Delta E_{\mathrm{OH}} = E_{\mathrm{surface\text{-}OH}} - E_{\mathrm{surface}} - E_{\mathrm{H_2O}} + \frac{1}{2}E_{\mathrm{H_2}} \tag{3.8}$$

where $E_{\mathrm{surface\text{-}OH}}$, E_{surface}, $E_{\mathrm{H_2O}}$ and $E_{\mathrm{H_2}}$ are the DFT calculated total energies of OH adsorbed on the surface, the clean surface, gas-phase water and hydrogen molecules, respectively. Gas-phase water is assumed to be in equilibrium with liquid water (pressure 0.035bar at 298K).

The calculated energies correspond only to the electronic component of the energy. Additional contributions to the energy from the translational, rotational and vibration modes are considered. The estimation of thermodynamic properties from electronic structure calculations is well described [52,137,138]. For adsorbed species, the frustrated translational and rotational modes are described by vibrational modes [139]. The combined contribution is approximated by the zero-point energy (ZPE)

$$ZPE = \sum_i \frac{h\nu_i}{2} \tag{3.9}$$

where h is the Planck's constant and ν_i is the frequency of the i-th normal mode of vibration. The frequencies ν_i are calculated from the mass-weighted Hessian matrix of the system within the harmonic approximation [138]. ASE/GPAW builds the Hessian matrix using a 7-point cross FD stencil, which corresponds to atom displacements of 0.01Å. Egg-box effects are minimized by imposing momentum conservation in each direction [94].

Further corrections are applied for the calculation of the free energy that corresponds to the operating conditions of a low-temperature FC. The entropy corrections are calculated from the entropy contribution S of each of the vibrational modes. In the harmonic normal mode approximation

$$S = k_B \sum_i \left(\frac{x_i}{e^{x_i} - 1} - \ln\left(1 - e^{-x_i}\right) \right) \tag{3.10}$$

with $x_i = h\nu_i / k_B T$, where k_B is the Boltzmann constant. The correction $\int C_p dT$ related to enthalpy is assumed negligible. The respective corrections for the clean surface are assumed negligible, i.e. $G_{surface} \approx E_{surface}$. Putting everything together, the adsorption free energy of OH is given with respect to the gas-phase energy of H_2O and H_2 by the following expression

$$\begin{aligned} \Delta G_{OH}(U) = {} & E_{surface\text{-}OH} - E_{surface} - E_{H_2O} + \frac{1}{2} E_{H_2} \\ & + ZPE_{surface\text{-}OH} - ZPE_{surface} - ZPE_{H_2O} + \frac{1}{2} ZPE_{H_2} \\ & - T\left(S_{surface\text{-}OH} - S_{surface} - S_{H_2O} + \frac{1}{2} S_{H_2} \right) \\ & - eU \end{aligned} \tag{3.11}$$

or in a more compact form

$$\Delta G_{OH}(U) = \Delta E_{OH} + \Delta ZPE_{OH} - T\Delta S - eU \tag{3.12}$$

The pH of the electrolyte is assumed equal to zero corresponding to the acidic environment of the electrode.

The numerical values for the corrections relevant to both the gas and liquid-phase reaction species are taken from the work of Ferrin et al. [63], reproduced in Table 3.2. Tabulated data were used for the entropy corrections corresponding to gas-phase molecules [140].

Modeling the electrochemical environment

Modeling catalysis in the electrochemical environment of the FC requires a model for the interface between the electrode and the electrolyte [141]. Experiments under high vacuum conditions have suggested that water adsorbs on Pt fcc(111) as an hexagonal water layer parallel to the electrode surface [142]. Calculations have found the same structure at potentials relevant for the ORR [24]. In this case, the coverage of the ORR intermediates is 1/3 of a monolayer (ML). Every two reaction intermediates are separated by a water molecule (Fig. 3.2).

Modeling the water environment explicitly, increases the computational burden. Alternatively, its effect on the adsorption free energies is calculated for one surface or a few surfaces and then applied as a correction for every other surface in the same study set. Both OH and OOH are stabilized significantly through hydrogen bonds with the water. For OH, Eqn. 3.12 is rewritten as

$$\Delta G_{OH}(U) = \Delta E_{OH} + E_{OH,w} + \Delta ZPE_{OH} - T\Delta S - eU \tag{3.13}$$

where $E_{OH,w}$ is the water correction corresponding to the stabilization of OH on the surface. For TM close-packed surfaces the correction for OH and OOH was calculated ca. -0.30eV for adsorption on top of Pt atoms [60].

The electrochemical double layer on the electrode gives rise to a field that interacts with the adsorbed species. Such field effects were neglected as they affect the model only slightly [143].

In Paper I, the water correction was calculated from a set of chalcogen-modified Ru and Rh surfaces and then applied to all other TM chalcogenides studied. In Paper II, the adsorption energies of OH and all R-OH MOR intermediate species were corrected by -0.15eV and -0.25eV, respectively. In Paper III, the effect of the particle edge on the energetics of the neighboring facets is studied on the assumption that the ORR intermediates are embedded in a half-dissociated network of water molecules.

Intermediate	TS	ZPE	$T\Delta S$	ΔZPE
$CO_{2(g)}$	-0.66	0.31		
$H_{2(g)}$	-0.40	0.27		
$H_2O_{(l)}$	-0.67	0.56		
$CH_3OH_{(g)}$	-0.74	1.36	0.45	0.79
$CH_2O_{(g)}$	-0.68	0.70	0.12	0.40
$HCOOH_{(g)}$	-0.77	0.70	0.29	0.12
CH_2OH^*	-0.05	1.10	0.95	0.66
CH_3O^*	-0.03	1.04	0.97	0.61
$CHOH^*$	-0.03	0.78	0.76	0.49
CHO^*	-0.03	0.43	0.56	0.27
COH^*	-0.03	0.47	0.56	0.31
CO^*	-0.05	0.17	0.34	0.15
OH^*	-0.04	0.31	0.43	-0.11
O^*	-0.04	0.07	0.22	-0.22
$C(OH)_2$	-0.05	0.77	1.01	0.19
$COOH^*$	-0.07	0.61	0.78	0.16
$CHOO^*$	-0.05	0.61	0.80	0.17
H_2COO^*	-0.02	0.86	1.04	0.28
H_2COOH^*	-0.03	1.06	1.24	0.34

Table 3.2 Corrections with respect to the gas-phase of the H_2O, H_2 and CO_2 molecules [63,140].

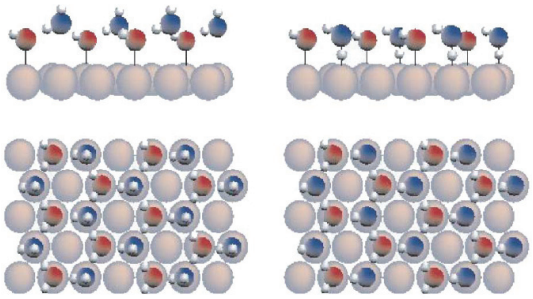

Fig. 3.2 Water bilayer structures on Pt fcc(111) [142].

Construction of reaction free energy diagrams

Reaction free energy diagrams such as the one shown in Fig. 3.2 have been used to acquire mechanistic insights into chemical reactions [63,144-147]. The reaction free energy diagram of Fig. 3.3 describes the ORR on Pt fcc(111) for different electrode potentials. The x-axis indicates how many proton-electron pairs have been transferred. As DFT calculations of O_2 are problematic [148], the thermodynamic value of 4.92eV was used for the overall Gibbs free energy

change for the reaction. The above approach is equally applicable to the study of the dissociative mechanism [60].

The ORR under realistic conditions involves many more species than the set of intermediates chosen to construct the reaction free energy diagram. For example, no transition states were described here. The reaction pathway is sampled as finely as necessary for calculating properties such the overpotential with adequate accuracy while keeping the complexity of model as low as possible. In all included Papers, the reaction paths were sampled finely enough for a semi-qualitative comparison with experiment. In any case, linear relationships between adsorption energies and the activation energy needed to create a transition state have been established (the so-called Brønsted-Evans-Polanyi relations) [149-151].

Fig. S3 in Paper I Sup. Inf. shows the reaction free energy diagram for the ORR on Pt and Ru elemental close-packed surfaces as well as two Ru chalcogenide surface alloys. In Fig. S3 in Paper II Sup. Inf. the reaction free energy diagram for the MOR over a Cu_3Pt surface alloy is shown.

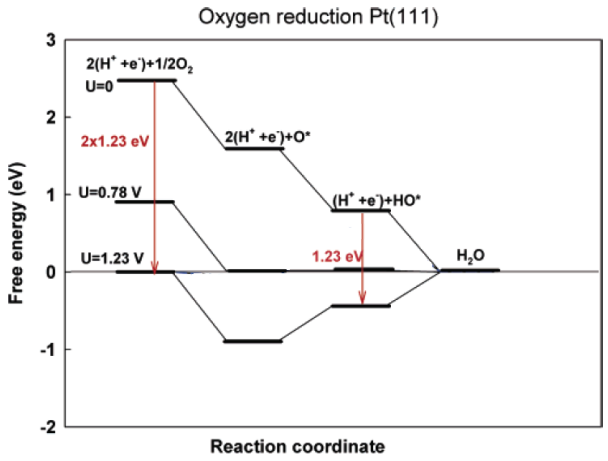

Fig. 3.3 Free energy diagram for the oxygen reduction reaction on Pt fcc(111) for different electrode potentials U [60].

Estimation of reaction overpotential

An estimation of overpotential for a reaction is made using the respective reaction free energy diagram. The highest positive change in energy ΔG_{max} along the reaction pathway at a given potential U is defined as

$$\Delta G_{max}(U) = \max\{\Delta G_i(U)\} \tag{3.14}$$

where ΔG_i is the free energy for the i-th reaction intermediate step. For the ORR, the absolute value of the overpotential is estimated as $\eta_{ORR} = |U_{ORR} - U^o|$ where the *ORR potential* U_{ORR} corresponds to the highest potential U for which the change in energy between every two consecutive steps along the reaction pathway is zero or negative. The above statements are compactly formulated as

$$\eta_{ORR} = \Delta G_{max}(1.23V)/e \tag{3.15}$$

and

$$\Delta G_{max}(U_{ORR}) = 0 \tag{3.16}$$

Fig. 3.3 shows the ORR pathway on Pt fcc(111) for three different electrode potentials, $U = 0$, $U = 0.78\text{V}$ and $U = 1.23\text{V}$. The first corresponds to the reaction running by short circuiting the FC, the second to a DFT value for the U_{ORR} [60], and the last to the theoretical maximum value. For $U =$ 1.23V, two proton-electron transfer steps are characterized by an uphill step in the free energy. The term *potential-determining step* (PDS) is used to describe the reaction intermediate step that shows the highest energy difference. In the case of Pt, the PDS is the oxidation of OH to water and $\Delta G_{\text{max}}(1.23\text{V}) = 0.45\text{eV}$. OH therefore can be considered as a poisoning species, blocking the active sites of the surface. The potential $U_{\text{ORR}} = 1.23 - 0.45\text{V} = 0.78\text{V}$ is the highest for which no reaction step is uphill. The calculated value of 0.78V is in agreement with experiments [152]. In the potential region of U_{ORR}, a peak is found in the cyclic voltammogram corresponding to acidic environment (Fig. 3.4). The peak describes the saturation of the surface with hydroxyl species.

In Paper I, the above procedure was used for the estimation of the overpotential associated with each of the elemental and chalcogen-modified TM surfaces. In a similar fashion, in Paper II, the overpotential for the MOR is estimated from the *MOR potential* U_{MOR} corresponding to the minimum potential U for which at least one reaction channel opens

$$U_{MOR} = \min\left\{\Delta G_{\text{max}}(0)/\text{e}\right\}_j \tag{3.17}$$

where j runs over the possible pathways (Fig. 1.2). Since the direct path will mostly contribute to the anode's current only after the removal of the poisoning CO from the surface, it is the potential U^j_{MOR} corresponding to the indirect path that it is used as estimation for the reaction overpotential.

A word of caution follows. The estimated overpotential is not always directly comparable to experiment where surface poisons, diffusion barriers, and kinetic effects can affect the electrode current.

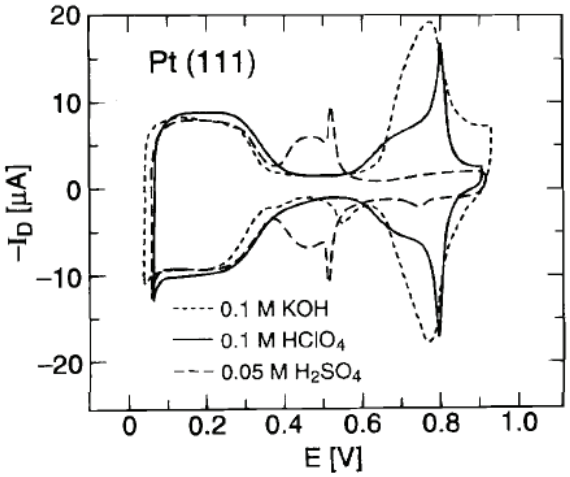

Fig. 3.4 Voltammetry of the Pt (111) disk electrode in different electrolytes [152].

Trends in reactivity

Abild-Pedersen et al. [153] established with DFT calculations, approximate *linear relationships* for the adsorption energies of hydrogen-containing molecules on TM surfaces. Linear relationships have been established and used in computational catalysis studies [154,155,63,156,151,157,121].

Fig. 3.5 shows how the adsorption energy ΔE_{AH_x} of a molecule AH_x scales with the adsorption energy ΔE_A of atom A . The correlation is expressed as a linear relationship

$$\Delta E_{AH_x} = \gamma \Delta E_A + \xi \tag{3.18}$$

where ξ a constant. The slope γ is given to a good approximation by

$$\gamma(x) = \frac{x_{max} - x}{x_{max}} \tag{3.19}$$

where x_{max} is the maximum number of bonds atom A can create.

The d-band model and effective medium theory [158] arguments were used to rationalize the trends. The d-band acts as a mediator for these correlations. Variation of adsorption energies reflects variation of the d-band features from one metal to the other.

Eqn. 3.19 formulates a generalized bond-counting argument, which can be used to rationalize the slopes of the linear relationships given in Table S5 in Paper II Sup. Inf. The adsorption free energy ΔG_{CHOO} of the O-bound CHOO scales with the adsorption free energy ΔG_{OH} of OH with a slope of 0.99. Both bind to the surface with the formation of one bond between oxygen and the surface. The adsorption free energy ΔG_{COH} of the C-bound COH scales with the adsorption free energy ΔG_{CO} with a slope of 1.53. COH forms a triple bond with the surface whereas the latter forms a double bond, i.e. γ = 3 /2 = 1.5. In the case of the C-bound COOH, the slope is calculated 0.77. A value closer to 0.5 would have been expected. This is a reminder that the scaling relationships are only approximate.

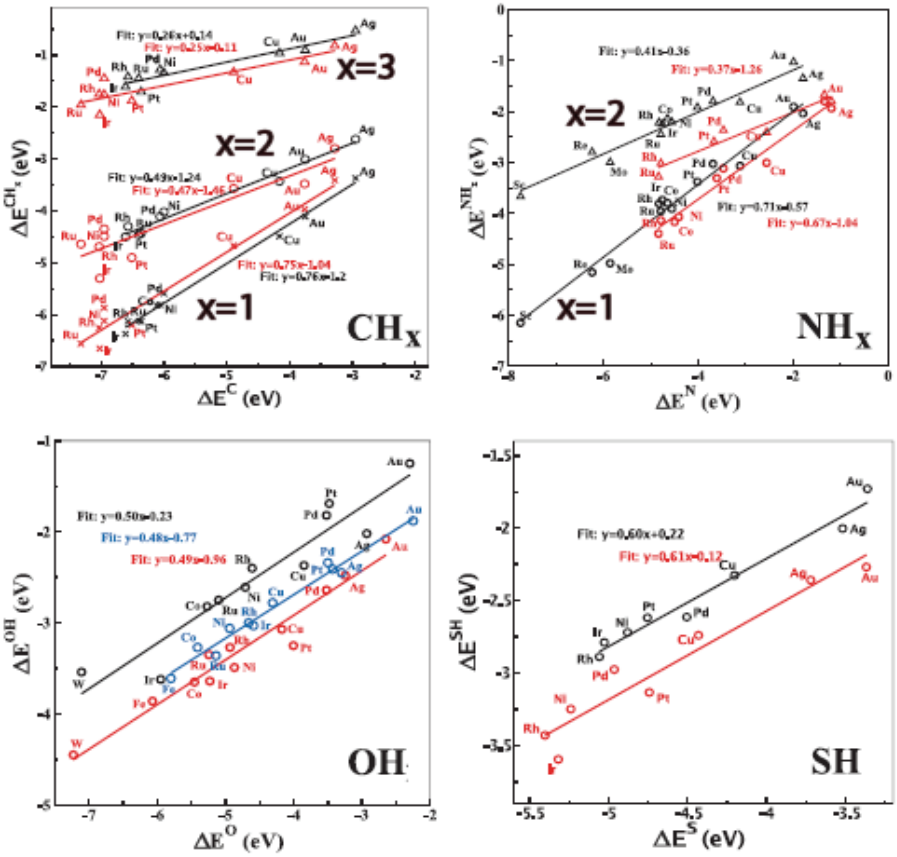

Fig. 3.5 Adsorption energies of CH_x, NH_x, OH, and SH intermediates, plotted against adsorption energies of C, N, O, and S, respectively, on close-packed (black) and stepped (red) surfaces [153].

Descriptors of reactivity and volcano-shaped plots

Trends in catalytic activity can be described by plots where the activity is shown against a suitable descriptor. Parsons [159], Trasatti [136] and Bockris [160] have constructed activity plots using adsorption energies as *reactivity descriptors*. A maximum in activity exists for an optimal value of the descriptor (adsorption energy). Such *volcano plots* give mechanistic insights into the reactions and reveal trends in activity of different catalysts [55,63,147,161-164].

In Fig. 3.6, the calculated ORR activity on close-packed TM surfaces is plotted as a continuous function of a single descriptor [60]. Using scaling relationships for the ORR intermediates, the reaction free energies ΔG_i are expressed as functions of the adsorption energy ΔE_O of oxygen. Effectively, the overpotential η_{ORR} is described as function of the adsorption energy of oxygen

$$\eta_{ORR} \propto \Delta G_{max} \propto \Delta G_O \propto \Delta E_O \tag{3.20}$$

There is a direct connection between the potential U_{ORR} and the ORR activity [165]. On the assumption of a single rate-limiting step, the rate $k(U)$ of the overall reaction for an electrode potentia U, is given by the Arrhenius equation [19]

$$k(U) = k_0 e^{-\Delta G_{max}(U)/k_B T} \tag{3.21}$$

The pre-exponential factor k_0 describes the transfer of a solvated proton to the surface [166]. The reaction is considered to take place under out-of-equilibrium conditions, the typical case for FC operation. The rate of the reaction can be converted into the current density (specific activity) $i(U)$, which is described by a Tafel type equation

$$i(U) = i_0 e^{-\Delta G_{max}(U)/kT} \tag{3.22}$$

with i_0 = 96mA cm^{-2} [60]. For $U = U_{ORR}$, $\Delta G_{max} = 0$. The exponential becomes unit and the current density maximizes.

The two legs of the activity volcano of Fig. 3.6 describe the situation of two different rate-limiting reaction steps. For surfaces lying on the left leg of the volcano, the ORR activity is limited by the proton-electron transfer to OH. This is the case of Pt. For surfaces lying on the right leg, catalytic activity is controlled by the proton-electron transfer to the adsorbed O_2. It is noted that violation of the assumption of a single rate-limiting step flattens the peak of the volcano plot [161].

The example study of the ORR on TMs is used here to introduce the concepts. Introducing scaling relationships and reactivity descriptors does simplify the problem. Calculating activity with a full set of calculations for each surface is realistic. The reaction path is sampled with three intermediate species. The potential of scaling relationships in simplifying is better demonstrated with the MOR, which involves 15 intermediates. Fig. 2 Paper II shows MOR potential that corresponds to the indirect path, plotted against a set of two reactivity descriptors: the adsorption free energy of OH and CO. Each corresponds two one of the two separate sets of scaling relationships that are established and used for the construction of the volcano plot. One set describes correlations among O-bound species and the other one correlations among C-bound species (Fig. 3 in Paper II).

A low value for U^i_{MOR} does not necessarily go hand-in-hand with experimentally measured high activity. The volcano plot was not derived from a reaction kinetic model [161]. No pre-exponential

factors were considered. Moreover, the acidic environment of the FC may render the catalyst completely ineffective because of stability issues.

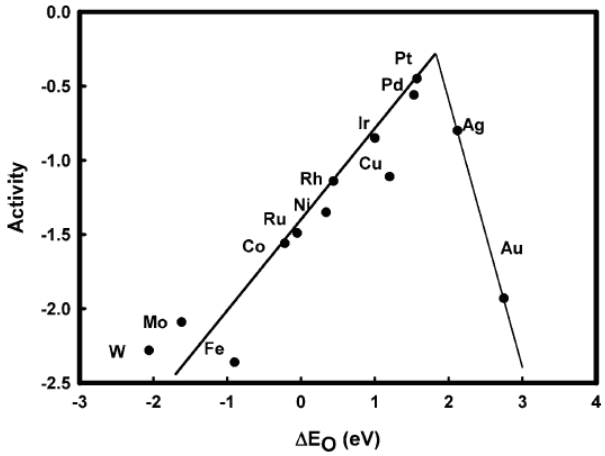

Fig. 3.6 Trends in oxygen reduction activity [60]. The activity volcano plot is constructed from linear relationships. Points represent the DFT calculated activities.

Efficient catalysis

The combined use of linear relationships and reactivity descriptors open up the possibility of fast screening for efficient catalysts [120,154,167]. The top of the volcano plot can accommodate only a relatively small number of structures. With the calculation of a small number of adsorption energies (e.g. two in Paper II) less effective catalysts can be quickly identified and discarded.

Is there an electro-catalyst that could lie at top of the volcano?

At the top of the volcano, adsorption energies assume intermediate values. Adsorbates bind neither too strongly nor too weakly to the surface, a manifestation of the Sabatier principle [168]. An efficient catalyst binds reaction intermediates strongly enough so it can activate the reactants but still weakly enough that the products can leave the catalyst surface. In that sense, Pt is an *efficient* ORR electro-catalyst. It is positioned close but not exactly at the top of the volcano plot of Fig 3.6. There is still room for improvement [120].

Is there an electro-catalyst with zero overpotential?

Fig. 3.6 hints a fundamental upper limit of the activity for the ORR on elemental TM surfaces. The difference between the adsorption energies of OH and OOH is fixed to ca. 3.2eV. In other words, the adsorption energies of OH and OOH cannot vary independently.

The ideal ORR catalyst would require this difference to be twice the equilibrium potential, i.e. 2.46eV. The reaction free energy diagram of the ideal ORR catalyst is shown in Fig. 3.7. In that case, $\Delta G_i(1.23V) = 0$. Such a catalyst would lie at 0 in Fig. 3.6. This does not happen for any of the elemental TM surfaces. The lowest overpotential is calculated (3.2 - 2.46) eV / 2e ≈ 0.4V.

Each of the volcano plots constructed in the thesis corresponds to a single class of electro-catalysts. Here, the term *class of catalysts* is used to describe a set of surfaces which

1. are described by a common reaction mechanism
2. share the same scaling relationships for adsorption energies of the reaction intermediates

The volcano plot of Fig. 3.6 implies that elemental TM surfaces are considered as one class of electro-catalysts for the ORR. Defining a class of catalytic materials implies tolerance to deviation from the linear relationships. The applicability of the model and its assumptions is validated by comparison with experiments.

As it is shown later, none of the classes of the catalytic surfaces studied in this thesis escapes the limiting nature of the scaling relationships.

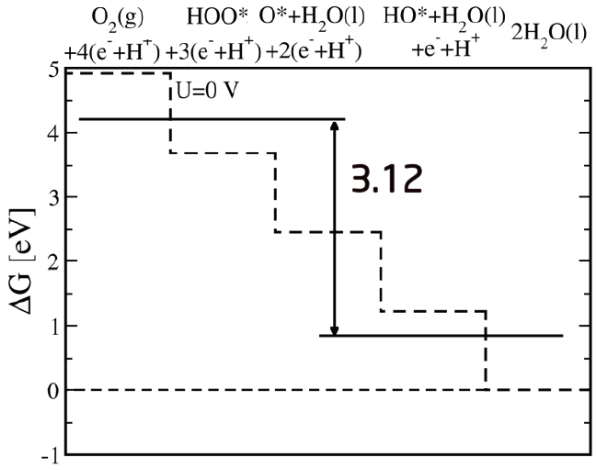

Fig. 3.7 Free energy diagram for the oxygen reduction reaction (dashed line). For elemental transition metals, the energy levels of OH and OOH are fixed to ca. 3.2eV. Even if ideally positioned (black line) the lowest overpotential is ca. 0.4V.

Evaluating stability

DFT has been used for evaluating catalyst stability [12,130,167,169].

In Paper I, evaluation of stability concerns the study of segregation and phase separation effects of TM chalcogenide surfaces. In some cases, the chalcogen atoms are found to relax out of the surface. The surfaces flatten on adsorption. The energy barrier for the surface flattening is calculated with NEB [170] to be within DFT error (of the order of 0.05eV). Thus, only flat surfaces are studied in Paper I. It should be added that even if a catalytic surface is not thermodynamically stable, it can still be kinetically stable under FC operation [171].

In Paper II, while screening for efficient TM-based electro-catalysts the MOR, the stability of every candidate alloy surface is evaluated in terms of resistivity to dissolution and oxidation effects. The surface is considered unstable if the lowest potential U_{MOR} is higher than the standard reduction potential of either of the constituent pure metals. For the reduction potentials, the experimental values corresponding to the bulk phases are used as an approximation [140], presented in Table 3.3. The promising (as suggested by the screening) MOR catalysts Cu_3Pt and Pt_2Cu/Pt are evaluated for their stability against segregation effects. The energy change associated with swapping Pt atoms with nearest neighbor Cu atoms is calculated. Andersson et al. [119] has shown that CO adsorption at elevated pressure and temperatures can pull to the surface the less reactive Cu of a CuPt near-surface alloy. With this study in mind, the stability of the aforementioned alloys against adsorption-induced segregation is also checked.

In Paper III, the concept of surface stability becomes of central importance. Edge and corner atoms are assumed to dissolve in solution giving rise to steps. The computational work of Greeley [130] explores periodic trends in the reversible deposition/dissolution potentials of admental on TM surfaces. For a species A in equilibrium with dissolved ions of standard concentration, supported on a substrate metal B, the grand canonical free energy of the system Ω is written as [169]

$$\Omega = E - \left(E_{\mathrm{A,bulk}} + ne\left(U_{\mathrm{A}}^{\mathrm{diss}} - U\right)\right)N_{\mathrm{A}} - E_{\mathrm{B,bulk}}N_{\mathrm{B}} \tag{3.23}$$

where E is the total energy, $E_{\mathrm{A,bulk}}$ and $E_{\mathrm{B,bulk}}$ is the energy of a A and B atom in the bulk, n is the number of electrons transferred during dissolution of A, $U_{\mathrm{A}}^{\mathrm{diss}}$ is the standard reduction potential of A as given in the electrochemical series [140]. N_{A} and N_{B} are the number of the A and B atoms in the unit cell. Dissolution of a single A atom is associated with a change ΔΩ in free energy

$$\Delta\Omega = E_{N_{\mathrm{A}}-1} - E_{N_{\mathrm{A}}} + \left(E_{\mathrm{A,bulk}} + ne\left(U_{\mathrm{A}}^{\mathrm{diss}} - U\right)\right) \tag{3.24}$$

The shift in dissolution potential for admetals in different structural forms was estimated by requiring ΔΩ = 0. DFT was used to calculate $E_{N_{\mathrm{A}}-1}$ and $E_{N_{\mathrm{A}}}$ for structures corresponding to isolated adatoms, dimers, and extended kinks. The identified trends show that the equilibrium dissolution potential and the coordination number of the dissolving atoms are correlated.

	Ru	Co	Pt	Ni	Pd	Rh	Ag	Cu	Au	Ir	Fe
U^{diss}(V)	0.68	-0.28	0.98	-0.26	0.92	0.76	0.80	0.34	1.52	0.93	-0.05

Table 3.3 Standard reduction potentials of transition metals [140].

4. Catalytic data sets

The management of catalytic data sets is of central importance to this thesis. Approximately 2000 adsorption energies were calculated for the project of Paper II alone. The methods and tools for storing and managing the generated data are presented below.

Management of catalytic data sets

For the study of Paper II, a database containing adsorption free energies of MOR intermediates on flat and stepped TM surfaces was established. The Computational Materials Repository (CMR) module provided basic database management functionality [172,173]. With CMR

- the data generated from a calculation are collected and stored
- the sharing of data and their backup is simplified
- the analysis of the data is facilitated

As soon as a total energy calculation was completed, its details were stored in a separate file. The files were collected in a common database repository directory. CMR uses Extensible Markup Language (XML) for storing the generated data. One compressed XML file was generated per calculation. A separate repository for any one project may be used, facilitating file management. XML offers the following advantages

- it is easily extensible
- its contents are verifiable
- it is human readable
- its structure is intuitive to understand
- no extra software is needed for handling it

For data sets of the size of the database established in Paper II, the CMR module alone provides all the necessary functionality for efficiently managing the data. Access to XML data is slower compared to other data serialization formats. For big projects, the XML schema is more appropriate as a temporary storage medium, feeding data into more advanced data management systems such as the MySQL database. The XML schema used by CMR (as of revision 0.2) is made up of four different sections:

static	Information such as the user name, date and calculator name.
calculator	All input parameters to the calculator and its output.
atom	Atomic numbers, atom positions, forces.
user	User-defined attributes.

An example of the generated XML code follows

```
<static>
   <arch>x86_64</arch>
   <calculator>gpaw</calculator>
   <date>Mon Mar 22 17:02:17 2010</date>
   <energy_unit>Hartree</energy_unit>
```

There are different approaches to classifying a calculation for subsequent easy retrieval. Attributes describing the structure configuration such as atomic numbers and atom positions together with the calculator parameters and calculated energies are naturally stored in the database. Such a set of attributes defines a tight classification framework. This *taxonomy* system comes with the advantage of providing a method for classifying all the calculations in a common way. As no user input is needed, classification errors are minimized. For example, the user may ask for all stored calculations of structures which contain both Pt and Ru and have been performed with a grid spacing of $h = 0.18$Å.

A different approach, complimentary to taxonomy, is to use user-defined attributes and keywords to classify calculations. User-defined tags are used to distinguish between, for example, a calculation of a clean surface and a calculation of a species adsorbed on the surface. The flexibility offered by this *folksonomy* system greatly facilitates data retrieval. On the other hand, consideration should be given to how keywords are chosen, especially if the sharing of the data is desired. A small set of attributes and tags was used classifying the content of the catalytic database of Paper II, shown in Table 4.1. In Table 4.1, example values corresponding to a calculation of a 1/4ML of OH adsorbed on the top sites of a Pt fcc(111) surface are also given. By convention:

- a *surface* tag is used to tag surface calculations.
- a *species* tag is used to describe calculations where atomic or molecular species are included in the unit cell.

For example, the "surface" and "species" tags are used together to classify a total energy calculation of an adsorbate on a surface. By the same convention, the energy of a clean surface is retrieved by querying the database for calculations tagged with "surface" but not with "species". Appropriate keywords are also used to describe the chemical composition of the surface and the binding site of adsorbates.

Attribute	Attribute description	Example value
Description	A short description of the calculation	"Total energy calculation of fcc111 Pt surface w. OH on Top"
Element	The composition of the surface	"Pt"
Surface	The surface index	"fcc111"
Species	The adsorbed species	"OH"
Site	Binding site of the adsorbate	"Top"
Keywords	A set of tags for easy data retrieval	"gpaw", "surface", "species", "Pt", "fcc111", "OH", "Top"

Table 4.1 User-defined attributes and keywords used to classify the content of the catalytic data set of Paper II.

A toolbox for computational catalysis

The following discussion concerns exclusively the study of Paper II. With the use of CMR, the construction of reaction free energy diagrams and volcano-shaped plots was greatly facilitated.

Calculation of adsorption free energies

Input	A surface and a MOR intermediate species
Output	Adsorption free energy corresponding to the most stable site

The adsorption free energy is calculated using a formula of the form of Eqn. 3.12. First, the total energy of the clean surface is retrieved from the database. The calculation is retrieved with the use of a set of tags that uniquely describe the surface composition and structure, for example ("Pt", "fcc(111)"). A list of total energy calculations of the reaction species on all available adsorption site is retrieved. The list is sorted with respect to the energy and the lowest energy is used together with the total energy of the clean surface to calculate the adsorption energy. Corrections are applied to the calculated energy and the adsorption free energy is reported.

Construction of reaction free energy diagrams

Input	A surface and a MOR path
Output	Reaction free energy diagram, overpotential estimation and PDS

For all the pathways of the given MOR path (direct or indirect, Fig. 1.2), the adsorption free energy of each of the corresponding reaction intermediates is calculated as described above. The reaction free energy diagram is constructed. The MOR overpotential is estimated and the PDS is identified.

Construction of volcano-shaped plots

Input	A set of surfaces and a MOR path
Output	A volcano plot

A list of calculations is compiled corresponding to either flat or stepped or both surfaces. The adsorption free energy is calculated for every reaction intermediate on every surface. With the calculated energies at hand, linear relationships are built. The reaction free energy diagram is constructed as described above and the MOR potential is calculated. This way, a volcano plot is built for the given MOR path.

5. The search for efficient fuel cell catalysts

Chapters 3 and 4 describe a DFT-based methodology for the evaluation of electro-catalytic performance. The process starts from an atomistic description of the catalytic material and passes through multiple layers of theoretical and computational modeling.

This chapter offers a look at the main findings of the included Papers from multiple perspectives. Insight-driven approaches based on the use of reactivity descriptors and scaling relationships open up the possibility of screening studies for novel, efficient FC catalysts. With use of volcano-shaped plots, the calculation of only a small set of adsorption free energies suffices for the evaluation of catalytic activity. In the same time, optimal values of the reactivity descriptors are identified. Insights into the catalytic systems studied are introduced in the form of design rules which guide the search for novel catalytic materials. Promising electro-catalysts are identified and studied in detail.

The questions posed in the Overview are repeated below:

1. What are the electro-catalytic properties of a material of specified composition and physical structure?
2. What is the composition and physical structure of an electro-catalyst exhibiting a set of desired (or optimal) properties?

Two case studies from Paper I and II are presented first. Functionality is predicted from structure (blue arrow in Fig. 5.1). A discussion on the search for FC cathode (Paper I) and anode (Paper II) catalysts of enhanced performance follows. In the process, the path from functionality towards structure is followed (red arrow in Fig. 5.1). Paper III is discussed mainly in the context of reducing catalyst cost.

Case studies

In Paper I, the search for improved FC cathode catalysts starts from the evaluation of ruthenium selenium (RuSe) surface alloys and a set of other chalcogen-modified Ru surfaces. Paper II ends with the detailed study of platinum copper (PtCu) surfaces. Both of the RuSe and PtCu alloys are identified as promising electro-catalysts for the FC cathode and anode reaction, respectively.

Studying electro-catalytic functionality by performing a full set of electronic structure calculations serves multiple purposes:

- it evaluates catalytic performance at a level of accuracy sufficient for semi-qualitative comparison with experimental results
- it is used for testing the employed models by comparison of the findings with experiment
- it allows for trends in catalytic functionality to be identified from a set of individual studies of catalysts

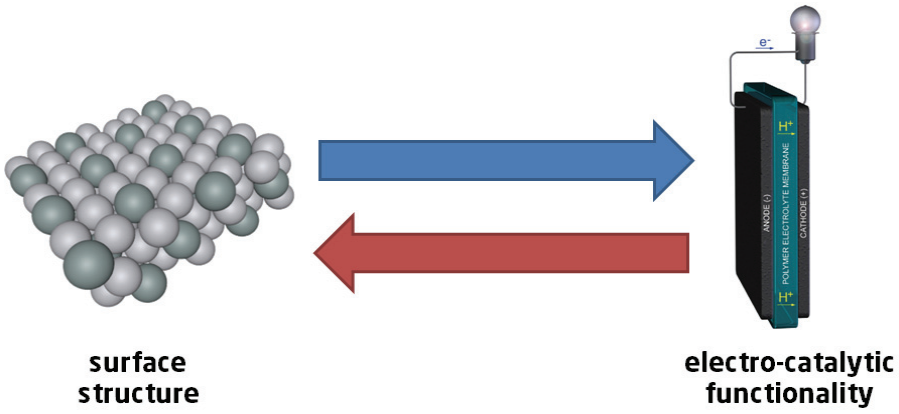

Fig. 5.1 The link between surface structure and electro-catalytic functionality.

Oxygen reduction on ruthenium chalcogenides

Pt fcc(111) served as the natural starting point for the study of the ORR on close-packed TM surfaces. In a similar fashion, in Paper I, RuSe is a natural starting point for the study of the electro-chemical ORR on Ru and other TM chalcogenides. RuSe is a well-studied ORR electro-catalyst [174-177]. The work of Alonso-Vante et al. [174] has demonstrated that RuSe catalysts show enhanced activity compared to Ru and that are not susceptible to methanol cross-over effects. A brief summary of the computational study of Ru chalcogenide catalysts follows.

Model close-packed surfaces were constructed as Ru hcp(0001) slabs where Ru atoms in the top layer were substituted with selenium (Se) or sulfur (S) atoms. The surfaces were modeled on the grounds of experimental observations for RuSe, which suggest a Ru hcp surface rich in Se [178]. Se and S-modified Ru surface alloys of varying content in the chalcogen were modeled (Fig. 1 in Paper I). For all surfaces, the ORR potentials are calculated as a measure of catalytic activity.

Ru surfaces with moderate content in Se ($Ru_{0.50}Se_{0.50}$, i.e. ½ surface coverage) are verified to show higher activity than Ru (Table 2 in Paper I). Surfaces with high chalcogen content ($Ru_{0.25}Se_{0.75}$, i.e. ¾ surface coverage) are found less active. Se-modified surfaces are calculated more active than S-modified surfaces. The following order is established for the activity: $Ru_{0.50}Se_{0.50} > Ru_{0.50}S_{0.50} > Ru > Ru_{0.25}Se_{0.75} > Ru_{0.25}S_{0.75}$. The respective ORR potentials are calculated 0.37 > 0.21 > 0.14 > 0.13 > -0.13V. The observed trends are in accordance with experiments [174,175]. For a Pt fcc(111) surface, U_{ORR} = 0.80V (Table 2 in Paper I). None of TM chalcogenides studied in Paper I was found to outperform Pt in terms of activity.

Stability is discussed in terms of segregation and phase separation effects. For all the Ru selenides diffusion of Se from the top layer to the bulk is associated with a high energy barrier. The barriers are calculated by interchanging Ru atoms of the second layer with Se atoms of the top layer. For $Ru_{0.25}Se_{0.75}$, $Ru_{0.50}Se_{0.50}$ and $Ru_{0.75}Se_{0.25}$ the barriers are calculated 1.44, 2.21 and 2.35eV (Table 1 in Paper I). The surface alloy mixing energy is calculated with an elemental Ru

slab and a Ru slab covered with a monoatomic skin of Se as reference. Phase separation is found energetically unfavorable (Table 1 in Paper I).

The evaluation of the selectivity of the Ru chalcogenides in the presence of methanol follows. The energy barrier U_{MO} for methanol activation is calculated. On Pt fcc(111), methanol oxidation is found to proceed through a CH_2OH intermediate (Table S3 in Paper I Sup. Inf., see also Paper II). The barrier is calculated equal to 0.43eV. For $U = U_{ORR}$, the barrier U_{MO} shifts down to -0.37eV. The negative energy difference implies that methanol readily decomposes on the Pt surface. In contrast, dehydrogenation of methanol is found thermodynamically unfavorable on all the Ru chalcogenides, in accordance with experiments [174](Fig. 3 in Paper I).

RuSe is verified to show enhanced electro-catalytic performance compared to elemental Ru and the other Ru chalcogenides studied. Experimentally observed trends are reproduced. For a more extended discussion, see Paper I.

Methanol oxidation on platinum copper alloys

In Paper II, alloys of PtCu are suggested by a screening procedure as promising electro-catalysts for the MOR. The screening initially predicts the MOR potential with limited accuracy. DFT calculations of model PtCu surfaces are performed for a better estimation of the overpotential. A brief summary of the computational study of PtCu catalysts follows.

Model structures were constructed for studying the PtCu surfaces. Model L_{12}(211) surfaces of Cu_3Pt and Pt_3Cu alloys were used, as well as a Pt fcc(211) surface, where the step atoms were substituted with Cu, Pt_2Cu/Pt (Fig. 4c-e in Paper II). The reactivity descriptors established for the MOR, i.e. the adsorption free of OH and CO, are calculated (Table S2 in Paper II Sup. Inf.) and the surfaces are positioned on a previously constructed volcano plot for the MOR potential (more on the the construction of the volcano plot follows shortly). An efficient anode catalyst for DMFC simultaneously satisfies the following three conditions [27]:

a. is active towards forming CO from methanol
b. easily activates water
c. binds both CO and OH moderately so CO_2 can form

The calculated descriptors suggest that both the PtCu alloys surfaces oxidize methanol to CO as efficiently as they oxidize CO to CO_2 (Fig. 5 in Paper II). None of the elemental surfaces studied fits the description of an efficient MOR catalyst. For example, Pt readily oxidizes methanol to CO but has difficulty activating water [27]. By comparison, the PtCu are found to show enhanced catalysis.

The stability of the bimetallic surfaces is evaluated in terms of their susceptibility to atomic diffusion effects. The energy barrier associated with atomic diffusion is calculated by swapping Pt atoms with nearest neighbor Cu atoms (Fig. S1 and Fig. S2 in Paper II Sup. Inf.) Such processes are calculated energetically unfavorable for both surfaces. All energy barriers are found positive. For Pt_3Cu/Pt, CO adsorption-induced segregation is found to be potentially an issue [119]. No further calculations of this model surface were performed.

A full set of DFT calculations were performed for the evaluation of the Cu_3Pt alloy. The PDS is determined to be the oxidation of CO to CO_2 (Fig. S3 in Paper II) with an associated energy barrier $U^i_{MOR} = U_{CO_2} = -(\Delta G_{OH} + \Delta G_{CO}) = 0.51$V (Table 2 in Paper II). In contrast, the MOR potential for Pt is calculated almost double, with $U^i_{MOR} = 0.90$V and 1.00V for the fcc(111) and fcc(211) surfaces

(Table 1 in Paper II). For Cu_3Pt, the potential U_{CO_2} is calculated almost equal to the potential U_{CO} that is associated with the oxidation of methanol to CO, with $U_{CO} = 0.47V$ (Table 2 in Paper II). In other words, the bimetallic alloy is found to satisfy simultaneously two of the three conditions for an efficient MOR electro-catalyst.

De-alloyed PtCu nanoparticles have been identified by experimental means to be active as PEMFC cathode catalysts [179,180]. Dissolution of Cu from the surface at low potentials could affect any of the aspects of catalytic performance. The lattice constant of Cu_3Pt is ca. 5% smaller compared to elemental Pt (Table S6 in Paper II Sup. Inf.) The surface of the de-alloyed PtCu nanoparticles shows a substantial number of irregularities (Fig. 5.2). Stepped surfaces are used as a model for defects. Compressing the lattice of a Pt fcc(211) so it matches that of Cu_3Pt, destabilizes the reaction intermediates on it, as the d-band model suggests. For, Pt fcc(211), the descriptors are calculated $(\Delta G_{OH}, \Delta G_{CO}) = (-1.16eV, 0.27eV)$. The minimum of the volcano plot corresponds to weaker binding of the descriptors, $(\Delta G_{OH}, \Delta G_{CO}) = (-0.29eV, 0.01eV)$. Thus, upon compression, the Pt fcc(211) will shift towards lower MOR overpotentials. Even if a de-alloyed surface is the case, enhancement in performance in comparison to elemental Pt is predicted. Consequently, the findings support the experimental observation that PtCu catalysts can also be susceptible to methanol cross-over effects as much as Pt is [179]. The exact ratio between the MOR and ORR activities will in general be dependent on the specifics of the nanoparticle's microstructure [181]. The model constructed in Paper III could be employed here for a study of catalytic selectivity.

Summarizing, PtCu alloys are predicted to show lower MOR overpotential compared to elemental Pt. They are suggested as promising DMFC anode catalysts. For a more extended discussion, see Paper II.

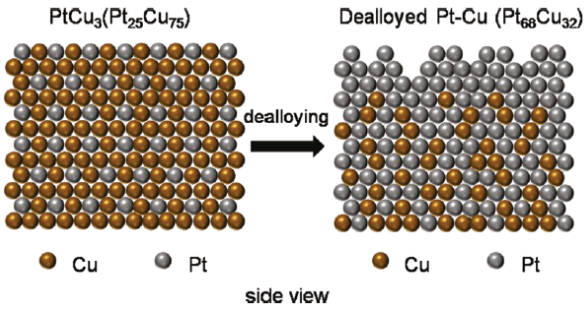

Fig. 5.2 Schematic of a de-alloyed Cu_3Pt film [182].

Transition metal-based electro-catalysts

The descriptors approach

Searching for FC catalysts of enhanced performance implies that more active, selective and stable catalysts exist than the known ones, waiting to be discovered. In principle, electro-catalytic performance can be estimated for all the candidate catalytic materials in the search space. In the process, the optimal catalyst for the given reaction is identified. On the other hand, predicting the functionality of even a single catalyst from first principles as described in Chapter 3 can be a computationally intensive procedure. Even if a small number of calculations need to be performed

(corresponding to three as in the case of the ORR) or only small unit cells are treated, the search space can be enormous. [183] In that case, an exhaustive search is impractical.

An intermediate layer of fast to calculate descriptors is introduced between surface structure and electro-catalytic functionality (Fig. 5.3). In this thesis, adsorption energies of reaction intermediates assume the role of such descriptors. The continuity of the path in the direction from structure towards functionality is kept intact:

1. DFT-based methods and models for the calculation of the reactivity descriptors (i.e. adsorption energies) have been presented in Chapter 3.
2. Reaction free energy diagrams are constructed from linear relationships among the adsorption energies of the reaction intermediates.

With the use of reactivity descriptors and linear relationships, volcano-shaped plots are constructed. The volcano plots serve as a *bidirectional* link between the descriptors and electro-catalytic functionality: there is a one-to-one relationship between the values of a set of descriptors and the activity (or overpotential).

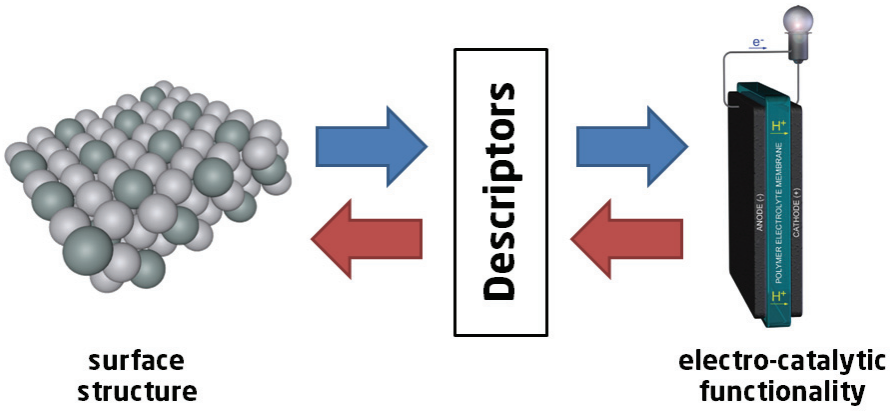

Fig. 5.3 The descriptors approach.

Catalysts for the methanol oxidation

Paper II demonstrates an approach for exploring the path in the direction from electro-catalytic functionality towards surface structure. It is one example of materials discovery by insight-based computational screening methods. A brief summary of the screening study follows.

Low-index flat and stepped surfaces of a set of 11 TMs were modeled as extended slabs. The potentials relevant to both of the direct and indirect paths of the MOR are calculated (Fig. 1 in Paper II). For all the surfaces, the potential for the indirect path is calculated less or equal than the potential for direct path. For example, for a Pt fcc(111) surface the potentials are calculated U^{i}_{MOR} = 1.00V and U^{d}_{MOR} = 0.41V (Table 1 in Paper II). CO binds strongly to the surface [34](Table S1 in Paper II Sup. Inf.) Since the direct mechanism will mostly contribute to the anode's current only after the removal of the poisoning CO, the potential U^{i}_{MOR} is used as estimation for the reaction overpotential.

Two sets of linear relationships are established, one for the O-bound MOR intermediates and one for the C-bound species (Fig. 3 in Paper II). A volcano-shaped plot for the MOR potential is constructed (Fig. 2 in Paper II) with the use of two reactivity descriptors, ΔG_{OH} and ΔG_{CO}. Is there a TM-based electro-catalyst that could lie at the top of the MOR potential volcano? In other words,

what is the structure of a surface that binds the MOR optimally? Designing a bimetallic alloy catalyst introduces increased flexibility in tuning the reactivity descriptors towards enhanced (or optimal) performance. This is possible because the descriptors can vary independently. In the same time, the search space is expanded. A screening mechanism is employed to reduce the number of candidate structures.

A *bi-functionality model* is developed for predicting the overpotential of a bimetallic catalyst. The model uses as input the calculated minimum potentials, at which each of the MOR channels operates (i.e. methanol activation U_{CO}, water activation U_{OH} and CO oxidation U_{CO_2}), for two different surfaces (Table S4 in Paper II Sup. Inf.) Then, it gives a prediction for the MOR potential for the alloy as

$$U^{i}_{MOR} = \min\left(\max\left(U^{A}_{CO}, U^{B}_{OH}, U^{min}_{CO_2}\right), \max\left(U^{B}_{CO}, U^{A}_{OH}, U^{min}_{CO_2}\right)\right) \quad (5.1)$$

where

$$eU^{min}_{CO_2} = \min\left(-\Delta G^{A}_{OH}, -\Delta G^{B}_{OH}\right) + \min\left(-\Delta G^{A}_{CO}, -\Delta G^{B}_{CO}\right) \quad (5.2)$$

The superscripts "A" and "B" denote the surface on which each potential pr adsorption free energy is calculated. Both of the OH and CO are assumed adequately mobile on the surface [44]. For example, Pt has difficulty activating water. Ru, on the other hand, activates water although it binds OH so strongly that its removal becomes difficult. A bi-functional PtRu alloy brings together the best of two worlds [27]. For a Pt flat surface and a Ru step, (U_{CO}, U_{OH}, ΔG_{OH}, ΔG_{CO}) = (0.33V, 1.00V, 1.00eV, 0.86eV) and (0.22V, -0.49V, -0.49eV, -0.97eV), respectively (Tables S1 and S4 in Paper II Sup. Inf.) The potential for the alloy is predicted by the model equal to 0.33V. The PDS is identified to be the initial dehydrogenation of methanol on Pt. The findings are in agreement with experiments [16,46].

All possible combinations of the elemental surfaces, are screened for low MOR potential. The top 20 alloys are reported (Fig. 6 in Paper II). The first five are found to be Ir_sCu_s, Pt_sCu_s, Ru_sCu_s, Cu_sCo_t, Pt_tRu_s. The subscripts "s" and "t" denote a stepped and flat surface (terrace), respectively. Two general remarks follow:

1. Surface irregularities give rise to bi-functionality [184]. 15 of the top 20 alloys screened include steps, a supportive argument for the importance of considering steps (which also serve as a model for defects) in an attempt for modeling MOR catalysts. The MOR potential for Pt_sPt_t is predicted ca. 0.30V, which is lower compared to that of Pt fcc(211), 0.90V, or Pt fcc(211), 1.00V. This result comes to complement the observation in Housmans et al. [184] of a favorable "ensemble site" of a step and a terrace for methanol decomposition.
2. Pt is a component in all the top alloys that successfully fulfill an additional set of criteria related to surface stability (see "Evaluating stability" in Chapter 3). All non-noble catalysts (e.g. Cu_sCo_t) are flagged as possibly unstable.

For an extended discussion of the results of the screening procedure, see Paper II.

The screening procedure points at the nature of the active site for the MOR but not at specific surface structure. For example, an alloy of a terrace and a step could correspond to the situation of clusters of one metal supported by the terrace of a second metal or a crystallographic defect on a flat surface (see also Paper III). Three different crystal structures (Fig. 4c-e in Paper II) were used to construct 10 model surfaces in total for the two bi-functional alloys suggested by the screening

as promising catalysts. The modeling of the catalysts is guided by intuition: since both combinations include only stepped surfaces, stepped bimetallic surfaces are used to model the alloys (Fig. 4c-e). The reactivity descriptors were calculated for all surfaces. The MOR potential for the IrCu alloys is found 0.90-1.70V more than the prediction of the screening. Thus, only PtCu alloys are examined in more detail, as discussed earlier in this chapter.

Instead of treating the problem of predicting surface structure from descriptors values directly, an exhaustive search identifies catalytic surfaces that are described by optimal descriptors values. This way, a structure-descriptors link is established. Together with a descriptors-functionality link in the form of the volcano plots, they allow for the path from surface structure to electro-catalytic functionality to be traced in both directions (Fig. 5.4).

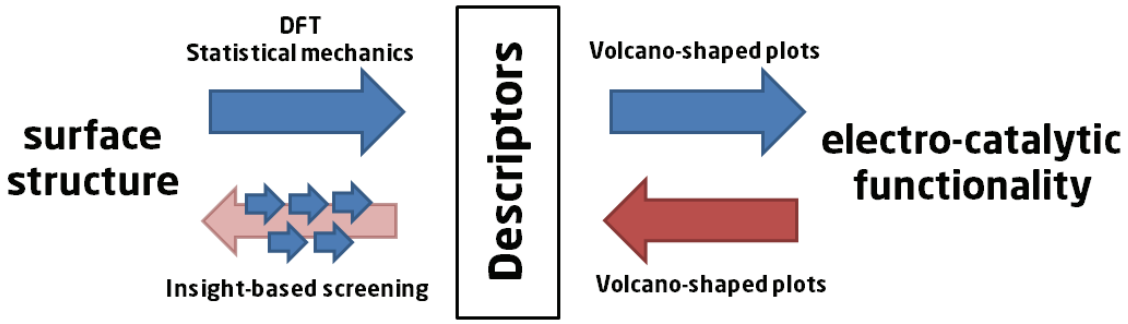

Fig. 5.4 An insight-based approach to catalyst design.

Catalysts for the oxygen reduction

Paper I discusses how the inclusion of chalcogen atoms in TM metals surfaces affects electro-catalytic functionality. A brief summary of the study of Paper I follows.

The Ru chalcogenides have already been discussed. More TM chalcogenides are considered at that point. Catalytic surfaces of Rh, Ir, Co, Pd and W modified with Se and S of ½ and ¾ coverage were modeled in a similar fashion as the Ru chalcogenides.

The surface stability is evaluated in a similar fashion with the Ru chalcogenides. Both Se and S are found to segregate to the top layer in all cases (Table 3 in Paper I). Two observations are made here:

1. The mixing energy in all cases is negative (or slightly positive in the case of $Ir_{0.25}Se_{0.75}$) suggesting that a surface ordered alloy is thermodynamically favorable (Fig. 4 in Paper I).
2. The absolute mixing energy is maximized for moderate content in Se (½ coverage), an effect ascribed to surface in-plane relaxation effects.

Scaling relationships for the adsorption energies of the ORR intermediates are established (Fig. 5 in Paper I). The chalcogen-modified surfaces are found to share the same linear relationships with the corresponding elemental surfaces. A common activity volcano plot is constructed (Fig. 6 in Paper I) with use of the adsorption energy of OH as reactivity descriptor.

Modifying a TM surface with Se or S affects the binding of the reaction intermediates to the surface. For example, a 1/4ML of OH binds to a clean surface of $Ru_{0.50}Se_{0.50}$ (the most active Ru chalcogenide identified) less strongly by 0.48eV compared to $Ru_{0.25}S_{0.75}$ (the least active Ru chalcogenide) (Table S2 in Paper II Sup. Inf.) In general, whether the effect on activity is positive or negative compared to the respective unmodified surface, depends on where the latter rests on the activity volcano plot. For example, for $Co_{0.50}Se_{0.50}$, the ORR potential is calculated 0.33V, which

is almost double the potential of elemental Co, 0.14V (Table 2 and Fig. 6 in Paper I). On the contrary, modification of a Pd surface results in lower activity, since elemental Pd sits already close to the top of the volcano, with U_{ORR} = 0.76 (Table 2 in Paper I).

The activities of Rh chalcogenides show a similar trend compared to Ru chalcogenides (Fig. 6 in Paper I). Se-modified surfaces are more active than the S-modified surfaces, in agreement with experiments [175]. The $Rh_{0.50}Se_{0.50}$ surface is calculated to show the highest activity among the TM chalcogenides studied, with U_{ORR} = 0.79 (Table 2 in Paper I). The activity is calculated comparable to elemental Pt and higher than that of any of the Ru chalcogenides. However, it has been reported that chalcogen-modified Rh surfaces are less active than the Rh chalcogenides [185]. The discrepancy may arise from the fact that the model does not account for the numerous possible surface phases. In any case, the calculated ORR potentials are an estimation of the upper limit of the activity, which does not conflict with the aforementioned experimental observations.

Tolerance to methanol oxidation is evaluated as previously demonstrated for the RuSe surface. Looking at trends, the TM chalcogenides show increased tolerance compared to elemental surfaces (Fig. 3 in Paper I). For example, the barrier U_{MO} for $Co_{0.50}Se_{0.50}$ is calculated 0.26eV higher than this of elemental Co (Table S3 in Paper I Sup. Inf.) The Rh chalcogenides are found to be less tolerant to methanol oxidation than the Ru chalcogenides, in accordance with experiment [185].

With the use of descriptors and trends in surface reactivity, electro-catalytic performance was evaluated from surface structure for all the catalysts in the study set. Effectively, this exhaustive search maps electro-catalytic functionality to surface structure for all the catalysts in the search space.

The study set is expanded to include TM surfaces modified with the As and P elements. The alloys are shown to be in the same class of electro-catalysts with the elemental and chalcogen-modified surfaces (Fig. 7 in Paper I).

Paper I focuses on the study of relative trends between elemental and modified TM surfaces. Only a few catalysts are evaluated with a full set of DFT calculations, as for example RuSe, which serves as a representative case study and a link with experiment.

Reducing catalyst cost

In Paper III, the search for efficient and inexpensive catalysts coincides with the optimization of the geometry of the catalytic nanoparticles [11,35]. A brief summary of the study follows.

For Pt catalysts, the existence of a maximum in ORR mass activity versus particle size is now well established [186,187]. Pt nanoparticles of were modeled as described in Section 3 (Fig. 3.1). For edge atom, two step sites were considered. Model particles of a diameter in the range of 2 to 30nm were constructed. The activity was averaged over all the different active sites (Fig. S1 in Paper III Sup. Inf.) The ORR potentials for the extended surfaces (100), (111) and (211) were used for calculating the activity, 0.80, 0.78 and 0.17V, respectively [58](Table S1 in Paper III Sup. Inf.)

The ORR activities on the extended surfaces are used on the assumption that the effect of the steps on the activity of the neighboring sites (and vice versa) is negligible. The adsorption free energies of two ORR intermediates, O and OH, are calculated. Extended Pt fcc(544) model surfaces are used (Fig. S2 in Paper III Sup. Inf.) The steps are shown to become occupied first. O and OH bind to the step site more strongly by 0.43eV and 0.85eV, respectively, than to the next

atomic row (Table S2 in Paper III Sup. Inf.) The effect of a step with 50% coverage of O or OH on the adsorption free energy of the same adsorbate bound to the next atomic row, is calculated +0.09 and -0.11, respectively (Table S2 in Paper II Sup. Inf.) The effect of the step is shown not to extend further than one neighboring row of atoms (Fig. 2 in Paper III). At potentials relevant for the ORR (ca. 0.9V), the ORR intermediates reside embedded in a half-dissociated water layer (Fig. 3.2). Every two intermediate species are separated by water molecules. The next atomic row to be occupied by ORR intermediate species after the step is the second, on which the step has no effect.

The specific and mass activities of all the particles were calculated and compared to experiment. The model captures the experimentally observed trend in the specific activity [11](Fig. 3 in Paper III). The ratio between the activity of the biggest and smallest particles is calculated ca. 4, in agreement with experiment. The mass activity is shown to be maximized for particles of a diameter in the range of 2-4nm.

Greeley et al. [58] developed a similar model for nanoparticle catalysis. Only one step site for every edge atom dissolving was assumed instead of two. In this case, the ratio between the maximum and minimum specific activities is underestimated, calculated ca. 1.5 (Fig. 3 in Paper III). The maximum in mass activity is not observed. Paper III suggests that an accurate description of surface irregularities is needed for modeling nanoparticle catalysis.

A tenfold increase in specific activity for extended Pt fcc(111) surface has been reported [11]. The proposed model underestimates this ratio by a factor of 2. The utilization of catalysts comprising octahedra nanoparticles has been proposed as an alternative route to achieving increased activity [196]. For a model particle of octahedron shape with dissolved edges and corners and ~30nm in diameter, the mass activity is calculated to double.

The maximum in the ORR mass activity discussed in Paper III, corresponds to reduced catalyst cost. In Papers I and II, alloying of expensive TMs, such as Pt and Ru, with less expensive elements, such as Se and Cu, is a different strategy for reducing catalyst cost. The loading of the precious metal is reduced. Non-precious electro-catalysts have been explored in the literature [11,33]. In Paper II, the screening procedure flags all the non-precious candidate catalysts as possibly unstable in the electrochemical environment of the DMFC (Fig. 6 in Paper II). The screening assumes that the energetics of each metal to remain unaffected by the presence of the other. Stabilization of the surface through ligand effects is suggested to be a requisite, if the complete replacement of Pt is desired.

Tuning catalytic performance

Trends in the reactivity of the TM-based surfaces describe *change*. Scaling relationships describe change qualitatively. For example, the linear relationships established in Papers I and II, describe qualitatively how the surface reactivity (adsorption energies) changes when the composition of the surface changes (substituting one metal with another other).

Subjecting a TM surface to compressive or tensile strain affects its reactivity. [188,189,113] Tensile strain expands the lattice. Increased interatomic distances result in decreased overlap between the d-states. The d-band narrows. Assuming that no charge transfer takes place, a more than half-filled d-band (as in the case of late TMs) moves up in energy to keep the number of electrons fixed. The energy upshift of the d-band states results in higher lying antibonding states

upon interaction of the surface with an adsorbate (Fig. 2.5). Thus, the interaction becomes more attractive. In Paper II, the effect of compressive strain on the reactivity of Pt fcc(211) is discussed. Under compressive strain the d-band states move down in energy, the surface-adsorbate bonds weakens and the MOR potential is reduced. The position of the uncompressed Pt fcc(211) on the volcano plot of Fig. 2 in Paper II is known. Knowledge on how its reactivity is affected under strain allows for predicting the relative position of the compressed surface (used as a model for de-alloyed PtCu surfaces) on the volcano plot.

In Paper III a one-to-one relationship is established between the size (diameter) of the model nanoparticles and the ORR activity. Atoms in steps have a smaller number of neighbors in comparison to atoms in low Miller index surfaces. The extent of the overlap between the d-states depends on the number of nearest neighbors. Small coordination number corresponds to small overlap between the d-states and strong surface-adsorbate bonding. The average surface coordination number changes as the size of the catalytic nanoparticles changes. For example, for the model of Paper III, a cluster of a diameter of 3nm features equal number of (111) and step sites. Each represents ca. 30% of the total sites (Fig. S1 in Paper III Sup. Inf.) For nanoparticles of a diameter of 15nm, the ratio between (111) sites and step sites is ca. 6. The relatively high number of low-coordinated sites on small nanoparticles results in the poisoning of the surface by the strongly bound ORR intermediates. The specific ORR activity decreases with decreasing size. Effectively, change in the particle size is readily translated into change in catalytic performance. Shape-controlled synthesis of catalytic nanoparticles allows the ratio of low-coordinated surface sites over the well-ordered domains to be controlled [190,191]. With the input of computational modeling, surface structure is tuned towards enhanced catalytic activity (performance) in a rational way.

Such insight is introduced into the search for novel catalytic materials in the form of design rules. Starting from a catalyst of well understood structure and functionality, catalysis is tuned towards enhanced performance.

Fundamental limits of activity

In Paper I, the ORR on chalcogen-modified TM surfaces is assumed to proceed through the same mechanism as the corresponding elemental surfaces. Scaling relationships common to both the TM chalcogenides and elemental TMs are established (Fig. 5 in Paper I). In both cases, the adsorption energies of OH and OOH differ by ca. 3.2eV. Elemental and chalcogen-modified TM surfaces are found members of the same class of electro-catalysts for the ORR, susceptible to the same limits of activity. The lower limit of the ORR overpotential on both elemental and chalcogen-modified TM surfaces is estimated ca. 0.4V. This conclusion is also supported by the reported activities of the TM chalcogenide catalysts, which are found at best comparable to this of elemental Pt but not higher [175,192], Pt being the most active elemental TM catalyst, situated on the very top of the activity volcano (Fig. 6 in Paper I).

In Paper II, close-packed flat and stepped TM surfaces are shown to share common scaling relationships for the MOR intermediates. As a result, they are considered members of the same class of electro-catalysts for the MOR. The study of Abild-Pedersen et al. has demonstrated that scaling relationships are structure sensitive [193]. The models constructed in Paper II rely on the

assumption that structure sensitivity can be hidden in the deviation from the linear relationships as scattering. The mean square error for the slope of the linear relationship describing the correlation between OH and H_2COOH is calculated 4%. For CO and COH the error is calculated 8%. In comparison, the study of Ferrin et al. [127] uses two different sets of scaling relationships to describe trends in surface reactivity. One set for (111) surfaces and one for (100) surfaces. Accordingly, two separate volcano plots were constructed. Making this distinction is of secondary importance for discussing the existence itself of a universal minimum for the MOR overpotential. The minimum MOR potential is calculated 0.29V. The potential for most promising MOR electrocatalyst identified in Paper II, the PtCu alloy, is estimated even higher with $U^{i}_{MOR} = 0.51V$.

If a TM-based surface that defies the limiting nature of linear relationships can be designed and engineered is an open research topic. Highly efficient biological catalysts have provided inspiration for the design of improved inorganic catalytic materials [41,144,145]. In any case, even if a dream catalyst is beyond reach, there is still room at the top of the volcano plots [120].

Data-driven modeling

As soon as the process of generation and management of the data becomes faster than their analysis by scientific intuition, tools and methods that extract useful information from the data can push the limits to progress further [49,173,194].

In Paper II, the adsorption free energies of the MOR intermediates are shown to follow two separate sets of linear relationships. Different correlation exist among O-bound intermediates and C-bound intermediates. The bonding between the surface and the binding O or C atom of the adsorbates exhibits common features for each group of intermediates. Physical insight suggests the construction of two distinct sets of linear relationships.

Patterns may also be extracted from a data set by combining methods from statistics with a database [49]. Correlations between the adsorption free energies calculated in Paper II can be identified by statistical analysis of the established catalytic data set. Let D be the numerical matrix describing the data set with

$$D_{i,j} = \Delta G^{i}_{j} \tag{5.3}$$

where ΔG^{i}_{j} is the adsorption energy of the i-th adsorbate on the most stable binding site of the j-th surface of the data set. The data of Table S1 in Paper II Sup. Inf. are used to build the data matrix D. As a measure of strength of linear dependence, for every two adsorbates, corresponding to the i_1-th and i_2-th column of the data matrix D, the *Pearson product-moment correlation coefficient* r_{i_1,i_2} is calculated [195]

$$r_{i_1,i_2} = \frac{N\sum D_{i_1,j}D_{i_2,j} - \sum D_{i_1,j}\sum D_{i_2,j}}{\sqrt{N\sum D^{2}_{i_1,j} - \left(\sum D_{i_1,j}\right)^{2}}\sqrt{N\sum D^{2}_{i_2,j} - \left(\sum D_{i_2,j}\right)^{2}}} \tag{5.4}$$

where the sum runs over all the N surfaces in the data set (N = 22). The (symmetric) correlation matrix r is presented in Table 5.1.

In general, the correlation coefficients assume values in the range of [-1,1]. The closer the value to ±1, the closer to perfect the correlation is. Values close to 0 show little or no association. For example, the adsorption free energies of CHO and COOH (r = 0.96) are strongly correlated. A

weak correlation is calculated between CHOH and CH_3O (r = 0.52). All values in Table 5.1 are positive: strong (weak) adsorption of one reaction intermediate is associated with strong (weak) adsorption of the second.

Adsorbates are grouped together on the basis of the following clustering procedure:
Two adsorbates i_1 and i_2 are grouped together if $r_{i_1,i_2} \geq r_c$ where r_c describes the threshold value for the correlation to be described as strong. Should for a third adsorbate i_3, $r_{i_1,i_3} \geq r_c$ or $r_{i_2,i_3} \geq r_c$, all three adsorbates are considered members of the same group. The threshold value was set to $r_c = 0.90$.

By performing the cluster analysis, two distinct sets of adsorbates are identified. O-bound and C-bound species are grouped in separate clusters. An adsorbate from each group is chosen as a reactivity descriptor and it is natural to select one that is easy to calculate. With only two atoms, both OH and CO make together a suitable set of descriptors.

The ever-growing availability of computing power allows for the compilation of larger and larger data sets describing more and more complex catalytic processes. The above analysis offers a rudimentary example of a data-driven approach to computational catalysis.

	H_2COO	H_2COOH	CO	OH	CHOH	$C(OH)_2$	CHO	CHOO	COOH	COH	CH_2OH	CH_3O
H_2COO	1.00											
H_2COOH	0.98	1.00										
CO	0.58	0.59	1.00									
OH	0.95	0.99	0.53	1.00								
CHOH	0.53	0.55	0.98	0.49	1.00							
$C(OH)_2$	0.39	0.43	0.93	0.36	0.97	1.00						
CHO	0.56	0.58	0.96	0.52	0.98	0.94	1.00					
CHOO	0.95	0.98	0.61	0.96	0.57	0.48	0.61	1.00				
COOH	0.69	0.71	0.92	0.65	0.93	0.90	0.96	0.75	1.00			
COH	0.54	0.52	0.97	0.46	0.97	0.90	0.94	0.52	0.88	1.00		
CH_2OH	0.48	0.52	0.89	0.47	0.94	0.95	0.96	0.59	0.94	0.86	1.00	
CH_3O	0.96	0.99	0.57	1.00	0.52	0.39	0.55	0.96	0.68	0.51	0.48	1.00

Table 5.1 Correlation matrix for the catalytic data set of Paper II. The cluster analysis groups the MOR intermediates into two separate sets. Green color marks O-bound species and violet color C-bound species.

6. Summary and outlook

Density functional theory simulations and theoretical materials modeling are used to study the electrochemical oxygen reduction and methanol oxidation reactions occurring on low-temperature fuel cell electrodes. Electronic structure calculations of model electro-catalysts were used to evaluate electro-catalytic performance in terms of activity, selectivity and stability. Trends in surface reactivity were identified and suitable descriptors of it have been established. The accuracy of the computational methods employed allowed semi-qualitative comparison with experiment.

The electro-catalytic performance of chalcogen-modified transition metal surfaces for use as cathode catalysts for low-temperature fuel cells was evaluated. Transition metal surfaces both elemental and modified with chalcogen atoms were shown to belong to the same class of oxygen reduction reaction electro-catalysts. Both were found susceptible to the same upper limit of activity. The lowest value for the overpotential was estimated ca. 0.4V. The high potential needed for the dehydrogenation of methanol is suggested as the origin of the tolerance of chalcogenide surface alloys to methanol oxidation. Ruthenium selenium was verified to show enhanced performance compared to elemental Ru surfaces. A future study based on a more accurate description of the surface structure of the different chalcogenides may be necessary for understanding why the calculated relative trends in activity between Ruthenium and Rhodium selenides are not in accordance with experiments.

A theoretical design cycle was followed in the search for efficient anode catalysts for direct methanol fuel cells. The lowest value for the overpotential was estimated ca. 0.3V. An insight-based approach was presented for the identification of bi-functional alloys of enhanced performance. One may proceed with enlarging the study set to ternary and quaternary alloys. Platinum copper alloys were identified as promising electro-catalysts for the methanol oxidation reaction. Their selectivity towards oxygen reduction when used as cathode catalysts in the presence of methanol merits further investigation.

The need for a detailed description of low-coordinated surface sites for understanding particle size effects was demonstrated. A model for nanoparticle catalysis was developed, which captures the experimentally observed trends in both the specific and mass activities of the oxygen electro-reduction on platinum. For fuel cell voltages of practical interest for the oxygen reduction reaction, surface irregularities were shown to have only a local effect on the activity of adjacent active sites. The ratio between the activity of the biggest and smallest particles was calculated ca. 4, in agreement with experiment. The mass activity was verified to be maximized for particles of a diameter in the range of 2-4nm. More precise modeling of the particle's surface and careful

consideration of the activity factors are possible directions for extending the scope of the model to particles with diameter greater than 30nm. Increased mass activities were estimated for octahedra particles.

In the process, the path between surface structure and electro-catalytic functionality was traced in both directions. Is there a transition metal-based electro-catalyst with zero ORR or MOR overpotential? None of the classes of the electro-catalysts studied in this thesis escapes the limiting nature of the scaling relationships, point at a possible direction for future research.

By statistical analysis of a catalytic data set, correlations among the adsorption energies of methanol oxidation reaction intermediates were identified. As the availability of computational power increases, screening studies may become broader. A larger number of promising candidates may be selected for further evaluation. Extended sets of crystal structure and chemical composition may be considered. As soon as the process of generation and management of the data becomes faster than data analysis, tools and methods that can extract meaningful information from the data sets without the need of physical insight can push the limits to progress further.

Bibliography

[1] N. Lewis and D. Nocera, Proceedings of the National Academy of Sciences of the United States of America **103**, 15729-15735 (2006).

[2] M. Ni, D. Y. Leung, M. K. Leung, and K. Sumathy, Fuel Processing Technology **87**, 461-472 (2006).

[3] M. Dresselhaus and I. Thomas, Nature **414**, 332-337 (2001).

[4] J. O. Bockris (1975).

[5] G. Crabtree, M. Dresselhaus, and M. Buchanan, Physics Today **57**, 39-44 (2004).

[6] L. Carrette, K. A. Friedrich, and U. Stimming, ChemPhysChem **1**, 162-193 (2000).

[7] J. Larminie and A. Dicks, *Fuel Cell Systems Explained*, 2nd ed. (Wiley, 2003).

[8] D. Hart, in *Encyclopedia of Energy* (Elsevier, New York, 2004), pp. 231-239.

[9] W. R. Grove, Philosophical Magazine Series 3 **14**, 127 (1839).

[10] P. Ferreira, G. La O' , Y. Shao-Horn, D. Morgan, R. Makharia, S. Kocha, and H. Gasteiger, Journal of the Electrochemical Society **152**, (2005).

[11] H. Gasteiger, S. Kocha, B. Sompalli, and F. Wagner, Applied Catalysis B: Environmental **56**, 9-35 (2005).

[12] Z. Gu and P. B. Balbuena, The Journal of Physical Chemistry A **110**, 9783-9787 (2006).

[13] S. Knights, K. Colbow, J. St-Pierre, and D. Wilkinson, Journal of Power Sources **127**, 127-134 (2004).

[14] Y. Shao-Horn, W. Sheng, S. Chen, P. Ferreira, E. Holby, and D. Morgan, Topics in Catalysis **46**, 285-305 (2007).

[15] A. S. Aricò, S. Srinivasan, and V. Antonucci, Fuel Cells **1**, 133-161 (2001).

[16] S. Wasmus and A. Küver, Journal of Electroanalytical Chemistry **461**, 14-31 (1999).

[17] M. Eikerling, A. A. Kornyshev, A. M. Kuznetsov, J. Ulstrup, and S. Walbran, The Journal of Physical Chemistry B **105**, 3646-3662 (2001).

[18] A. Kundu, J. Jang, J. Gil, C. Jung, H. Lee, S. Kim, B. Ku, and Y. Oh, Journal of Power Sources **170**, 67-78 (2007).

[19] P. Atkins and J. D. Paula, *Physical Chemistry*, 8th ed. (W. H. Freeman, 2006).

[20] C. Sealy, Materials Today **11**, 65-68 (2008).

[21] R. Adzic, in *Electrocatalysis*, edited by J. Lipkowski and P. N. Ross (Wiley-VCH, 1998), p. 197.

[22] K. Kinoshita and E. Society, *Electrochemical Oxygen Technology* (Wiley-Interscience, 1992).

[23] B. Grgur, N. Markovic, and P. Ross, Can. J. Chem. **75**, 1465-1471 (1997).

[24] V. Tripković, E. Skúlason, S. Siahrostami, J. K. Nørskov, and J. Rossmeisl, Electrochimica Acta **55**, 7975-7981 (2010).

[25] N. A. Vante, W. Jaegermann, H. Tributsch, W. Hoenle, and K. Yvon, Journal of the American Chemical Society **109**, 3251-3257 (1987).

[26] M. Götz and H. Wendt, Electrochimica Acta **43**, 3637-3644 (1998).

[27] T. Iwasita, Electrochimica Acta **47**, 3663-3674 (2002).

[28] D. Cao, G. Lu, A. Wieckowski, S. A. Wasileski, and M. Neurock, The Journal of Physical Chemistry B **109**, 11622-11633 (2005).

[29] E. Herrero, W. Chrzanowski, and A. Wieckowski, The Journal of Physical Chemistry **99**, 10423-10424 (1995).

[30] Dicks, *Fuel Cells*.

[31] M. Eikerling and A. Kornyshev, Journal of Electroanalytical Chemistry **453**, 89-106 (1998).

[32] H. A. Gasteiger, S. S. Kocha, B. Sompalli, and F. T. Wagner, Applied Catalysis B: Environmental **56**, 9-35 (2005).

[33] H. Liu, C. Song, L. Zhang, J. Zhang, H. Wang, and D. P. Wilkinson, Journal of Power Sources **155**, 95-110 (2006).

[34] B. Hammer, O. Nielsen, and J. Nørskov, Catalysis Letters **46**, 31-35 (1997).

[35] H. A. Gasteiger and N. M. Marković, Science **324**, 48-49 (2009).

[36] J. Kua and W. Goddard III, Journal of the American Chemical Society **121**, 10928-10941 (1999).

[37] A. Lima, C. Coutanceau, J. Léger, and C. Lamy, Journal of Applied Electrochemistry **31**, 379-386 (2001).

[38] V. Stamenkovic, N. M. Markovic, and P. N. Ross, Journal of Electroanalytical Chemistry **500**, 44-51 (2001).

[39] V. Stamenkovic, B. S. Mun, K. J. Mayrhofer, P. N. Ross, N. M. Markovic, J. Rossmeisl, J. Greeley, and J. K. Nørskov, Angewandte Chemie International Edition **45**, 2897-2901 (2006).

[40] P. Strasser, Q. Fan, M. Devenney, W. Weinberg, P. Liu, and J. Nørskov, Journal of Physical Chemistry B **107**, 11013-11021 (2003).

[41] Y. Gorlin and T. F. Jaramillo, Journal of the American Chemical Society **132**, 13612-13614 (2010).

[42] L. Zhang, J. Zhang, D. P. Wilkinson, and H. Wang, Journal of Power Sources **156**, 171-182 (2006).

[43] N. Lebedeva, M. Koper, J. Feliu, and R. Van Santen, Journal of Physical Chemistry B **106**, 12938-12947 (2002).

[44] S. W. Lee, S. Chen, W. Sheng, N. Yabuuchi, Y. Kim, T. Mitani, E. Vescovo, and Y. Shao-Horn, Journal of the American Chemical Society **131**, 15669-15677 (2009).

[45] J. Solla-Gullón, F. Vidal-Iglesias, A. López-Cudero, E. Garnier, J. Feliu, and A. Aldaz, Physical Chemistry Chemical Physics **10**, 3689-3698 (2008).

[46] H. A. Gasteiger, N. Markovic, P. N. Ross, and E. J. Cairns, The Journal of Physical Chemistry **97**, 12020-12029 (1993).

[47] W. Zhou, Z. Zhou, S. Song, W. Li, G. Sun, P. Tsiakaras, and Q. Xin, Applied Catalysis B: Environmental **46**, 273-285 (2003).

[48] J. Hafner, C. Wolverton, and G. Ceder, MRS Bulletin **31**, 659-668 (2006).

[49] W. Maier, K. Stowe, and S. Sieg, Angewandte Chemie - International Edition **46**, 6016-6067 (2007).

[50] J. K. Nørskov, T. Bligaard, J. Rossmeisl, and C. H. Christensen, Nat Chem **1**, 37-46 (2009).

[51] D. Frenkel and B. S. Professor, *Understanding Molecular Simulation: From Algorithms to Applications*, 2nd ed. (Academic Press, 2001).

[52] J. Kohanoff, *Electronic Structure Calculations for Solids and Molecules: Theory and Computational Methods* (Cambridge University Press, 2006).

[53] R. M. Martin, *Electronic Structure: Basic Theory and Practical Methods* (Cambridge University Press, 2004).

[54] G. Bond, *Catalysis by Metals* (Academic Press Inc, 1962).

[55] C. J. Jacobsen, S. Dahl, A. Boisen, B. S. Clausen, H. Topsøe, A. Logadottir, and J. K. Nørskov, Journal of Catalysis **205**, 382-387 (2002).

[56] M. P. Allen and D. J. Tildesley, *Computer Simulation of Liquids* (Oxford University Press, USA, 1989).

[57] W. Kohn, Rev. Mod. Phys. **71**, 1253 (1999).

[58] J. Greeley, J. Rossmeisl, A. Hellman, and J. Nørskov, Zeitschrift Fur Physikalische Chemie **221**, 1209-1220 (2007).

[59] A. Michaelides and P. Hu, Journal of the American Chemical Society **123**, 4235-4242 (2001).

[60] J. K. Nørskov, J. Rossmeisl, A. Logadottir, L. Lindqvist, J. R. Kitchin, T. Bligaard, and H. Jónsson, The Journal of Physical Chemistry B **108**, 17886-17892 (2004).

[61] Z. Shi, J. Zhang, Z. Liu, H. Wang, and D. Wilkinson, Electrochimica Acta **51**, 1905-1916 (2006).

[62] S. K. Desai, M. Neurock, and K. Kourtakis, The Journal of Physical Chemistry B **106**, 2559-2568 (2002).

[63] P. Ferrin, A. U. Nilekar, J. Greeley, M. Mavrikakis, and J. Rossmeisl, Surface Science **602**, 3424-3431 (2008).

[64] C. Hartnig and E. Spohr, Chemical Physics **319**, 185-191 (2005).

[65] E. Skúlason, G. S. Karlberg, J. Rossmeisl, T. Bligaard, J. Greeley, H. Jonsson, and J. K. Nørskov, Phys. Chem. Chem. Phys. **9**, 3241-3250 (2007).

[66] R. G. Parr and Y. Weitao, *Density-Functional Theory of Atoms and Molecules* (Oxford University Press, USA, 1994).

[67] M. Born and R. Oppenheimer, Annalen Der Physik **389**, 457-484 (1927).

[68] L. H. Thomas, Mathematical Proceedings of the Cambridge Philosophical Society **23**, 542-548 (1927).

[69] E. Fermi, Rend. Accad. Naz. Lincei (1927).

[70] P. Hohenberg and W. Kohn, Phys. Rev. **136**, B864 (1964).

[71] W. Kohn and L. J. Sham, Phys. Rev. **140**, A1133 (1965).

[72] N. Schuch and F. Verstraete, Nature Physics **5**, 732-735 (2009).

[73] S. Kurth, J. Perdew, and P. Blaha, International Journal of Quantum Chemistry **75**, 889-909 (1999).

[74] J. Chem. Phys. **123**, 062201-062201-9 (2005).

[75] A. D. Becke, J. Chem. Phys. **98**, 1372 (1993).

[76] D. M. Ceperley and B. J. Alder, Phys. Rev. Lett. **45**, 566 (1980).

[77] J. P. Perdew, J. A. Chevary, S. H. Vosko, K. A. Jackson, M. R. Pederson, D. J. Singh, and C. Fiolhais, Phys. Rev. B **46**, 6671 (1992).

[78] J. Tao, J. P. Perdew, V. N. Staroverov, and G. E. Scuseria, Phys. Rev. Lett **91**, 146401 (2003).

[79] J. P. Perdew, M. Ernzerhof, and K. Burke, J. Chem. Phys. **105**, 9982 (1996).

[80] B. Hammer, L. B. Hansen, and J. K. Nørskov, Phys. Rev. B **59**, 7413 (1999).

[81] J. P. Perdew, K. Burke, and M. Ernzerhof, Phys. Rev. Lett. **77**, 3865 (1996).

[82] A. J. Cohen, P. Mori-Sánchez, and W. Yang, Science **321**, 792-794 (2008).

[83] A. Ruzsinszky, J. P. Perdew, G. I. Csonka, O. A. Vydrov, and G. E. Scuseria, J. Chem. Phys. **126**, 104102 (2007).

[84] Y. Zhang and W. Yang, J. Chem. Phys. **109**, 2604 (1998).

[85] P. E. Blöchl, Phys. Rev. B **50**, 17953 (1994).

[86] J. J. Mortensen, L. B. Hansen, and K. W. Jacobsen, Phys. Rev. B **71**, 035109 (2005).

[87] J. Enkovaara, C. Rostgaard, J. Mortensen, J. Chen, M. Dułak, L. Ferrighi, J. Gavnholt, C. Glinsvad, V. Haikola, H. Hansen, H. Kristoffersen, M. Kuisma, A. Larsen, L. Lehtovaara, M. Ljungberg, O. Lopez-Acevedo, P. Moses, J. Ojanen, T. Olsen, V. Petzold, N. Romero, J. Stausholm-Møller, M. Strange, G. Tritsaris, M. Vanin, M. Walter, B. Hammer, H. Häkkinen, G. Madsen, R. Nieminen, J. Nørskov, M. Puska, T. Rantala, J. Schiøtz, K. Thygesen, and K. Jacobsen, Journal of Physics Condensed Matter **22**, (2010).

[88] A. H. Larsen, M. Vanin, J. J. Mortensen, K. S. Thygesen, and K. W. Jacobsen, Phys. Rev. B **80**, 195112 (2009).

[89] N. Troullier and J. L. Martins, Phys. Rev. B **43**, 1993 (1991).

[90] D. Vanderbilt, Phys. Rev. B **41**, 7892 (1990).

[91] D. R. Hamann, M. Schlüter, and C. Chiang, Phys. Rev. Lett. **43**, 1494 (1979).

[92] M. Cohen and P. S. Kelly, (1966).

[93] T. L. Beck, Rev. Mod. Phys. **72**, 1041 (2000).

[94] T. Frederiksen, M. Paulsson, M. Brandbyge, and A. Jauho, Phys. Rev. B **75**, 205413 (2007).

[95] W. L. Briggs, V. E. Henson, and S. F. McCormick, *A Multigrid Tutorial*, 2nd ed. (SIAM: Society for Industrial and Applied Mathematics, 2000).

[96] J. R. Chelikowsky, N. Troullier, K. Wu, and Y. Saad, Phys. Rev. B **50**, 11355 (1994).

[97] E. L. Briggs, D. J. Sullivan, and J. Bernholc, Phys. Rev. B **54**, 14362 (1996).

[98] H. J. Monkhorst and J. D. Pack, Phys. Rev. B **13**, 5188 (1976).

[99] M. J. Gillan, Journal of Physics Condensed Matter **1**, 689-711 (1989).

[100] D. M. Wood and A. Zunger, Journal of Physics A Mathematical General **18**, 1343-1359 (1985).

[101] M. C. Payne, M. P. Teter, D. C. Allan, T. A. Arias, and J. D. Joannopoulos, Rev. Mod. Phys. **64**,

1045 (1992).
[102] E. R. Davidson, Journal of Computational Physics **17**, 87-+ (1975).
[103] H. Hellmann, Einfuhrung in Die Quantenchemie 285 (1937).
[104] R. P. Feynman, Phys. Rev. **56**, 340 (1939).
[105] J. Nocedal and S. Wright, *Numerical Optimization* (Springer, 2000).
[106] P. W. Anderson, Phys. Rev. **124**, 41 (1961).
[107] D. M. Newns, Phys. Rev. **178**, 1123 (1969).
[108] B. Hammer and J. Nørskov, in *Impact of Surface Science on Catalysis* (Academic Press, 2000), pp. 71-129.
[109] E. Golfetto, A. Baraldi, M. Pozzo, D. Alfè, A. Sala, P. Lacovig, E. Vesselli, S. Lizzit, G. Comelli, and R. Rosei, The Journal of Physical Chemistry C **114**, 436-441 (2010).
[110] J. Greeley and M. Mavrikakis, Nature Materials **3**, 810-815 (2004).
[111] J. Greeley, J. K. Nørskov, and M. Mavrikakis, Annu. Rev. Phys. Chem. **53**, 319-348 (2002).
[112] B. Hammer and J. K. Nørskov, in *Impact of Surface Science on Catalysis* (Academic Press, 2000), pp. 71-129.
[113] M. Mavrikakis, B. Hammer, and J. K. Nørskov, Phys. Rev. Lett. **81**, 2819 (1998).
[114] A. Roudgar and A. Groß, Phys. Rev. B **67**, 033409 (2003).
[115] J. Zhang, M. B. Vukmirovic, Y. Xu, M. Mavrikakis, and R. R. Adzic, Angew. Chem. Int. Ed. Engl **44**, 2132-2135 (2005).
[116] B. Hammer, Faraday Disc. **110**, 323-333 (1998).
[117] K. Honkala, A. Hellman, I. Remediakis, A. Logadottir, A. Carlsson, S. Dahl, C. Christensen, and J. Nørskov, Science **307**, 555-558 (2005).
[118] G. Jones, J. G. Jakobsen, S. S. Shim, J. Kleis, M. P. Andersson, J. Rossmeisl, F. Abild-Pedersen, T. Bligaard, S. Helveg, B. Hinnemann, J. R. Rostrup-Nielsen, I. Chorkendorff, J. Sehested, and J. K. Nørskov, Journal of Catalysis **259**, 147-160 (2008).
[119] K. J. Andersson, F. Calle-Vallejo, J. Rossmeisl, and I. Chorkendorff, Journal of the American Chemical Society **131**, 2404-2407 (2009).
[120] J. Greeley, I. E. L. Stephens, A. S. Bondarenko, T. P. Johansson, H. A. Hansen, T. F. Jaramillo, J. Rossmeisl, I. Chorkendorff, and J. K. Nørskov, Nat. Chem. **1**, 552-556 (2009).
[121] F. Studt, F. Abild-Pedersen, T. Bligaard, R. Z. Sørensen, C. H. Christensen, and J. K. Nørskov, Science **320**, 1320 -1322 (2008).
[122] I. N. Remediakis, N. Lopez, and J. K. Nørskov, Applied Catalysis A: General **291**, 13-20 (2005).
[123] G. Wulff, Zeitschrift Fur Krystallographie Und Mineralogie **34**, 449-530 (1901).
[124] M. Arenz, K. Mayrhofer, V. Stamenkovic, B. Blizanac, T. Tomoyuki, P. Ross, and N. Markovic, Journal of the American Chemical Society **127**, 6819-6829 (2005).
[125] L. Gontard, L. Chang, C. Hetherington, A. Kirkland, D. Ozkaya, and R. Dunin-Borkowski, Angewandte Chemie - International Edition **46**, 3683-3685 (2007).
[126] S. Lee, S. Chen, J. Suntivich, K. Sasaki, R. Adzic, and Y. Shao-Horn, Journal of Physical Chemistry Letters **1**, 1316-1320 (2010).
[127] P. Ferrin and M. Mavrikakis, Journal of the American Chemical Society **131**, 14381-14389

(2009).
[128] N. Tian, Z. Zhou, and S. Sun, Journal of Physical Chemistry C **112**, 19801-19817 (2008).
[129] L. Vitos, A. Ruban, H. Skriver, and J. Kollár, Surface Science **411**, 186-202 (1998).
[130] J. Greeley, Electrochimica Acta **55**, 5545-5550 (2010).
[131] S. Bahn and K. Jacobsen, Computing in Science & Engineering **4**, 56-66 (2002).
[132] C. R. Henry, Surface Science Reports **31**, 231-325 (1998).
[133] A. Peterson, F. Abild-Pedersen, F. Studt, J. Rossmeisl, and J. Nørskov, Energy and Environmental Science **3**, 1311-1315 (2010).
[134] S. Trasatti, Pure Appl. Chem. **58**, 955-966 (1986).
[135] S. Schnur and A. Groß, New J. Phys. **11**, 125003 (2009).
[136] S. Trasatti, Electrochimica Acta **29**, 1503-1512 (1984).
[137] C. J. Cramer, *Essentials of Computational Chemistry: Theories and Models*, 2nd ed. (Wiley, 2004).
[138] D. Sholl and J. A. Steckel, *Density Functional Theory: A Practical Introduction* (Wiley-Blackwell, 2009).
[139] A. A. Gokhale, S. Kandoi, J. P. Greeley, M. Mavrikakis, and J. A. Dumesic, Chemical Engineering Science **59**, 4679-4691.
[140] *CRC Handbook of Chemistry and Physics* (CRC Press, New York, 1996).
[141] S. Trasatti, Surface Science **335**, 1-9 (1995).
[142] H. Ogasawara, B. Brena, D. Nordlund, M. Nyberg, A. Pelmenschikov, L. G. M. Pettersson, and A. Nilsson, Phys. Rev. Lett. **89**, 276102 (2002).
[143] G. Karlberg, J. Rossmeisl, and J. Nørskov, Physical Chemistry Chemical Physics **9**, 5158-5161 (2007).
[144] B. Hinnemann, P. G. Moses, J. Bonde, K. P. Jørgensen, J. H. Nielsen, S. Horch, I. Chorkendorff, and J. K. Nørskov, Journal of the American Chemical Society **127**, 5308-5309 (2005).
[145] C. H. Kjaergaard, J. Rossmeisl, and J. K. Nørskov, Inorganic Chemistry **49**, 3567-3572 (2010).
[146] J. Rossmeisl, A. Logadottir, and J. Nørskov, Chemical Physics **319**, 178-184 (2005).
[147] J. Rossmeisl, Z. Qu, H. Zhu, G. Kroes, and J. Nørskov, Journal of Electroanalytical Chemistry **607**, 83-89 (2007).
[148] J. Martínez, H. Hansen, J. Rossmeisl, and J. Nørskov, Phys. Rev. B **79**, (2009).
[149] M. A. Barteau, Catal Lett **8**, 175-183 (1991).
[150] Z. Liu and P. Hu, J. Chem. Phys. **114**, 8244 (2001).
[151] A. Michaelides, Z. Liu, C. Zhang, A. Alavi, D. King, and P. Hu, Journal of the American Chemical Society **125**, 3704-3705 (2003).
[152] N. Markovic, H. Gasteiger, and P. Ross, Journal of the Electrochemical Society **144**, 1591-1597 (1997).
[153] F. Abild-Pedersen, J. Greeley, F. Studt, J. Rossmeisl, T. R. Munter, P. G. Moses, E. Skúlason, T. Bligaard, and J. K. Nørskov, Phys. Rev. Lett. **99**, 016105 (2007).
[154] M. P. Andersson, T. Bligaard, A. Kustov, K. E. Larsen, J. Greeley, T. Johannessen, C. H. Christensen, and J. K. Nørskov, Journal of Catalysis **239**, 501-506 (2006).

[155] E. Fernndez, P. Moses, A. Toftelund, H. Hansen, J. Martínez, F. Abild-Pedersen, J. Kleis, B. Hinnemann, J. Rossmeisl, T. Bligaard, and J. Nørskov, Angewandte Chemie - International Edition **47**, 4683-4686 (2008).

[156] G. Jones, T. Bligaard, F. Abild-Pedersen, and J. K. Nørskov, J. Phys.: Condens. Matter **20**, 064239 (2008).

[157] J. K. Nørskov, T. Bligaard, A. Logadottir, S. Bahn, L. B. Hansen, M. Bollinger, H. Bengaard, B. Hammer, Z. Sljivancanin, M. Mavrikakis, Y. Xu, S. Dahl, and C. J. H. Jacobsen, Journal of Catalysis **209**, 275-278 (2002).

[158] J. K. Nørskov and N. D. Lang, Phys. Rev. B **21**, 2131 (1980).

[159] R. Parsons, Trans. Faraday Soc. **54**, 1053-1063 (1958).

[160] J. O. Bockris and T. Otagawa, The Journal of Physical Chemistry **87**, 2960-2971 (1983).

[161] T. Bligaard, J. Nørskov, S. Dahl, J. Matthiesen, C. Christensen, and J. Sehested, Journal of Catalysis **224**, 206-217 (2004).

[162] L. Grabow, B. Hvolbæk, and J. Nørskov, Topics in Catalysis **53**, 298-310 (2010).

[163] H. A. Hansen, I. C. Man, F. Studt, F. Abild-Pedersen, T. Bligaard, and J. Rossmeisl, Phys. Chem. Chem. Phys. **12**, 283 (2010).

[164] J. Kleis, G. Jones, F. Abild-Pedersen, V. Tripković, T. Bligaard, and J. Rossmeisl, J. Electrochem. Soc. **156**, B1447-B1456 (2009).

[165] J. Rossmeisl, G. S. Karlberg, T. Jaramillo, and J. K. Nørskov, Faraday Discuss. **140**, 337-346 (2009).

[166] J. K. Nørskov, T. Bligaard, A. Logadottir, J. R. Kitchin, J. G. Chen, S. Pandelov, and U. Stimming, J. Electrochem. Soc. **152**, J23-J26 (2005).

[167] M. Mavrikakis, Nat Mater **5**, 847-848 (2006).

[168] P. Sabatier, Ber. Dtsch. Chem. Ges. **44**, 1984-2001 (1911).

[169] J. Greeley and J. Nørskov, Electrochimica Acta **52**, 5829-5836 (2007).

[170] G. Henkelman, B. P. Uberuaga, and H. Jónsson, J. Chem. Phys. **113**, 9901 (2000).

[171] W. Vogel, P. Kaghazchi, T. Jacob, and N. Alonso-Vante, The Journal of Physical Chemistry C **111**, 3908-3913 (2007).

[172] Computational Materials Repository. https: //wiki.fysik.dtu.dk/cmr/.

[173] T. R. Munter, D. D. Landis, F. Abild-Pedersen, G. Jones, S. Wang, and T. Bligaard, Comput. Sci. Disc. **2**, 015006 (2009).

[174] N. Alonso-Vante, P. Bogdanoff, and H. Tributsch, Journal of Catalysis **190**, 240-246 (2000).

[175] D. Cao, A. Wieckowski, J. Inukai, and N. Alonso-Vante, J. Electrochem. Soc. **153**, A869-A874 (2006).

[176] F. Dassenoy, W. Vogel, and N. Alonso-Vante, The Journal of Physical Chemistry B **106**, 12152-12157 (2002).

[177] A. Lewera, J. Inukai, W. Zhou, D. Cao, H. Duong, N. Alonso-Vante, and A. Wieckowski, Electrochimica Acta **52**, 5759-5765 (2007).

[178] F. Dassenoy, W. Vogel, and N. Alonso-Vante, The Journal of Physical Chemistry B **106**, 12152-12157 (2002).

[179] E. Antolini, T. Lopes, and E. Gonzalez, Journal of Alloys and Compounds **461**, 253-262

(2008).
[180] S. Koh and P. Strasser, Journal of the American Chemical Society **129**, 12624-12625 (2007).
[181] F. Maillard, M. Martin, F. Gloaguen, and J. Léger, Electrochimica Acta **47**, 3431-3440 (2002).
[182] R. Yang, J. Leisch, P. Strasser, and M. F. Toney, Chemistry of Materials **22**, 4712-4720 (2010).
[183] G. Jóhannesson, T. Bligaard, A. Ruban, H. Skriver, K. Jacobsen, and J. Nørskov, Physical Review Letters **88**, 2555061-2555065 (2002).
[184] T. Housmans, A. Wonders, and M. Koper, Journal of Physical Chemistry B **110**, 10021-10031 (2006).
[185] D. C. Papageorgopoulos, F. Liu, and O. Conrad, Electrochimica Acta **52**, 4982-4986 (2007).
[186] H. Yano, J. Inukai, H. Uchida, M. Watanabe, P. Babu, T. Kobayashi, J. Chung, E. Oldfield, and A. Wieckowski, Physical Chemistry Chemical Physics **8**, 4932-4939 (2006).
[187] S. Mukerjee and J. McBreen, Journal of Electroanalytical Chemistry **448**, 163-171 (1998).
[188] L. Grabow, Y. Xu, and M. Mavrikakis, Phys. Chem. Chem. Phys. **8**, 3369 (2006).
[189] L. Kibler, A. El-Aziz, R. Hoyer, and D. Kolb, Angewandte Chemie - International Edition **44**, 2080-2084 (2005).
[190] N. Tian, Z. Zhou, S. Sun, Y. Ding, and Z. L. Wang, Science **316**, 732-735 (2007).
[191] S. Han, Y. Song, J. Lee, J. Kim, and K. Park, Electrochemistry Communications **10**, 1044-1047 (2008).
[192] E. Vayner, R. A. Sidik, A. B. Anderson, and B. N. Popov, The Journal of Physical Chemistry C **111**, 10508-10513 (2007).
[193] F. Abild-Pedersen, Phys. Rev. Lett. **99**, (2007).
[194] C. Klanner, D. Farrusseng, L. Baumes, C. Mirodatos, and F. Schüth, QSAR and Combinatorial Science **22**, 729-736 (2003).
[195] J. L. Rodgers and W. A. Nicewander, The American Statistician **42**, 59-66 (1988).
[196] H. A. Gasteiger and N. M. Marković, Science **324**, 48-49 (2009).

Useful web resources

http://wiki.fysik.dtu.dk/gpaw

Official webpage of the GPAW electronic structure code.

http://wiki.fysik.dtu.dk/ase

Official webpage of the ASE atomistic simulation environment.

http://wiki.fysik.dtu.dk/cmr

Official webpage of the Computational Materials Repository database management module.

http://webbook.nist.gov/chemistry

Thermochemical, thermophysical, and ion energetics data compiled by the National Institute of Standards and Technology (NIST).

http://cst-www.nrl.navy.mil/lattice

An index of common crystal lattice structures.

Publications

Paper I

Tuning the electro-catalytic performance of transition metal surfaces by alloying with chalcogen atoms

Tritsaris G. A., Nørskov J. K., Rossmeisl J. In preparation.

Tuning the electro-catalytic performance of transition metal surfaces by alloying with chalcogen atoms

G. A. Tritsaris*, J. K. Nørskov, J. Rossmeisl

Department of Physics, Center for Atomic-scale Materials Design, Technical University of Denmark, DK-2800 Lyngby, Denmark

Abstract

It is shown how the inclusion of chalcogen atoms in a transition metal surface can be used as a means to tune electro-catalytic performance. We use density functional theory calculations to evaluate the performance of model transition metal surfaces, both elemental and modified with selenium or sulfur, as cathode catalysts for low-temperature fuel cells. With ruthenium selenium as starting point, we study the effect of the chalcogen on the stability of the modified surfaces. An upper bound for their oxygen reduction reaction activity is established. We investigate their tolerance to methanol oxidation by simple thermodynamic considerations. The strength of the effect of the chalcogen is reflected on the strength of OH binding which assumes the role of a descriptor for the surface reactivity.

Introduction

Fuel cells represent a possible technology for the direct conversion of chemical bond energy to electricity. Different types of fuel cells have been developed depending on the intended application[1]. Low-temperature fuel cells such as the proton exchange membrane fuel cell (PEMFC)[2] are considered among the most suited solutions for mobile applications and for replacing combustion engines in vehicles. The design of novel and improved materials is imperative if efficiency and durability is desirable to such an extent that low-temperature fuel cells become an economically viable solution[3].

The performance of the catalytic materials remains one of the main challenges for PEMFC to overcome[4]. In present technology, the catalyst is Pt-based. Pt exhibits the highest catalytic activity over any other pure metal. Its high cost together with the significant cell voltage losses originating from the rather slow catalysis of the oxygen

reduction reaction (ORR) highlight the need for cathode catalysts of enhanced mass activity[5,6]. The challenge of hydrogen handling and storage may be circumvented for some portable systems with the use of methanol as fuel for direct-methanol fuel cells (DMFC). In this case, the selectivity of the cathode catalyst becomes of great importance. There will be a competition between the ORR and the combustion of methanol, should the latter reach the cathode electrode (the so-called 'methanol crossover' effect). A mixed potential reduces the output voltage of the fuel cell significantly[7,8]. Thus, a fundamental aspect in the development of fuel cells concerns the enhancement of the performance of the cathode catalyst in terms of mass activity and selectivity [5,9,10].

Transition metal surfaces enriched with chalcogen atoms (i.e. sulfur (S), selenium (Se) or tellurium(Te)) have been acknowledged as attractive candidates for cathode catalysts in low-temperature fuel cells. Although a range of chalcogen-modified materials of favorable catalytic performance has been reported, which are the exact mechanisms responsible for the observed increased ORR activity (compared to the respective pure transition metal surfaces) and tolerance to methanol oxidation (MO) still remains an open question. Efforts focus primarily on the elucidation of issues such as the effect of the chalcogen on the electronic structure, the surface structure of the catalyst and the nature of the catalytically active centers[5,11--13].

Ruthenium selenium (RuSe) is a well-studied cathode catalyst for low-temperature fuel cells, naturally serving as a starting point for the study of a set of transition metal chalcogenide surfaces. The kinetics of the ORR on pure Ru surfaces are dependent on the formation of a Ru oxide-like phase[14]. Ru is also known to be an active catalyst for MO. These two aspects render Ru an ineffective electro-catalyst. The work of Alonso-Vante et al.[15] has demonstrated that the performance of RuSe is unaffected by the presence of methanol. RuS also proves to be as insensitive as RuSe to MO[11,16] while the experimentally observed resistance of the Ru surface atoms to electro-chemical oxidation has been attributed to the modification of the nature of the metallic active centers by the presence of the chalcogen[16--19].

DFT studies of model surfaces have provided atomistic insights on different classes of reactions relevant to fuel cells operation, including hydrogen evolution[20], oxygen reduction[21] and methanol oxidation[22]. Such a theoretical investigation is important not only for fundamental reasons but with the identification of descriptors of the surface reactivity, the screening for catalysts of enhanced catalytic performance is facilitated[23--27].

In this work, we show with DFT calculations how the inclusion of chalcogen atoms in a transition metal surface can be used as a means for tuning electro-catalytic functionality. For that, we evaluate the catalytic performance of well-defined model surfaces of transition metal chalcogenides for use as cathode catalysts in low-temperature

fuel cells. We establish an upper bound for the ORR activity of the chalcogen-modified surfaces and we investigate the observed tolerance to MO by simple reaction thermodynamic considerations.

Models and methods

Model surfaces were constructed for the study of the catalytic performance of RuSe and other chalcogen-containing transition metal surfaces in the form of periodically repeated (2x2) or (2x3) slabs. Four atomic layers of transition metal atoms were used to describe pure metal reference slabs while for the chalcogen-modified surfaces one, two, three or four metal atoms in the top layer were substituted with either Se or S atoms in order to account for different surface coverage of the chalcogen (see Fig. 1). We distinguish between the different structures as $M_{1-x}X_x$ where M describes the transition metal and X to be either Se or S. The coverage of the chalcogen is quantified by the parameter *x* which assumes the values of 0, 0.25, 0.50, 0.75 and 1. The two limiting cases refer to a pure metal surface ($x = 0$) and a Ru surface covered with a monoatomic layer of chalcogen atoms ($x = 1$). Depending on the bulk crystal structure of each transition metal considered, the corresponding fcc(111), hcp(0001) or bcc(110) surface was modeled.

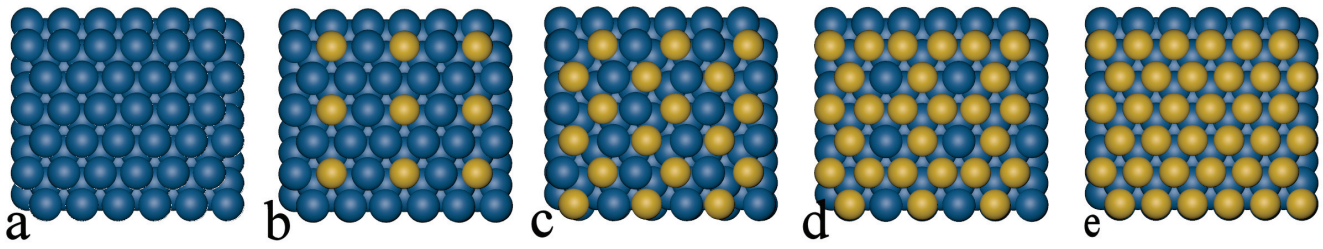

Fig. 1 Model of a a) pure fcc(111) surface ($x = 0$), Se-modified surface with b) small ($x = 0.25$), c) moderate ($x = 0.50$), d) high ($x = 0.75$) content in Se and a e) fcc(111) surface covered with a monolayer of Se ($x = 1$). The optimized structures are shown. An in-plane surface relaxation effect is observed for moderate Se content.

Total energy calculations were done with the GPAW package, a DFT implementation based on the projector-augmented wave (all electron, frozen core approximation) method[28]. It uses real-space uniform grids and multigrid methods (grid mode) as well as atom-centered basis functions (LCAO mode)[29]. For the description of exchange and correlation, the RPBE functional[30] was chosen and a Monkhorst-Pack mesh was used for integration in k-space. A set of 2 to 8 special points (depending on structure symmetry) were used for sampling the irreducible Brillouin zone. The grid spacing was set to $h = 0.15$Å as tradeoff between computational efficiency and accuracy and a stencil of $O(h^8)$ accuracy was used to discretize the kinetic energy Laplacian. The electron density is converged to 10^{-4} eV per valence electron. For structure optimization, the top 3 slab layers

were relaxed by minimization of all the interatomic forces to the upper limit of 0.05 eV/Å. For structures of more than 50 atoms, structure optimization was done in two steps, initially using the much faster LCAO mode using a double-zeta polarized basis set and then switching to the more accurate (but slower) grid mode.

Modeling a RuSe surface the way described above is justified on the grounds of the available literature. Different geometries have been suggested for the RuSe catalyst:
a) core-shell particles which comprise a hexagonally packed Ru core with the atoms in their native (hcp) lattice and a skin of either amorphous RuSe surface alloy or pyrite (space group n. 205) structure $RuSe_2$[11,18,19,31,32]
b) particles of bulk pyrite $RuSe_2$[33,34]

In any case, Se is expected to segregate to the surface. Atomic Se is insoluble in bulk Ru[35] and even when a bulk pyrite structure is the thermodynamically favorable phase, the surface will be rich in Se as reported calculations of low-index RuSe surfaces suggest[33].

Methods for describing electro-chemical reactions in a semi-quantitative way using the adsorption free energy of the reaction intermediates are well established[21,36--38]. For the purposes of our analysis, a four-electron transfer process is assumed for the cathode reaction, i.e. the reduction of O_2 to water. In acidic environment

(1) $\mathrm{O_2 + 4\left(H^+ + e^-\right) \rightarrow H_2O}$

The reaction comprises the following elementary steps:

(2)
1. $\mathrm{O_2 + H^+ + e^- + * \rightarrow HOO*}$
2. $\mathrm{HOO^* + H^+ + e^- \rightarrow H_2O + O*}$
3. $\mathrm{O* + H^+ + e^- \rightarrow OH*}$
4. $\mathrm{OH* + H^+ + e^- \rightarrow H_2O + *}$

where e^- is an electron in the electrode, H^+ a proton solvated in the electrolyte and * signifies an adsorption site on the surface. By setting the reference potential to be that of the standard hydrogen electrode the free energy of each elementary step is calculated from the binding energies of the ORR intermediates using $\mu\left(\mathrm{H^+ + e^-}\right) = 1/2\mu\left(\mathrm{H_2}\right) - eU$ where μ stands for the chemical potential[21]. The last term quantifies the effect of the electrode potential U on the chemical potential of the electrode electrons. As an example, the adsorption energy ΔE_{O} of O* is calculated as $\Delta E_{\mathrm{O}} = E_{\mathrm{surface/O}} - E_{\mathrm{surface}} - E_{\mathrm{H_2O(g)}} + E_{\mathrm{H_2(g)}}$, where $E_{\mathrm{surface/O}}$ and E_{surface} is the DFT total energy of a slab with and without O adsorbed respectively. $E_{\mathrm{H_2O(g)}}$ and $E_{\mathrm{H_2(g)}}$ are the gas

phase energies of a water and hydrogen molecule used here as reference states (we assume equilibrium between gas and liquid water at the pressure of 0.035bar). To account for the effect of the water environment in the electro-chemical cell on the binding energy of the intermediates, we fill the surface with water molecules in a way forming a hexagonal network of adsorbed species[39]. The calculated adsorption energies are corrected with zero-point energy (ZPE) and entropy (TS) contributions. Then, the binding free energy ΔG_{O} of O* will be given by $\Delta G_{\mathrm{O}} = \Delta E_{\mathrm{O}} + \Delta \mathrm{ZPE} + T\Delta S - \mathrm{e}U$. The ZPE and TS corrections are relevant to the adsorbate and they are taken from the work of Ferrin et al.[22]. The corresponding corrections for the slab are considered negligible and they are omitted. Thermal corrections to enthalpy are also assumed negligible. We consider the pH of the electrolyte to be 0 and we assume reaction barriers to be both potential and material independent[40]. For the calculation of the binding energy of all C-containing species, the gas phase energy of CO_2 serves as an additional reference energy. The latter is corrected by +0.45eV, an empirical correction based on a number of reactions studied with the RPBE functional[41].

Ruthenium chalcogenides

Given the harsh conditions under which the fuel cell cathode operates, it is of great interest to evaluate its stability. As a measure of stability, we calculate the energy per Se atom associated with the segregation of Se to the surface[42]. We do that by interchanging Ru atoms of the second layer with Se atoms of the top layer for $Ru_{1-x}Se_x$ surfaces with x = 0.25, 0.50 and 0.75. Neglecting any entropy contributions, we calculate the segregation energy as:

$$E_{segr} = \left(E\left(Ru_{1-x}Se_x; Ru_1Se_0 \right) - E\left(Ru_1Se_0; Ru_{1-x}Se_x \right) \right) / 4x \quad (3)$$

where the two terms represent the total energy of two different slab configurations. The semicolon delimits the composition of the first (left part) and second (right part) layer (see also supporting information). The sign of the excess free energy of mixing conveys information on the stability of our model surface alloys against phase separation effects[42]. We calculate the surface alloy mixing energy per unit surface area with a pure Ru slab and a Ru slab covered with a monoatomic skin of Se as reference as:

$$E_{\mathrm{mix}} = \left(E_{\mathrm{Ru_{1-x}Se_x}} - (1-x)E_{\mathrm{Ru_1Se_0}} - xE_{\mathrm{Ru_0Se_1}} \right) / \gamma \quad (4)$$

with γ representing the surface of the unit cell. E_{segr} is found to be negative for all surfaces (Table 1) showing the tendency of Se to enrich the surface. E_{mix} is calculated to be negative for all the different Se coverages (see Table 1), i.e. a surface ordered alloy surface is thermodynamically favored over phase separation. The absolute mixing energy maximizes for moderate (x = 0.50) content in Se. The origin of this maximum lies in an in-plane surface relaxation effect with mutual repulsion of the Se atoms (see also Fig. 1c).

Structure	E_{segr} (eV)	E_{mix} (eV/Å^2)
$Ru_{0.75}Se_{0.25}$	-2.35	-0.013
$Ru_{0.50}Se_{0.50}$	-2.21	-0.062
$Ru_{0.25}Se_{0.75}$	-1.44	-0.028

Table 1 Both the segregation and mixing energy are calculated as a measure of stability of three RuSe surfaces with different content in Se. In all cases diffusion of Se from the top layer to the bulk is associated with a high energy barrier. Phase separation is also found unfavorable. In terms of mixing energy, the most stable surface proves to be the one with moderate content in Se exhibiting an in-plane surface relaxation.

Experimental observations have established that the metallic Ru atoms act as the catalytically active centers of the RuSe surface[11,16,43]. In order to get insights into this property of the RuSe system, we calculate the binding strength of a 1/4ML of O on a pure Ru surface (x = 0) and on a Ru surface covered with a monolayer of Se (x = 1). The energy difference with respect to the pure metal surface is calculated to be 2.67eV, a fact that renders O binding to Se an event of relatively low probability (at least for a low O coverage). Moreover, the experimental observation[44] that, although Se in bulk is a semiconductor, it becomes metallic when embedded in the Ru surface is supported by the projected density of states (PDoS) on Se. Both the s and p bands are shown in Fig. 2 to cross the Fermi level in a continuous way.

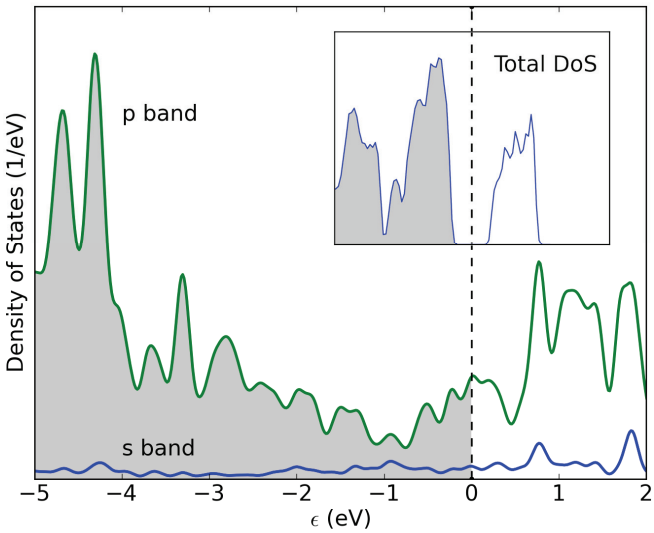

Fig. 2 Projected density of states on a Se atom of a clean $Ru_{0.50}Se_{0.50}$ surface and total density of states of Se bulk (inset). The gap around fermi level ($\varepsilon = 0$) of the total density of states renders Se in bulk a semiconductor. When Se is embedded in the surface of a transition metal becomes metallic as both the s and p bands cross the Fermi level in a continuous way.

We focus on the activity of the $Ru_{1-x}Se_x$ and $Ru_{1-x}S_x$ surfaces. For reaction intermediates coverages relevant to practical fuel cell operation[40], surfaces of low content in Se or S (x = 0.25) are expected to show similar activity to the pure Ru surfaces. Surfaces fully covered with the chalcogen (x = 1) are considered to be inactive since there will be no catalytically active (Ru) centers available. Thus, we limit our study to only two different coverages, moderate (x = 0.50) and high (x = 0.75). We estimate the activity of four different RuSe and RuS surfaces from the highest potential U_{ORR} for which no reaction step of Eqn. 2 is uphill in energy. The potential is calculated as $U_{ORR} = \min(-\Delta G_i)$ where ΔG_i refers to the reaction free energy of the i-th step for $U = 0$. The total change in free energy for Eqn. 1 is set to the experimental value of 4.92eV. The following order is established: $Ru_{0.50}Se_{0.50}$ > $Ru_{0.50}S_{0.50}$ > Ru > $Ru_{0.25}Se_{0.75}$ > $Ru_{0.25}S_{0.75}$ (Table 2). The adsorption free energies considered for the estimation of the activity together with constructed free energy diagrams can be found in the supporting information.

Structure	U_{ORR} (eV)	Structure	U_{ORR} (eV)	Structure	U_{ORR} (eV)	Structure	U_{ORR} (eV)
Pt	0.80	Rh	0.46	Ir	0.50	Pd	0.76
Ru	0.14	$Rh_{0.50}Se_{0.50}$	0.79	$Ir_{0.50}Se_{0.50}$	0.51	$Pd_{0.50}Se_{0.50}$	0.53
$Ru_{0.50}Se_{0.50}$	0.37	$Rh_{0.25}Se_{0.75}$	0.66	Co	0.14	$Pd_{0.25}Se_{0.75}$	0.55
$Ru_{0.25}Se_{0.75}$	0.13	$Rh_{0.50}S_{0.50}$	0.60	$Co_{0.50}Se_{0.50}$	0.33	W	-0.69
$Ru_{0.50}S_{0.50}$	0.21	$Rh_{0.25}S_{0.75}$	0.41	$Co_{0.50}S_{0.50}$	0.49	$W_{0.50}Se_{0.50}$	-0.72
$Ru_{0.25}S_{0.75}$	-0.13			$Co_{0.25}S_{0.75}$	0.08	$W_{0.25}Se_{0.75}$	-1.09

Table 2 The oxygen reduction reaction potential U_{ORR} for different chalcogenide surfaces has been calculated on the basis of the adsorption energy of the reaction intermediates.

Equally attractive to the reported favorable ORR activity of RuSe is its resistance to MO. We first estimate the potential needed for the initial activation of methanol on the (unselective) Pt surface which is known to be sensitive to methanol 'cross-over' effects. For an extensive DFT study of the methanol electro-oxidation reaction (MOR) the reader is advised to refer to the work of Ferrin et al.[22] There are two possible pathways for the activation of methanol, with its dehydrogenation to form either a hydroxymethyl CH_2OH or methoxide CH_3O intermediate:

$$CH_3OH_{(g)} \rightarrow CH_2OH^* + H^+ + e^- \text{ or } CH_3OH_{(g)} \rightarrow CH_3O^* + H^+ + e^-$$

We calculate that methanol activation on Pt takes places through CH_2OH. CH_3O binds to the surface less strongly by 0.95eV (see also Table S3). The associate change in free energy U_{MO} is then calculated to be equal to 0.43eV. Since the respective ORR activity is calculated U_{ORR} = 0.80eV, under a cathode electrode voltage of $U = U_{ORR} / e$ = 0.80V, U_{MO} will be shifted down to -0.37eV. The negative energy difference implies that methanol readily decomposes on the surface. The situation changes for the RuSe and RuS surfaces: For moderate chalcogen coverage methanol activation is prohibited since U_{MO} - U_{ORR} is calculated 0.19eV and 0.15eV respectively (Table S3). Both structures lie on the upper left part of Fig. 3 with $U_{MO} > U_{ORR}$. Pt lies on the lower right. We therefore suggest the relatively high potential needed for the activation of methanol as the origin of the observed suppression of methanol combustion on Ru chalcogenides.

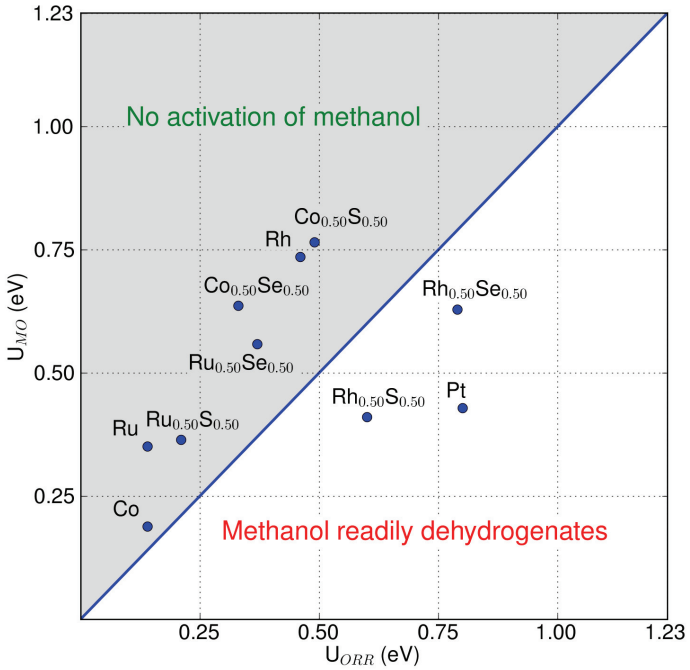

Fig. 3 The change in free energy U_{MO} for the initial activation of methanol is plotted against the activity for the oxygen reduction reaction. For structures lying on the upper left part of the plot methanol activation is thermodynamically unfavorable with $U_{MO} > U_{ORR}$. For structures lying on the lower right part methanol readily dehydrogenates since $U_{MO} < U_{ORR}$.

Transition metal chalcogenides

We now consider a broader set of chalcogenide surfaces for study. In addition to Ru, we consider surface alloys of Rh, Ir, Co, Pd and W with Se and S for x = 0.50 and x = 0.75 coverage. Surfaces of Pt and Cu were also considered which however proved to be too unstable for any subsequent analysis. In the following, the relative stability of the surfaces, their ORR activity, as well as their tolerance to MO is discussed.

Both Se and S are found to segregate to the top layer in all cases (see Table 3). Thus, even if a bulk alloy is the favored phase, thermodynamics suggest that the surface will be enriched in the chalcogen. In some cases (including RuSe), the clean surface is found to reconstruct with the chalcogen atoms relaxing out of the surface in order to compensate for the excess charge introduced by the chalcogen atoms. The surface will flatten on adsorbate binding. Although reaction-induced changes in the morphology of the catalyst surface can have a definite impact on reaction kinetics[45], the energy barrier for the surface flattening is found to be within DFT error (of the order of 0.05eV). The effect of reconstruction is left out of the discussion as it not expected to affect

our fundamental analysis and only unreconstructed surfaces are modeled. We calculate the mixing energy for all the different Se-modified surfaces (Fig. 4, see also Table S1). Two observations are made:

a) The mixing energy in all cases is negative (or slightly positive in the case of $Ir_{0.25}Se_{0.75}$) suggesting that an ordered surface alloy is thermodynamically favorable.

b) The absolute mixing energy is maximized for moderate (x = 0.50) content of Se, an effect ascribed to surface in-plane relaxation effects as in the case of RuSe.

Structure	E_{segr} (eV)	Structure	E_{segr} (eV)
$Ru_{0.50}Se_{0.50}$	-2.21	$Co_{0.50}Se_{0.50}$	-1.51
$Ru_{0.25}Se_{0.75}$	-1.44	$Co_{0.25}Se_{0.75}$	N.A.
$Rh_{0.50}Se_{0.50}$	-1.45	$Pd_{0.50}Se_{0.50}$	-0.82
$Rh_{0.25}Se_{0.75}$	-1.37	$Pd_{0.25}Se_{0.75}$	-0.31
$Ir_{0.50}Se_{0.50}$	-1.75	$W_{0.50}Se_{0.50}$	-2.82
$Ir_{0.25}Se_{0.75}$	-1.21	$W_{0.25}Se_{0.75}$	-2.30

Table 3 Diffusion of Se from the top to the second layer is calculated to be energetically unfavorable for all the surfaces considered here. $Co_{0.25}Se_{0.75}$ surface proves too unstable for any further analysis.

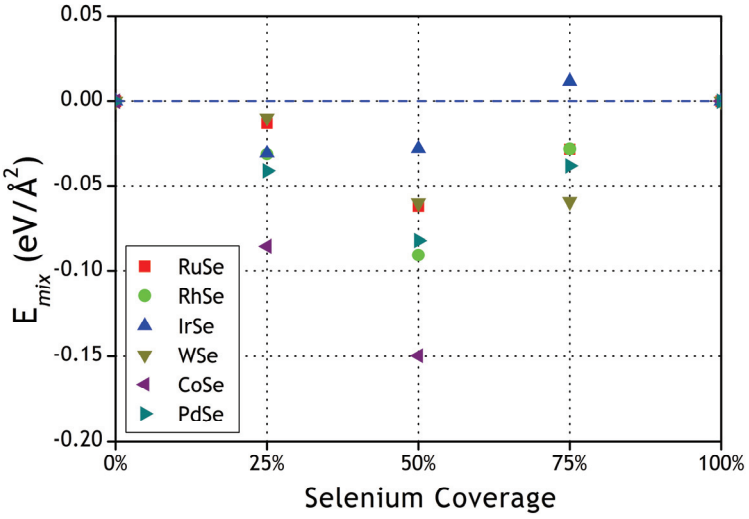

Fig. 4 The mixing energy for all the Se-modified surfaces screened in this study is calculated to be negative (or slightly positive in the case of $Ir_{0.25}Se_{0.75}$) suggesting that no phase separation is energetically favorable. The absolute mixing energy maximizes for moderate (x = 0.50) content in Se.

Identification of a descriptor or a set of descriptors for the catalytic activity is an important step towards fast screening for novel catalysts. The computational power needed for sampling the phase space of descriptors is only a fraction of the power needed for the detailed study of each candidate material. We identify one such descriptor for the ORR activity of chalcogen-modified transition metal surfaces, the binding energy of OH. The use of a single descriptor for the catalytic activity relies on the fact that correlations exist between the binding energies of the ORR intermediates for the surfaces studied.

Accounting for the effect of the electrolyte on the ORR kinetics although it renders our model more realistic and reliable, it increases the computational power requirements significantly. We circumvent the explicit modeling of the water environment of the cathode by making the observation that a correlation exists between the binding energies of the intermediates on a clean surface and a surface covered with the intermediates embedded in the water layer. We establish linear relationships between the binding energies of the ORR intermediates after performing calculations on all pure and selected chalcogen-modified metal surfaces. In Fig. 5a the binding energy of 1/4ML of OH on the clean surface of elemental surfaces and chalcogenides is plotted against and the corresponding energy of OH/H_2O of 1/3ML or 1/4ML coverage for elemental and chalcogenide surfaces respectively. A difference in the coverage for the OH/H_2O is expected to have non negligible effect on the calculated adsorption energies only when two OH are nearest neighbors, which is not the case here. A correlation is also identified between the binding energy of OH and 1/6ML of OOH/H_2O, the same for pure metals and chalcogenides (Fig. 5b). Therefore, the binding energies of OH/H_2O and OOH/H_2O are also correlated with a calculated energy difference of ~3.2eV between the two. Finally, the binding energy of a 1/4ML of O scales linearly with this of any of the other intermediates through a linear relationship with the binding energy of OH (Fig. 5c). Water has no effect on the binding of O since no stabilizing hydrogen bonds form, in contrast with the case of OH/H_2O or OOH/H_2O.

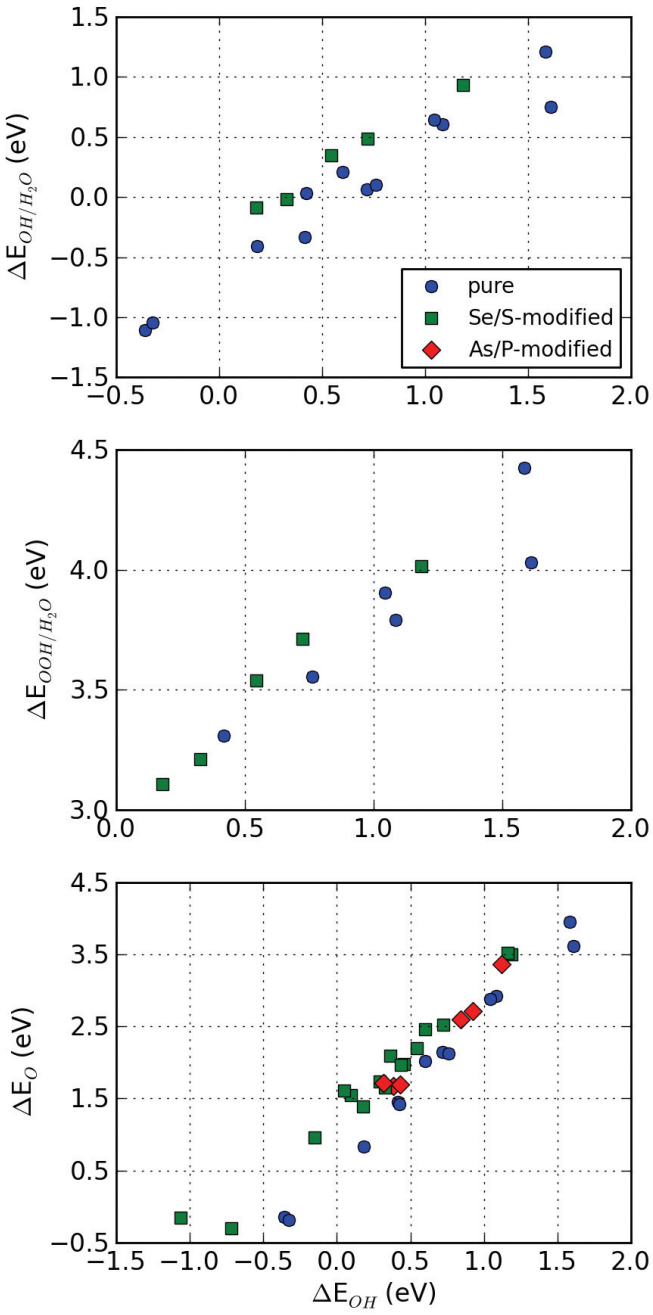

Fig. 5 Correlations are identified between the adsorption energy of OH on a clean surface and the adsorption energy of O, OH and OOH on the same surface covered with a water. Elemental (circles), chalcogen-modified (squares) transition metal surfaces and surfaces modified with other p-block elements, i.e. As and P (diamonds), share the same trends.

We now estimate the activity of Se and S-containing transition metal surfaces using the established linear relationships. Since the only material-dependent information is encoded in the calculated adsorption energies of

the different reaction species, our analysis allows for the direct comparison between the activity of the chalcogen-modified and the respective pure transition metal surfaces. An attempt for such a comparison is materialized in the form of the activity volcanoes shown in Fig. 6 where the binding energy $\Delta E^{c}_{OH/H_2O}$ of OH/H_2O is used as descriptor for the activity as calculated from its linear relationship with ΔE_{OH}. In the ascending left arm of the volcano, the activity is increased as OH binding on the surfaces weakens, while in the descending right arm, the trend in activity reverses. For the assumed ORR mechanism, for structures lying on the left arm it is the electron/proton transfer to OH that is the rate limiting step, see Eqn. (2.4). For structures lying on the right arm the overall rate is limited by the proton and electron transfer to adsorbed O_2, see Eqn. (2.2). Pt rests close to the top of the volcano reflecting its position as the most active pure metal catalyst for the ORR. Focusing on the chalcogenide surfaces, the activities of Rh chalcogenides shows a similar trend compared to Ru chalcogenides. Se-modified surfaces will outperform S-containing surfaces, in agreement with experiment[11]. Experiments report that modified Ru surfaces show increased activity over Rh surfaces[11,46][11]. The discrepancy between our findings and experiment could possibly rise from the fact that our model does not account for the specifics of the numerous possible surface phases. In any case, what we report is an estimation of the upper limit of the activity which does not conflict with the aforementioned experimental observations.

In Fig. 6 the distance between any point and the dashed line that represents the equilibrium potential of 1.23V gives the ORR overpotential for the respective structure. We see that the minimum value the overpotential can assume is equal to ~0.4V for both pure and chalcogen-modified surfaces. This fundamental limit has its origin in the difference between the binding energies of OH and OOH which is found fixed to ~3.2eV for all the surfaces considered here. The ideal ORR catalyst would require this difference to be twice the equilibrium potential, i.e. 2.46eV. Since this is not the case, the lowest potential possible is calculated (3.2 - 2.46) eV / 2e = ~0.4V.

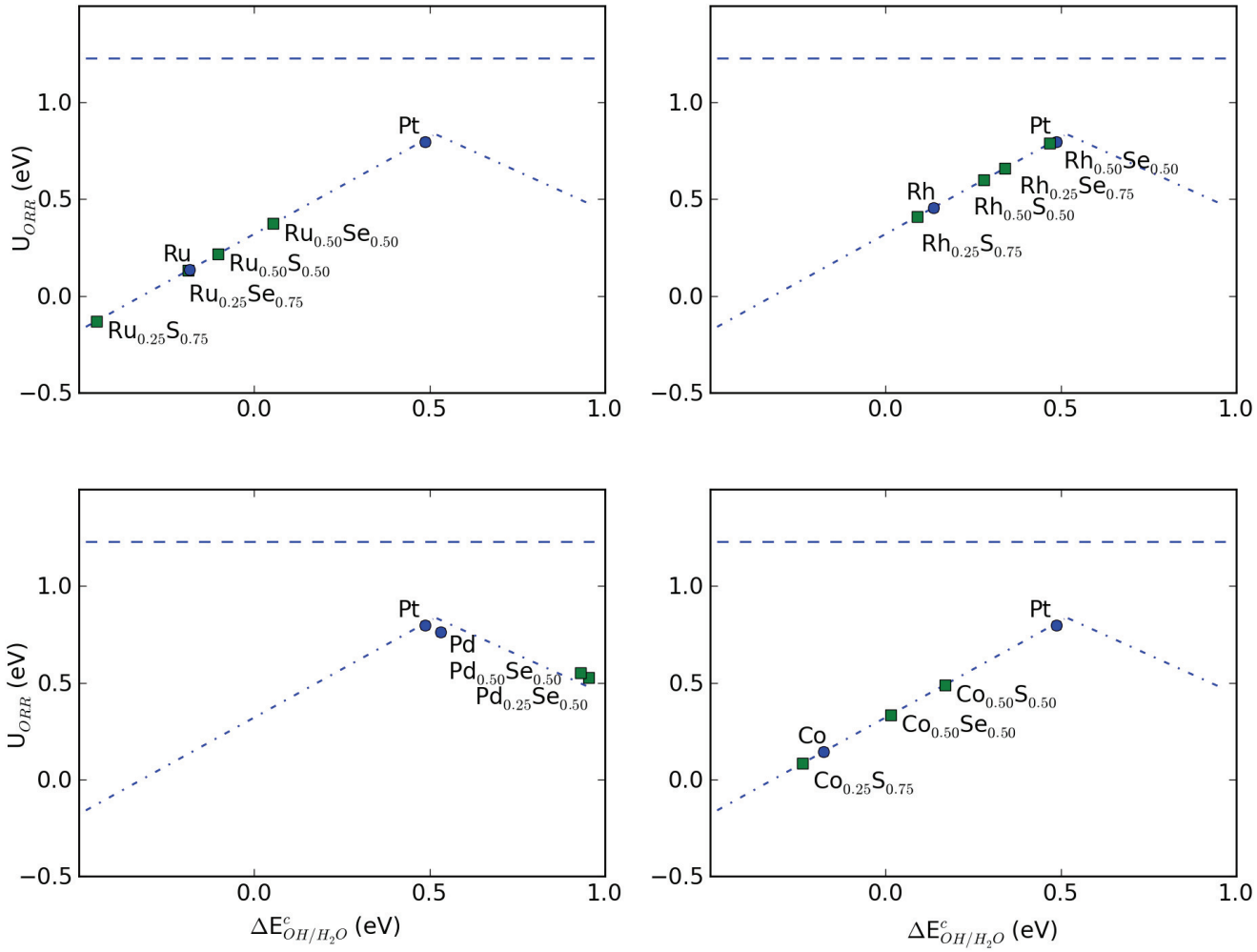

Fig. 6 Trends in oxygen reduction reaction activity for selected surfaces. The activity of each surface (see also Table 2) is plotted against the respective adsorption energy of OH. Pt is calculated to have the highest activity compared to both the pure (circles) and chalcogen-modified (squares) metal surfaces. Pure Pd also shows high activity and any modification with Se will deteriorate its performance. Ru and Rh surfaces modified with Se show increased activity compared to the S-modified surfaces. Activity maximizes for moderate (x = 0.50) content in chalcogen. The horizontal dashed line represents the equilibrium potential 1.23 eV.

We have used two different sets of linear relationships to describe the correlations of Fig. 5a,b, one for the pure metal and one for the chalcogen-modified surfaces for the construction of the volcanoes of Fig. 6. This distinction allows for increased accuracy in estimating relative activities between pure and chalcogenide surfaces that are closely situated on the volcano. Such differentiation is irrelevant over the complete range of values the adsorption energies assume. Effectively, both the pure metal and the chalcogen-modified surfaces are consider to belong to the same class of catalytic materials for ORR (given our assumption of a common reaction mechanism) with a

common volcano plot describing their activity. This conclusion is also supported by the reported activity of the different chalcogenides which are found at best comparable to this of Pt but never higher[11,13,47], Pt being the most active pure metal catalyst, situated on the very top of the activity volcano.

The dependence of the ORR kinetics on the strength of interaction between OH and the surface reflects the Sabatier principle which states that the catalytic activity maximizes when the binding of the reaction intermediates on the surface is neither too strong nor too weak. Modifying a transition metal surface with Se or S affects the binding between the catalyst and the reaction intermediates. Activity is shifted higher or lower depending on where the respective unmodified metal surface rests on the volcano. For example, modifying a Ru surface with Se will increase the activity since the weakening of the binding between the surface and the intermediates will position the resulting surface alloys more to the right of the volcano compared to the unmodified surface. On the other hand, modifying a Pd surface will only result in the deterioration of its activity since pure Pd already sits close to the top of the volcano.

We take a closer look at the effect of the chalcogen on the electronic structure of the surface. Looking for a direct link between the observed trends in catalytic activity of chalcogenide surfaces and their electronic structure, the significance of the position of the d-band center emerges. For the chalcogen-modified surfaces of our study, a linear relationship is found between the center of the d-band of the metal atoms and the adsorption energies of the ORR intermediates (Fig. 7, see also Table S2). The lower the metallic d-band center lies on the energy axis, the weaker the surface-adsorbate binding. Together with the fact that the binding energies are found to correlate with the surface's activity make the d-band center an alternative descriptor for the catalytic activity. Indeed, the importance of the d-band center as a reactivity descriptor is well established in the literature[25,48].

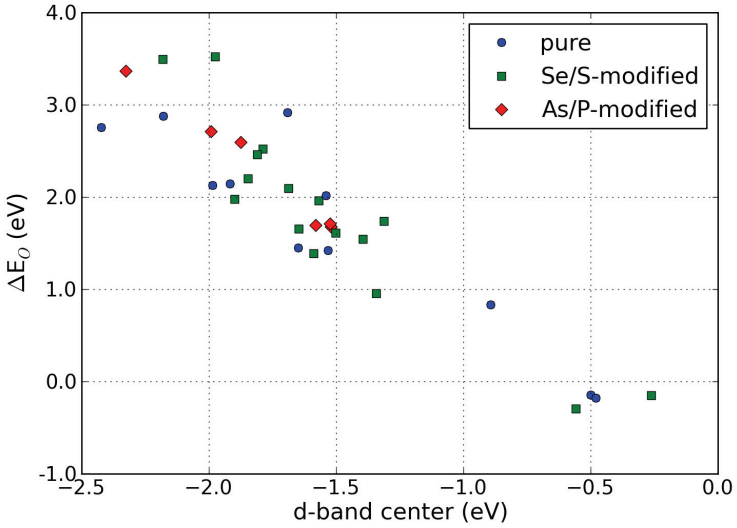

Fig. 7 A linear relationship is established between the d-band center of the metallic active centers on a pure (circles) or chalcogen-modified (squares) metal surface and the adsorption energy of the ORR intermediates. Transition metal surfaces modified with the group 15 elements As and P (diamonds) also share the same correlation.

Different methodologies have been suggested for fine-tuning the electronic structure of transition metal surfaces and thus of their catalytic activity, including alloying with other transition metal elements and induced strain[48]. We generalize to propose the inclusion of p-block elements in the surface as an alternative way of tuning the electro-chemistry of transition metal surfaces. To support our argument we perform calculations of transition metal surfaces of Ru, Rh and Pd modified with the group 15 elements As or P (also belonging to the p-block of the periodic table as Se and S). All prove to share the same linear relationships describing the pure and chalcogen-modified surfaces (Fig. 5, 7).

Finally, we seek the origin of the reported methanol tolerance of the chalcogenide surfaces in the relatively high potential needed for the MOR to initiate. To illustrate our point, we estimate the lowest potential needed for the initial dehydrogenation of methanol on selected chalcogen-modified surfaces of moderate content in chalcogen. For the chalcogen-modified surfaces of Ru and Co, U_{MO} is found high enough to completely inhibit the MOR from initiating (Fig. 3). Although pure Ru and Co surfaces are also calculated to be tolerant to MO, their low ORR activity together with their low stability makes them uninteresting as cathode catalysts. Looking at trends, the chalcogen-modified surfaces show increased tolerance. Since the estimated ORR activity provides an upper bound to the true activity and the calculated U_{MO} does not include any extra potential dependent barriers, the

minimum potential needed for activating methanol is expected to be higher than the calculated value reported here. Equivalently, accounting for extra barriers would result in a shift of all the points on Fig. 3 towards more positive values on the y-axis. This would result in increased tolerance for the Rh chalcogenides which are shown to lie on the lower right part of the plot. In any case, Rh chalcogenides are reported to show reduced tolerance to MO relatively to the Ru chalcogenides, a trend well captured by our model[46]. A complete study of the MOR mechanism however is beyond the scope of this study.

Conclusions

We employed DFT calculations and theoretical materials modeling to evaluate the stability, ORR activity and methanol tolerance of model chalcogen-modified transition metal surfaces for use as cathode catalysts for low-temperature fuel cells. Transition metal surfaces whether pure or modified with chalcogen atoms were shown to belong to the same class of ORR catalysts, described by the same activity volcano and susceptible to the same upper limits in ORR activity. The enhanced tolerance of chalcogenide surface alloys to MO is attributed to the high potential needed for the initial dehydrogenation of methanol. Effectively, we have demonstrated the ability to tune the chemistry of transition metal surfaces towards more favorable energetics for catalysis by the inclusion of p-block elements in the surface.

Addressing the problem of identifying novel and efficient catalysts requires substantial exchange between theory and experiment. In that respect, we demonstrated the importance of the binding energy of OH as a descriptor of the activity of transition metal/chalcogenide electro-catalysts, an experimentally accessible quantity, with the aim of backing up the experimental benchmarking of new catalysts.

Acknowledgements

Financial support by the International Graduate School of Science and Engineering is acknowledged. Center of Atomic-Scale Materials Design is funded by the Lundbeck Foundation. This work was supported by the Danish Center for Scientific Computing.

References

[1] L. Carrette, K. A. Friedrich, and U. Stimming, ChemPhysChem **1**, 162 (2000).

[2] G. J. K. Acres, J. C. Frost, G. A. Hards, R. J. Potter, T. R. Ralph, D. Thompsett, G. T. Burstein, and G. J. Hutchings, Catalysis Today **38**, 393 (1997).

[3] B. C. H. Steele and A. Heinzel, Nature **414**, 345 (2001).

[4] H. A. Gasteiger, S. S. Kocha, B. Sompalli, and F. T. Wagner, Appl. Catal. B Environ **56**, 9 (2005)
[5] L. Zhang, J. Zhang, D. P. Wilkinson, and H. Wang, J. Power Sources **156**, 171 (2006).
[6] B. Wang, J. Power Sources **152**, 1 (2005).
[7] A. S. Aricò, S. Srinivasan, and V. Antonucci, Fuel Cells **1**, 133 (2001).
[8] A. Hamnett, Catalysis Today **38**, 445 (1997).
[9] N. M. P. N. R. Markovic and P. N. Ross, CATTECH **4**, 110 (2000).
[10] M. Eikerling and A. A. Kornyshev, J. of Electroanal Chem 453, 89 (1998)
[11] D. Cao, A. Wieckowski, J. Inukai, and N. Alonso-Vante, J. Electrochem. Soc. **153**, A869 (2006).
[12] V. Trapp, P. Christensen, and A. Hamnett, Faraday Trans. **92**, 4311 (1996).
[13] E. Vayner, R. A. Sidik, A. B. Anderson, and B. N. Popov, J. Phys. Chem. C **111**, 10508 (2007).
[14] V. Le Rhun, E. Garnier, S. Pronier, and N. Alonso-Vante, Electrochemistry Communications **2**, 475 (2000).
[15] N. Alonso-Vante, P. Bogdanoff, and H. Tributsch, Journal of Catalysis **190**, 240 (2000).
[16] A. Lewera, J. Inukai, W. P. Zhou, D. Cao, H. T. Duong, N. Alonso-Vante, and A. Wieckowski, Electrochim. Acta **52**, 5759 (2007).
[17] M. Bron, P. Bogdanoff, S. Fiechter, I. Dorbandt, M. Hilgendorff, H. Schulenburg, and H. Tributsch, J Electroanal Chem **500**, 510 (2001).
[18] F. Dassenoy, W. Vogel, and N. Alonso-Vante, The Journal of Physical Chemistry B **106**, 12152 (2002).
[19] V. I. Zaikovskii, K. S. Nagabhushana, V. V. Kriventsov, K. N. Loponov, S. V. Cherepanova, R. I. Kvon, H. Bönnemann, D. I. Kochubey, and E. R. Savinova, The Journal of Physical Chemistry B **110**, 6881 (2006).
[20] E. Skulason, G. S. Karlberg, J. Rossmeisl, T. Bligaard, J. Greeley, H. Jonsson, and J. K. Norskov, Phys. Chem. Chem. Phys. **9**, 3241 (2007).
[21] J. K. Norskov, J. Rossmeisl, A. Logadottir, L. Lindqvist, J. R. Kitchin, T. Bligaard, and H. Jonsson, The Journal of Physical Chemistry B **108**, 17886 (2004).
[22] P. Ferrin, A. U. Nilekar, J. Greeley, M. Mavrikakis, and J. Rossmeisl, Surf. Sci. **602**, 3424 (2008).
[23] E. Reddington, A. Sapienza, B. Gurau, R. Viswanathan, S. Sarangapani, E. S. Smotkin, and T. E. Mallouk, Science **280**, 1735 (1998).
[24] V. R. Stamenkovic, B. S. Mun, M. Arenz, K. J. J. Mayrhofer, C. A. Lucas, G. Wang, P. N. Ross, and N. M. Markovic, Nat Mater **6**, 241 (2007).
[25] H. Toulhoat and P. Raybaud, Journal of Catalysis **216**, 63.
[26] M. Mavrikakis, Nat Mater **5**, 847 (2006).
[27] J. Greeley, T. F. Jaramillo, J. Bonde, I. Chorkendorff, and J. K. Norskov, Nat Mater **5**, 909 (2006).
[28] P. E. Blochl, Phys. Rev. B. Condens Matter **50**, 17953 (1994).
[29] J. J. Mortensen, L. B. Hansen, and K. W. Jacobsen, Phys. Rev. B **71**, 035109 (2005).
[30] B. Hammer, L. B. Hansen, and J. K. Nørskov, Phys. Rev. B **59**, 7413 (1999).
[31] J. Lee and B. Popov, Journal of Solid State Electrochemistry **11**, 1355 (2007).
[32] M. Shen, S. Chiao, D. Tsai, D. P. Wilkinson, and J. Jiang, Electrochim. Acta **54**, 4297 (2009).

[33] W. Vogel, P. Kaghazchi, T. Jacob, and N. Alonso-Vante, The Journal of Physical Chemistry C **111**, 3908 (2007).

[34] Y. Hara, N. Minami, and H. Itagaki, Applied Catalysis A: General **340**, 59 (2008).

[35] N. Bogolowski, T. Nagel, B. Lanova, S. Ernst, H. Baltruschat, K. Nagabhushana, and H. Boennemann, J. Appl. Electrochem. **37**, 1485 (2007).

[36] J. Rossmeisl, G. S. Karlberg, T. Jaramillo, and J. K. Nørskov, Faraday Discuss. **140**, 337 (2009).

[37] J. O. Bockris and T. Otagawa, J. Phys. Chem. **87**, 2960 (1983)

[38] S. Trasatti, Electrochimica Acta, **29**, 1503 (1984)

[39] H. Ogasawara, B. Brena, D. Nordlund, M. Nyberg, A. Pelmenschikov, L. G. Pettersson, and A. Nilsson, Phys. Rev. Lett. **89**, 276102 (2002).

[40] V. Tripkovic, E. Skúlason, S. Siahrostami, J. K. Nørskov, and J. Rossmeisl, Electrochimica Acta **55**, 7975 (2010).

[41] A. A. Peterson, F. Abild-Pedersen, F. Studt, J. Rossmeisl, and J. K. Nørskov, Energy Environ. Sci. **3**, 1311 (2010).

[42] A. Christensen, A. V. Ruban, P. Stoltze, K. W. Jacobsen, H. L. Skriver, J. K. Nørskov, and F. Besenbacher, Phys. Rev. B, **56**, 5822 (1997).

[43] L. Colmenares, Z. Jusys, and R. Behm J., Langmuir **22**, 10437 (2006).

[44] P. K. Babu, A. Lewera, J. H. Chung, R. Hunger, W. Jaegermann, N. Alonso-Vante, A. Wieckowski, and E. Oldfield, J. Am. Chem. Soc. **129**, 15140 (2007).

[45] G. Ertl, *Dynamics of reactions at surfaces* (Academic Press, 2000), volume 45, p. 1.

[46] D. C. Papageorgopoulos, F. Liu, and O. Conrad, Electrochim. Acta **52**, 4982 (2007).

[47] K. Lee, L. Zhang, and J. Zhang, J. Power Sources **165**, 108 (2007).

[48] B. Hammer and J. K. Nørskov, *Theoretical surface science and catalysis--calculations and concepts* (Academic Press, 2000), volume 45, p. 71.

Tuning the electro-catalytic performance of transition metal surfaces by alloying with chalcogen atoms

G. A. Tritsaris*, J. K. Nørskov, J. Rossmeisl

Department of Physics, Center for Atomic-scale Materials Design,

Technical University of Denmark,DK-2800 Lyngby, Denmark

Supporting information includes material on the calculation of segregation and mixing energies, tables summarizing the calculated binding energies of the oxygen reduction and methanol oxidation reaction intermediates and free energy diagrams for selected surfaces.

Segregation and mixing energy calculation

As a specific example, the segregation energy E_{segr} for $Ru_{1-x}Se_x$ with x = 0.25 (i.e. $Ru_{0.75}Se_{0.25}$) is calculated from the geometries shown in Fig. S1 as $E_{segr} = (E_a - E_b)$ where E_a and E_b correspond to the total energy of the structure of Fig. S1a and Fig. S1b respectively.

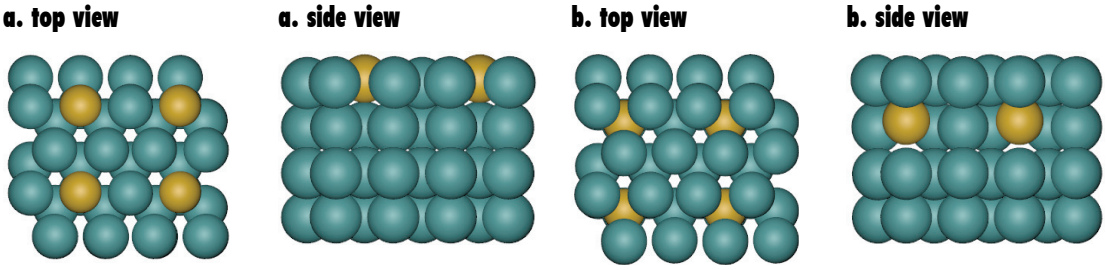

Fig. S1 Top and side views of the model surfaces used for the calculation of segregation energies. The unit cell is shown repeated two times along the x and y axis.

The mixing energy E_{mix} of $Ru_{0.75}Se_{0.25}$ is calculated as $E_{mix} = (E_a - 0.75E_c - 0.25E_s)/\gamma$ where E_c and E_s correspond to the structures shown in Fig. S2 and γ is equal to 26.20Å^2, the surface of the unit cell.

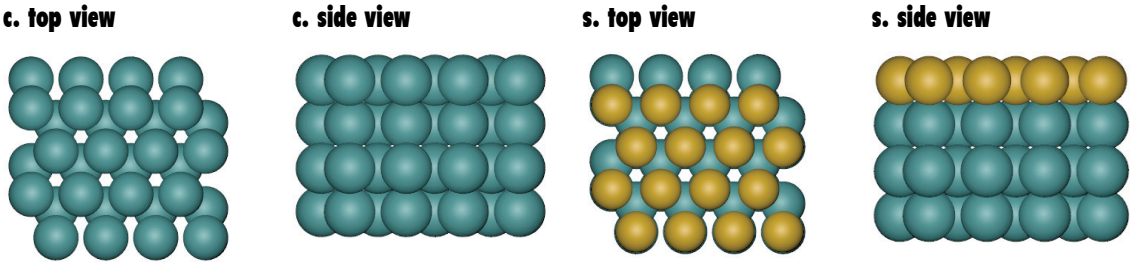

Fig. S2 Top and side views of the geometries used for the calculation of mixing energies. The unit cell is shown repeated two times along the x and y axis.

The mixing energies of a number of different Se-modified surfaces is calculated, plotted in Fig. 4 and summarized in Table S1.

x	RuSe	Rh	Ir	W	Co	Pd
0.25	-0.005	-0.019	-0.019	-0.005	-0.061	-0.024
0.50	-0.023	-0.056	-0.017	-0.033	-0.110	-0.048
0.75	-0.011	-0.017	0.007	-0.032	*N.A.*	-0.022

Table S1 The calculated mixing energies used in Fig. 4

Calculated adsorption energies

The calculated adsorption energies of all the oxygen reduction reaction intermediates are summarized in Table S2 (in eV):

Structure	O	OH	OH/H_2O	OOH/H_2O	d-band	Structure	O	OH	OH/H_2O	OOH/H_2O	d-band
Ru	1.45	0.42	-0.34	3.31	-1.65	$Rh_{0.50}Se_{0.50}$	2.52	0.72	0.49	3.71	-1.79
Ag	3.61	1.61	0.75	4.03	-3.99	$Rh_{0.25}Se_{0.75}$	2.46	0.60			-1.81
Au	3.95	1.58	1.21	4.42	-3.31	$Rh_{0.50}S_{0.50}$	2.20	0.54	0.35	3.54	-1.85
Pt	2.88	1.04	0.64	3.90	-2.18	$Rh_{0.25}S_{0.75}$	2.09	0.36			-1.69
Rh	2.15	0.72	0.06		-1.92	$Ir_{0.50}Se_{0.50}$	1.98	0.46			-1.90
Ir	2.13	0.76	0.10	3.55	-1.99	$W_{0.50}Se_{0.50}$	-0.30	-0.72			-0.56
Mo	-0.18	-0.32	-1.05		-0.48	$W_{0.25}Se_{0.75}$	-0.15	-1.06			-0.26
W	-0.14	-0.36	-1.11		-0.50	$Co_{0.50}Se_{0.50}$	1.74	0.29			-1.31
Cu	2.75		0.36	3.48	-2.42	$Pd_{0.50}Se_{0.50}$	3.49	1.18	0.93	4.02	-2.18
Pd	2.92	1.09	0.60	3.79	-1.69	$Pd_{0.25}Se_{0.75}$	3.52	1.16			-1.98
Ni	2.02	0.60	0.21		-1.54	$Co_{0.50}S_{0.50}$	1.96	0.44			-1.57
Fe	0.83	0.18	-0.41		-0.89	$Co_{0.25}S_{0.75}$	1.61	0.05			-1.50
Co	1.42	0.42	0.04		-1.53	$Ru_{0.50}As_{0.50}$	1.68	0.39			-1.52
$Ru_{0.50}Se_{0.50}$	1.66	0.33	-0.02	3.21	-1.65	$Ru_{0.25}As_{0.75}$	1.71	0.32			-1.52
$Ru_{0.25}Se_{0.75}$	1.55	0.10			-1.40	$Ru_{0.50}P_{0.50}$	1.69	0.43			-1.58
$Ru_{0.50}S_{0.50}$	1.39	0.18	-0.09	3.11	-1.59	$Rh_{0.50}As_{0.50}$	2.59	0.84			-1.87
$Ru_{0.25}S_{0.75}$	0.96	-0.15			-1.34	$Rh_{0.50}P_{0.50}$	2.71	0.92			-1.99
						$Pd_{0.50}As_{0.50}$	3.37	1.12			-2.33

Table S2 Adsorption energies of all the oxygen reduction reaction intermediates relevant to the calculation of the surfaces activity (in eV). All the adsorption energies correspond to the on top metallic binding site. As reference energies, the gas phase energies $E_{H_2O(g)}$ = -14.01eV and $E_{H_2(g)}$ = -6.73eV were used.

Reaction free energy diagrams

From the calculated adsorption energies, summarized in Table S2, free energy diagrams for the oxygen reduction reaction are constructed. The reaction free energy diagrams for selected surfaces are shown in Fig. S3. All the energy levels are shown, shifted by $-eU$ = -1.23eV. Fig. S3 shows that the potential-determining step for the Ru chalcogenides is the proton/electron transfer to the adsorbed OH, since it is characterized by the largest positive change in free energy along the reaction path. It is also clearly shown that $Ru_{0.50}Se_{0.50}$ will show a higher activity compared to $Ru_{0.25}S_{0.75}$ since the former binds OH less strongly. Pt, the best known monometallic catalyst, shows a much higher activity since the OH binding is much weaker.

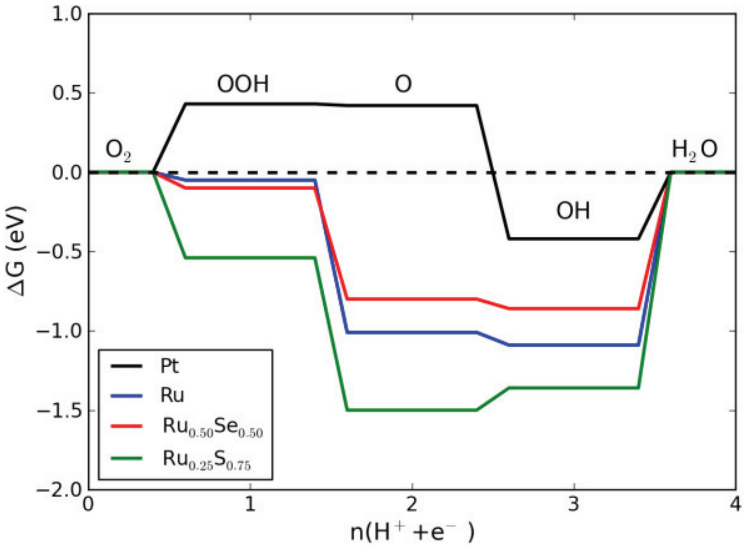

Fig. S3 Free energy diagrams for the oxygen reduction reaction constructed from the data shown in Table S2.

Methanol activation

For the estimation of the methanol activation free energy, we calculate the adsorption energy of both ΔG_{CH_2OH} and ΔG_{CH_3O} on selected surfaces. The activation energy U_{MO} (U = 0) is calculated as the difference between the adsorption energy of the strongest binding intermediate and gas phase methanol $\Delta G_{CH_3OH(g)}$ = 0.04eV. Methanol will dehydrogenate on a surface if U_{MO} ($U = U_{ORR}$ / e) = U_{MO} (U = 0) - U_{ORR} assumes a negative value. Table S3 summarizes the calculated adsorption energies and the calculated U_{MO}.

Structure	ΔG_{CH_2OH} (eV)	ΔG_{CH_3O} (eV)	U_{MO} (U = 0) (eV)	U_{MO} (U = U_{ORR}/e) (eV)
Pt	0.46	1.41	0.43	-0.37
Ru	0.76	0.38	0.74	0.28
$Ru_{0.50}Se_{0.50}$	0.67	0.59	0.56	0.19
$Ru_{0.50}S_{0.50}$	0.51	0.40	0.36	0.15
Rh	0.77	0.79	0.74	0.28
$Rh_{0.50}Se_{0.50}$	0.66	1.04	0.63	-0.16
$Rh_{0.50}S_{0.50}$	0.44	0.73	0.41	-0.19
Co	1.24	0.22	0.19	0.05
$Co_{0.50}Se_{0.50}$	0.72	0.67	0.64	0.31
$Co_{0.50}S_{0.50}$	0.90	0.80	0.77	0.28

Table S3 Calculated adsorption energies of the two possible methanol oxidation intermediates after one proton/electron transfer step and the relevant free energy change U_{MO} at zero (U = 0) and $U = U_{ORR}$ / e potential.

Paper II

Methanol electro-oxidation catalysis on elemental and bimetallic transition metals surfaces

Tritsaris G. A., Rossmeisl J. In preparation.

Methanol electro-oxidation catalysis on elemental and bimetallic transition metals surfaces

Department of Physics, Center for Atomic-scale Materials Design,

Technical University of Denmark, DK-2800 Lyngby, Denmark

G. A. Tritsaris, J. Rossmeisl

Abstract

We develop a framework for the study of the methanol electro-oxidation reaction (MOR) for direct methanol fuel cells using density functional calculations and theoretical materials modeling. Under a unified methodology, we discuss trends in reactivity of a set of monometallic and bimetallic transition metal model surfaces, flat and stepped, including non-precious alloys, overlayer structures and modified edges. All are found susceptible to the same upper limit of activity. A bi-functionality model is employed to screen for novel alloys of enhanced activity and we investigate a family of PtCu surfaces identified as promising catalysts by evaluating their reactivity and stability. In the same time, we try to expand the current molecular-level understanding of size effects in MOR catalysis by demonstrating the importance of modeling low-coordinated active sites such as steps in bridging the structure gap between studies of single crystal surfaces and realistic nanoparticles.

Introduction

The current worldwide trend of increasing energy demands together with the growing concerns over the related environmental problems have triggered an intensified effort for the realization of efficient and pollutant-free energy delivery. Fuel cells stand today as a key enabling technology for clean energy. Low-temperature fuel cells such as the direct methanol fuel cells (DMFC) are promising candidates as power sources for portable applications [1,2]. Improvement of the catalytic performance of the fuel cell electrodes proves a major materials science challenge related to current DMFC technology research. Both fundamental and development-oriented research is essential for the identification of novel and improved electro-catalysts [2,3].

The methanol electro-oxidation reaction (MOR) [3,4], taking place on the anode, is a 6-electron transfer process described by the overall reaction:

$$1)\ CH_3OH+H_2O \rightarrow CO_2+6\left(H^+ + e^-\right)$$

Even the current state-of-the-art DMFC anode catalysts, exclusively Pt-based [5], prove problematic mainly because of surface poisoning by CO, a strongly binding reaction intermediate [6]. In that respect, catalysts with increased CO tolerance are desirable. Another hindrance closely related to the commercialization of the DFMC technology is the cost of the catalyst [5], effectively calling for a reduction in the noble metal loading or, equivalently, for catalysts of increased mass activity.

Several strategies [7] have been identified for overcoming the aforementioned obstacles, including increasing the utilization of the noble metal by alloying [8-11], tailoring the morphology of the catalyst towards increased CO tolerance and enhanced activity [12-14] and the exploration of new non-precious metal catalysts [5,15]. The MOR comprises a complex reaction mechanism and although significant efforts have been invested into the elucidation of the reaction pathway, most related studies focus mainly on Pt or Pt-based alloys [4,16-19] of a well-defined geometry (such as single crystal model surfaces) and/or under idealized conditions. This is not always directly transferable to the realistic picture of dispersed catalyst nanoparticles functioning under the harsh electro-chemical environment of the DMFC [20-22]. In general, systematic research on other than Pt-based materials is limited [23,8] further hindering the search for inexpensive MOR electro-catalysts.

Density functional theory (DFT) based methods have provided us with atomistic insights into many different classes of chemical reactions relevant to fuel cells operation, including the MOR [23-27]. We use DFT calculations and theoretical modeling to develop a set of tools and methods for the study of DMFC anode catalysis. Our study aims at demonstrating the aforementioned challenges in MOR catalyst development can be treated theoretically under a common framework. Correlations between the binding energies of key MOR intermediates [25,28,29] allow for the construction of volcano plots on the basis of which we discuss trends in reactivity over a set of different transition metal surfaces, flat and stepped. We develop a methodology for screening for high performance MOR electro-catalysts, accounting for bi-functionality effects. This way, we demonstrate a knowledge-driven procedure for enhancing MOR catalysis. Finally, modeling low-coordinated surface sites such as steps [6,14,30-32] helps in elucidating the link between studies of the MOR on idealized single crystal surfaces and realistic nanoparticle catalysts [33] and in expanding the current molecular-level understanding of size effects in catalysis [34-37].

Model and computational details

Extended model slabs were constructed for the study of the MOR on all different transition metal surfaces. For the flat surfaces periodically repeated (2x2) slabs of three atomic layers were used. Depending on the bulk crystal structure of each transition metal, the corresponding close-packed fcc(111), hcp(0001) or bcc(110) surface were modeled. Stepped surfaces were modeled as fcc(211) surfaces for fcc and hcp metals and as bcc(310) for the bcc metals, both with nine atomic layers in a (1x2) slab. All slabs were surrounded with 13Å of vacuum in the simulation cell. Total energy calculations were performed with the GPAW package, a DFT implementation based on the projector-augmented wave (all electron, frozen core approximation) method [38]. It uses real-space uniform grids and multigrid methods [39,40]. For the description of exchange and correlation, the RPBE functional [41] was chosen and a Monkhorst-Pack mesh was used for k-space integration. A set of 2 to 8 special points (depending on structure symmetry) was used for sampling the irreducible Brillouin zone. The grid spacing was set to h = 0.18Å as a tradeoff between computational efficiency and accuracy and a stencil of O(h^8) accuracy was used to discretize the kinetic energy Laplacian. The energies were converged to 10^{-4} eV per valence electron. For structure optimization, the top 1 or 3 slab layers (for flat or stepped surfaces respectively) were relaxed by the minimization of all inter-atomic forces to the upper limit of 0.045 eV/Å.

For our analysis, we adopt the approach of the "computational hydrogen electrode" as it has been introduced by Nørskov et al. [25] Briefly, the MOR pathway is sampled on the basis of DFT calculated binding energies of key reaction intermediates after these energies are corrected with zero-point energy and entropic contributions. The corrections used in our study are taken from the work previously published by Ferrin et al. [23] Thermal corrections to enthalpy are assumed negligible. For closed-shell molecules the respective gas phase energy is used [23,25], corrected by +0.45eV when a O-C-O backbone is present (as in the case of HCOOH and CO_2), an empirical correction based on a number of reactions studied with the RPBE functional [42]. Other energy corrections include the stabilization of R-OH species by 0.15eV, OH by 0.25eV and CO by 0.10eV [42] as an approximation for the effect of the electrolyte (see also supporting information). Since the terraces of fcc(211) and fcc(111) surfaces share the same geometry these corrections are applicable to both geometries. The relation between the anode potential U (versus the reversible hydrogen electrode) and the chemical potential of an

electrode electron is accounted for by shifting the electron energy by -eU where e is the elementary positive charge. Our model implicitly assumes acidic environment of pH = 0. We then estimate the overpotential as the potential U_{MOR} for which the change in energy between every two consecutive steps along a given MOR path becomes zero or negative. We assume any energy barriers to be negligible. Although such an assumption would limit the reliability of a detailed study of the MOR mechanism on a surface in isolation, the model captures all the essential science for an accurate description of relative trends in the reactivity over the different surfaces. Since all material-dependent chemical information is encoded in the adsorption energy of the various MOR intermediates, we calculate the free energy of 15 different intermediate states [23,8] from the binding energy of the corresponding MOR species(Table S1). Although all non-equivalent sites were calculated, any reference to the calculated binding energies concerns only the most stable binding site identified for each surface/intermediate combination.

Results and discussion

A 'dual-path' mechanism is generally recognized for the electro-chemical oxidation of methanol to CO_2 which comprises two different parallel pathways: In the 'direct' or 'active intermediate' path, methanol oxidizes directly to CO_2 without passing through a poisoning intermediate such as CO in contrast with the 'indirect' or 'poisoning intermediate' path where the mechanism proceeds via the formation of poisoning species [4,43,44].

Table 1 summarizes the potentials U^{d}_{MOR} and U^{i}_{MOR} corresponding to the direct and indirect pathway as calculated from a database of adsorption energies of MOR intermediates (Table S1). Fig. 1 visualizes the difference between the two potentials for the flat and stepped surfaces. By inspection of Fig. 1 we see that $U^{i}_{MOR} \geq U^{d}_{MOR}$ in all cases which suggests that the direct mechanism should be operational already at relatively low potentials. The contribution of direct mechanism to the anode's current is expected to be low because of the CO poisoning of the surface. Thus, the anode's activity will be greatly dependant on the lowest potential that the indirect mechanism can run which allows for the removal of the poisoning intermediate. At high enough potentials both pathways will contribute but for potentials lower than U^{i}_{MOR} the overall activity is expected to be low. For this reason, in the following we will only consider the indirect pathway in our discussion unless stated otherwise. A more detailed discussion on the MOR on flat transition metal surfaces on the basis of DFT calculations is found in the work of Ferrin et al. [23,45]

	Ag	Au	Co	Cu	Fe	Ir	Ni	Pd	Pt	Rh	Ru
$U^{d}_{MOR,s}$ (V)	1.05	1.03	0.52	0.46	0.51	0.37	0.46	0.54	0.29	0.33	0.22
$U^{i}_{MOR,s}$ (V)	1.05	1.03	1.22	0.57	0.88	1.10	0.94	0.58	0.90	1.06	0.90
$U^{d}_{MOR,t}$ (V)	1.28	1.29	0.26	0.89	0.57	0.52	0.52	0.69	0.41	0.74	0.37
$U^{i}_{MOR,t}$ (V)	1.28	1.29	0.59	0.97	1.07	0.64	0.52	0.93	1.00	0.74	0.60

Table 1 Potentials calculated from a database of adsorption energies of methanol oxidation reaction intermediates. The subscripts signify a flat (terrace, 't') and stepped ('s') surfaces. The potential for the indirect mechanism is always found equal to or greater than this of the direct mechanism. Since the direct mechanism will mostly contribute to the anode's current only after the removal of the poisoning CO from the surface, it is the potential corresponding to the indirect mechanism that we use as estimation for the reaction overpotential.

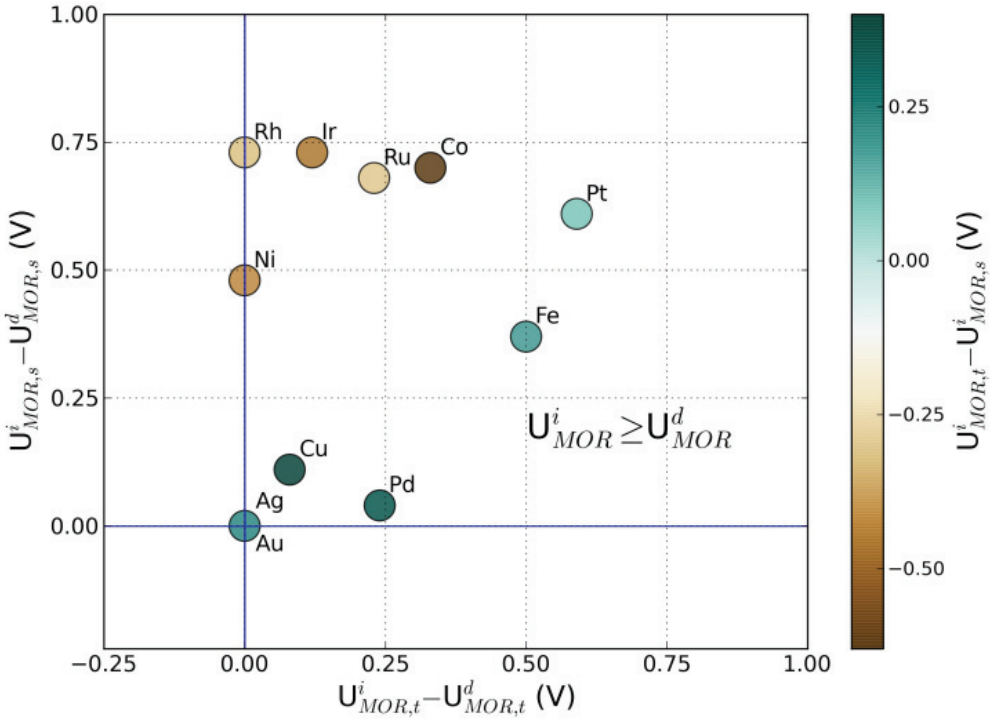

Fig. 1 Difference between the potential U^{i}_{MOR} for the indirect and U^{d}_{MOR} for the direct mechanism for flat (x axis) versus stepped surfaces (y axis). All surfaces are located at the upper-left quadrant since $U^{i}_{MOR} \geq U^{d}_{MOR}$ in all cases. For points of blue shades, the indirect mechanism potential for the respective elemental surface is found higher for the flat surface compared to the stepped one. Shades of brown signify the opposite trend.

In order to gain more insight into the reaction mechanism, we proceed to construct a volcano plot where the potential U_{MOR} is plotted versus an appropriately selected set of reactivity descriptors. This way trends in the

surface reactivity are revealed. The activity of different surfaces can then be studied under a common framework and conditions to be satisfied for enhanced catalysis are hinted (e.g. optimal descriptors values) [23,25,46]. For reasons discussed later in the article, we use ($\Delta G_{CO}, \Delta G_{OH}$) pairs to represent the phase space of reactivity descriptors for the MOR, where ΔG_{CO} and ΔG_{OH} correspond to the binding energy of CO and OH respectively. Plotting U^{i}_{MOR} against ($\Delta G_{CO}, \Delta G_{OH}$) results in a 3-d volcano plot presented as 2-d filled contour plot in Fig. 2.

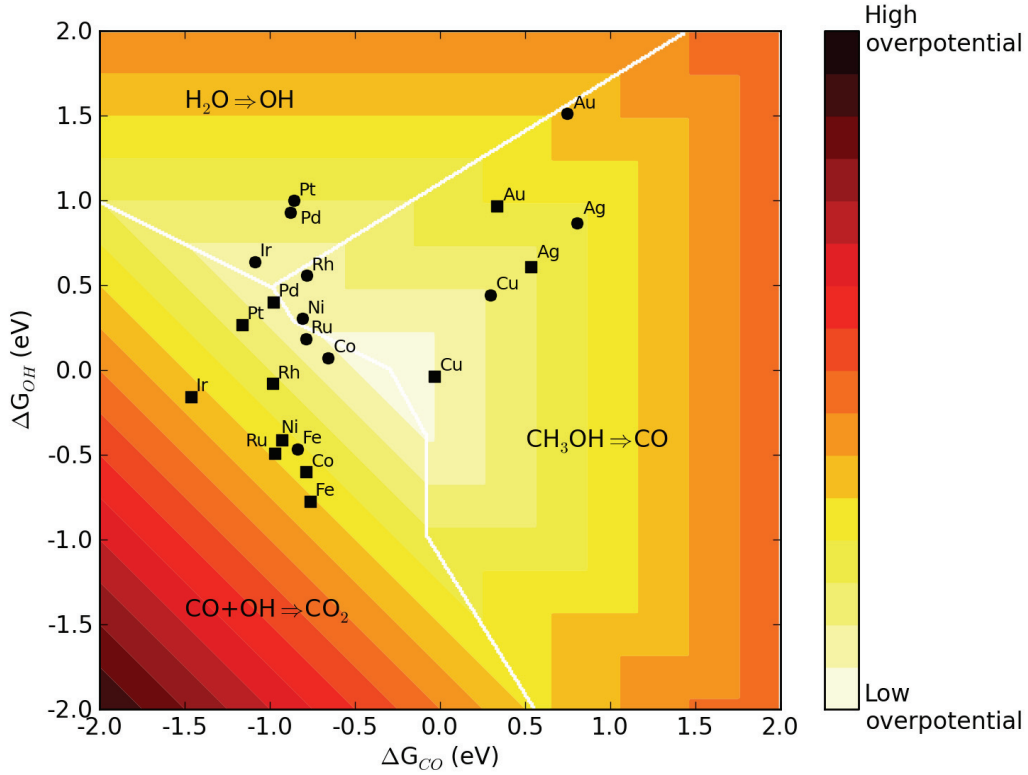

Fig. 2 Volcano plot for the indirect mechanism. All surfaces are positioned on the volcano according to the strength of CO and OH binding. Stepped surfaces (squares) show stronger binding than flat surfaces (circles). The overpotential minimizes only over an area (white color) of optimal CO and OH adsorption energies. The plot is divided in three distinct regions, each one corresponding to a different potential-determining step.

Each surface studied is positioned on the volcano plot according to the surface-specific values of ΔG_{CO} and ΔG_{OH}. The potential U^{i}_{MOR} shows a minimum for a rather well-defined area of the phase space (white areas in Fig. 2). Care must be taken for the correct interpretation of the volcano. A low value for U^{i}_{MOR} does not

necessarily go hand-in-hand with experimentally measured high activity. The volcano plot does not derive from a reaction kinetic model which accounts for the reaction rate prefactors. Moreover, stability issues can render a surface completely ineffective in the acidic environment of the DMFC as in the case of Cu or Co. Nonetheless, such volcano plots provide us with important insights: The minimum is calculated U^{i}_{MOR} = 0.29V. Although the MOR has a thermodynamic potential of ~0.02V, the complexity of the reaction mechanism is such that the activity of any monometallic surface is bounded by a significant upper limit. U^{i}_{MOR} minimizes at the point where both ΔG_{CO} and ΔG_{OH} assume intermediate values, i.e. the binding of both CO and OH on the surface must be only moderately strong for the surface reactivity to maximize, a manifestation of the Sabatier principle.

With OH as a model for activated water [4,47], we assume the following reaction mechanism for the indirect mechanism:

a. $CH_3OH \rightarrow CO + 4\left(H^+ + e^-\right)$

2 b. $H_2O \rightarrow OH + \left(H^+ + e^-\right)$

c. $CO + OH \rightarrow CO_2 + \left(H^+ + e^-\right)$

Step 1 describes the oxidation of methanol to CO, step 2 describes the activation of water to form OH and step 3 the combination of the surface CO and OH to form the final product, CO_2. The volcano plot is then separated in 3 distinct regions, each one corresponding to a different potential-determining step (PDS), i.e. the reaction step characterized by the highest energy difference for $U = 0$ and the last channel to open for $U = U^{i}_{MOR}$. A good anode catalyst for DMFC simultaneously satisfies the following three conditions:

a) is active towards forming CO from methanol

b) easily activates water

c) binds both CO and OH moderately so CO_2 can form

An efficient catalyst will have the potentials corresponding to each of the above processes equal to each other and an ideal one all three equal to zero. Fig. 2 shows that such an ideal catalyst is not realizable.

For Pt, the reference elemental catalyst, it has been reported that CO will preferentially adsorb at steps, where it oxidizes [48]. Housmans and Koper [30] also report an increase in the overall MOR activity of Pt with increasing

step density. We identify the PDS for the indirect mechanism on Pt fcc(211) to be the oxidation of CO and we calculate $U^{i}_{MOR,s} \geq U^{i}_{MOR,t}$, in agreement with the experiments.

By considering the position of any stepped model surface relatively to the corresponding flat one on the volcano plot a shift towards more negative values for both ΔG_{CO} and ΔG_{OH} is readily recognizable. Under-coordinated atoms, such as those on steps, will bind OH and CO more strongly. The observed shift is rationalized on the basis of the d-band model [28,29]. The d-band of stepped surfaces is narrower compared to that of terraces and for late transition metals its center shifts upward and closer to the Fermi level. The higher the d-band center is positioned, the stronger the interaction between the surface and the adsorbate is. The effect of stabilization of CO becomes less pronounced with decreasing occupancy of the transition metal d-band. For the metals that lie on the upper right part of the volcano, the stepped surfaces will show lower overpotential as they are shifted towards the minimum U^{i}_{MOR} area. In contrast, metals lying on the lower left part are shifted further away from the minimum. The volcano plot of Fig. 2 stands as a pictorial description of size effects in methanol electro-oxidation catalysis, assuming that catalytic particles will show an increasing number of steps with decreasing size. However, a detailed investigation of particle size effects is out of the scope of the current study.

We have used a pair of adsorption energies as descriptors, i.e. ΔG_{CO} together with ΔG_{OH}, for the construction of the volcano plot. This is feasible only because a correlation exists between the adsorption energy of any of the MOR intermediates and ΔG_{CO} or ΔG_{OH} (Fig. 3). The existence of correlations between the binding energies of the intermediates of different catalytic reactions (including the MOR) is well established in the literature [28,23,29,49]. As shown in Fig. 3 the adsorption energies of all the MOR intermediates binding through a O atom to the surface scale linearly with ΔG_{OH} whereas for species which bind through a C atom, the respective binding energies show a linear relationship with ΔG_{CO}. The stronger OH and CO bind to the surface, the stronger the binding of the other MOR intermediates is. The scaling relationships offer only an approximate description of the identified correlations. This reduces the reliability of the study of any surface in isolation. When discussing trends over the whole set of surfaces considered here, the error in the approximations becomes of secondary importance due to the large range of values ΔG_{CO} and ΔG_{OH} assume (~2.5eV). These linear relationships allow for the overpotential to be estimated for every point of the descriptors phase space. The

potential $U^{\dagger}_{\mathrm{MOR}}$ is calculated as = max(U_{CO}, U_{OH}, $U_{\mathrm{CO_2}}$) with $eU_{\mathrm{OH}} = \Delta G_{\mathrm{OH}}$ and $eU_{\mathrm{CO_2}} = -\left(\Delta G_{\mathrm{OH}} + \Delta G_{\mathrm{CO}}\right)$. The potential U_{CO} is calculated as the maximum free energy difference between every two successive elementary steps of the reaction 2a after the reaction mechanism is constructed for a pair of $\left(\Delta G_{\mathrm{CO}}, \Delta G_{\mathrm{OH}}\right)$ values using the established linear relationships. Since both steps and terraces are found to share the same scaling relationships, a common volcano plot such as the one shown in Fig. 2 can be constructed.

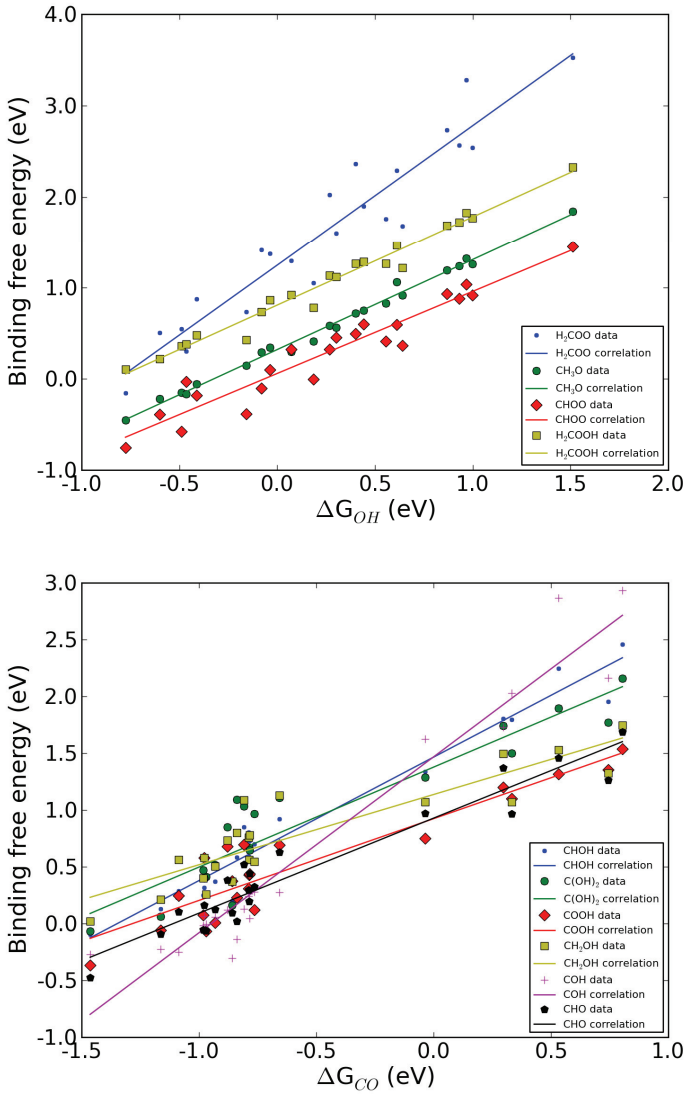

Fig. 3 Adsorption free energies of methanol oxidation reaction intermediates are found to scale linearly with the adsorption energy of either OH (left) or CO (right), for O- or C-bound species, respectively. Since both stepped and flat surfaces share the same scaling relationships, a common pair of microscopic descriptors, i.e. the adsorption energy of OH and CO, is used for the estimation of the relative reactivity.

To this point, we have demonstrated the existence of a global minimum for U^{i}_{MOR} on monometallic, stepped or flat, surfaces which is significantly above the thermodynamic value. Still, a way one can achieve lower overpotentials is by exploiting bi-functionality and ligand effects in bimetallic alloy structures [11]. Prominent examples include PtRu [4,3,8,50], the most commercially successful DMFC anode catalyst, and PtSn [3,51] both of which show enhanced activity compared to the constituent metals alone. The oxidation of methanol to CO requires low potentials on Pt but the latter's inefficiency in further oxidizing CO to CO_2 limits the overall activity. On the other hand, Ru or Sn easily activate water in a way that a PtRu or a PtSn alloy brings together the best of two worlds.

We test the applicability of our methodology to the study of bimetallic alloys: if the volcano plot can also accommodate such structures then elemental and bimetallic surfaces can all be studied under a common framework. Since the volcano plot is constructed from linear relationships extracted from a set of monometallic metal surfaces only, it is first ensured that bimetallic alloys can also be accommodated on it. We construct two model surfaces, one for the PtRu and one for the PtSn alloy and see how they fit on the volcano plot. We model PtRu as Ru slab with a 3/4ML skin of Pt on a Ru hcp(0001) surface (Pt_3Ru/Ru, Fig. 4a) and PtSn as a $L1_2$(111) surface (Pt_3Sn, Fig. 4b) according to the work of Liu et al. [52] and we calculate the pair of the $\left(\Delta G_{\mathrm{CO}}, \Delta G_{\mathrm{OH}}\right)$ descriptors for each alloy.

Both alloys appear exactly on the border between two different PDS regions where water is activated as easily as methanol is oxidized to CO (Fig. 5). In other words, both alloys are found to simultaneously satisfy two of the three conditions for an efficient MOR catalyst although OH and CO still bind unfavorably weakly. Quantitative one-to-one comparison between experimentally measured activities and a theoretical estimation based on scaling relationships can be problematic. Still, our model is in qualitative agreement with what is reported in the literature, i.e. the improvement of the performance of these alloys over monometallic surfaces. This allows us to use the same volcano plot as a common platform for the study of both monometallic and bimetallic catalysts together. An implication of this fact is that bimetallic electro-catalysts are also susceptible to a global maximum in activity (minimum in overpotential). On the other hand, an alloy introduces more degrees of freedom in the design process. The increased flexibility in tuning $\left(\Delta G_{\mathrm{CO}}, \Delta G_{\mathrm{OH}}\right)$ facilitates the exploration of the phase space and, thus, the process of optimizing the catalytic performance.

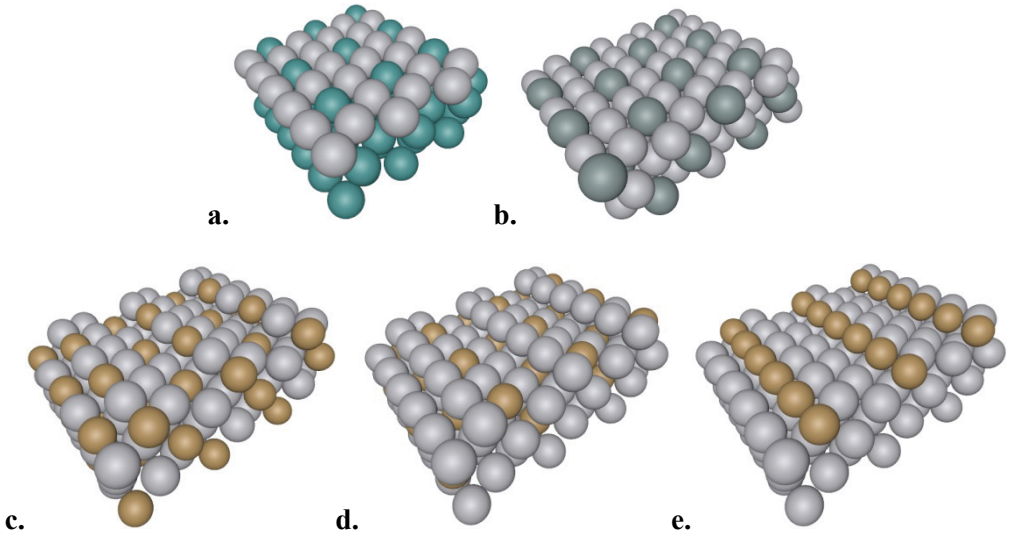

Fig. 4 Model surfaces of a) Pt_3Ru/Ru fcc(111), b) Pt_3Sn $L1_2$(111), c) Pt_3Cu $L1_2$(211)-AB, d) Pt_3Cu $L1_2$(211)-BB and e) Pt_2Cu/Pt fcc(211) alloys.

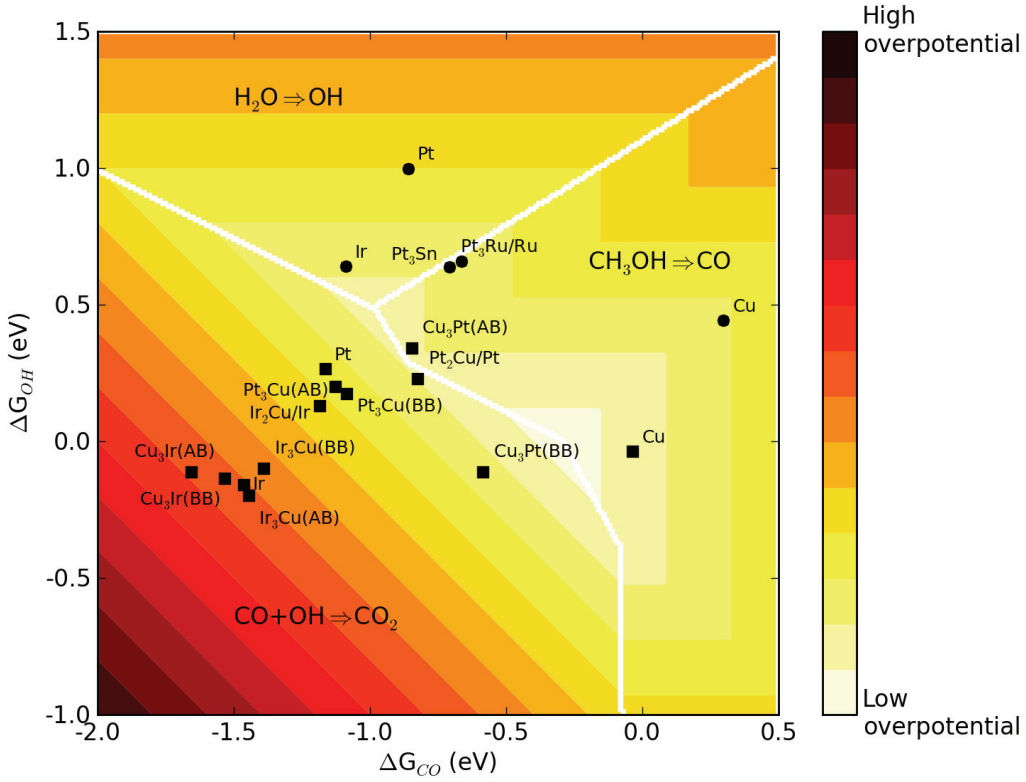

Fig. 5 Volcano plot for the indirect mechanism with stepped (squares) and flat (circles) elemental surfaces and bimetallic alloys. The reference structures Ru_3Pt/Ru and Pt_3Sn are located exactly on the border where the potential for water activation and oxidation of methanol to CO become equal to each other hinting a qualitative

difference from monometallic surfaces towards more efficient catalysis. When screening for bimetallic catalysts we find the PtCu alloys to show promising catalytic performance.

Next, we estimate the MOR overpotential of a bimetallic catalyst by only considering the adsorption free energies of the MOR intermediates on monometallic surfaces of the constituent elements alone. Different assumptions can be made about the mobility of OH and CO on the surface of the catalyst [13,50]. By assuming both to be adequately mobile, we estimate the potential U^{i}_{MOR} for a bi-functional catalyst AB as $U^{\mathrm{i}}_{\mathrm{MOR}} = \min\left(\max\left(U^{\mathrm{A}}_{\mathrm{CO}}, U^{\mathrm{B}}_{\mathrm{OH}}, U^{\mathrm{min}}_{\mathrm{CO_2}}\right), \max\left(U^{\mathrm{B}}_{\mathrm{CO}}, U^{\mathrm{A}}_{\mathrm{OH}}, U^{\mathrm{min}}_{\mathrm{CO_2}}\right)\right)$ with $eU^{\mathrm{min}}_{\mathrm{CO_2}} = \min\left(-\Delta G^{\mathrm{A}}_{\mathrm{OH}}, -\Delta G^{\mathrm{B}}_{\mathrm{OH}}\right) + \min\left(-\Delta G^{\mathrm{A}}_{\mathrm{CO}}, -\Delta G^{\mathrm{B}}_{\mathrm{CO}}\right)$. The superscripts 'A' and 'B' denote the surface on which each potential or adsorption free energy was initially calculated. As a specific example, we estimate the potential U^{i}_{MOR} for an alloy of Pt and Ru to be 0.33V, calculated as $U^{\mathrm{i}}_{\mathrm{MOR}} = \max\left(U^{\mathrm{Pt_t}}_{\mathrm{CO}}, U^{\mathrm{Ru_s}}_{\mathrm{OH}}, -\left(\Delta G^{\mathrm{Pt_t}}_{\mathrm{OH}} + \Delta G^{\mathrm{Pt_t}}_{\mathrm{CO}}\right)\right)$ where a Pt terrace (denoted by subscript 't') oxidizes methanol to CO and a Ru step (denoted by subscript 's') activates water (see also Table S4). OH is assumed to migrate from Ru to Pt before reacting with CO. We find the PDS to be the initial methanol dehydrogenation on Pt. Both the calculated potential and the PDS are indeed found in agreement with experiments [3,50].

We now proceed to screen all possible combinations of two transition metal surfaces for favorable reactivity. We calculate U^{i}_{MOR} for each combination and the performance of all the resulting bi-functional surfaces are tested against the following criteria:

1. The potential U^{i}_{MOR} of the bi-functional surface must be less than this of each of the constituent elemental surfaces.
2. As a measure of surface stability against dissolution and oxidation effects, U^{i}_{MOR} should be less than the standard reduction potential [53] of both the two constituent pure metals. Although the reduction potential is dependent on the detailed geometry of a surface, we use the values for the bulk as an approximation. Moreover, the sum $\Delta G_{\mathrm{CO}} + \Delta G_{\mathrm{O}}$ which corresponds to the CO+O state with the lowest energy should be higher than $\Delta G_{\mathrm{CO_2(g)}} = 0$ to ensure resistance to surface poisoning from O.

3. The absolute difference in ΔG_{CO} or ΔG_{OH} between the two surfaces should be less than 1.0eV for CO and OH to be considered adequately mobile.

The top 20 alloys of favorable performance are presented in Fig. 6.

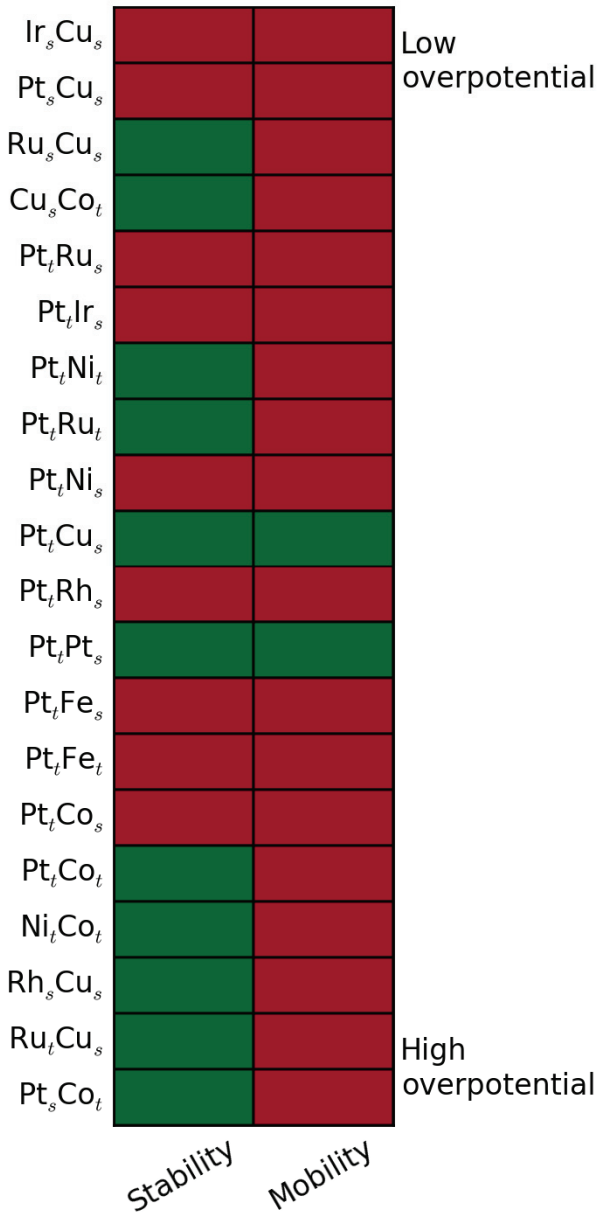

Fig. 6 Results of the screening process of bi-functional methanol oxidation catalysts. The subscripts signify a terrace ('t') or a step ('s'). Each alloy is screened for stability and adequate mobility of CO and OH. Any of these two criteria is marked with green if successfully satisfied or red if otherwise.

Returning to the case of the PtRu alloy, two different combinations of Pt and Ru surfaces are included in the list. A combination of terraces and a combination of Ru steps with Pt terraces. Although the two alloys are calculated to show low overpotential, the screening points at stability issues. During the screening we implicitly ignored any ligand effects. The energetics of each metal are assumed to remain unaffected by the presence of the other. Experiments show that such electronic effects are present in the case of PtRu [47,54]. By comparing with experiment, the screening procedure helps in decomposing the alloying effect into two components, a bi-functionality effect and a ligand effect.

The bi-functionality effect is not relevant only to combinations of different metals. It also manifests itself on monometallic surfaces by considering the presence of both steps and terraces, a picture closer to the morphology of real catalytic nanoparticles. Indeed, a combination of a Pt step with a Pt terrace is calculated to show lower U^{i}_{MOR} (~0.30V) compared to a single stepped or flat surface. Steps will facilitate the activation of water while CO is formed on the terrace. The final step of CO oxidation is assumed to take place on the flat surface. This result comes to complement the observation of Housmans et al. [55] of a favorable "ensemble site" of a step and a terrace for methanol decomposition. The most active bi-functional alloy which complies with all the requirements of the filtering process is PtCu. Water is activated on Cu steps and CO is provided by Pt terraces. CO_2 is then formed on Pt.

Ir when alloyed with Pt is known to act as a promoter for the MOR [56]. The latter observation is supported by the screening process as a PtIr surface is found among the alloys with the lowest overpotential. Other catalysts of favorable performance shown in Fig. 6 include the PtNi and PtCo alloys. These catalysts have already been the subject of previous experimental studies which attribute the catalytic efficiency to reduced CO poisoning [21,57]. PtRh is yet another candidate that is discussed in the literature [58]. In this case, experiments show that the bi-functionality mechanism switches off by poisoning of the surface, as the screening also suggests.

The physical meaning behind a 'combination of terraces' or a 'combination of terraces and steps' must be treated with caution. A terrace or step here indicates which feature of the alloy surface contributes mainly to the MOR mechanism. A stepped surface serves as a model for surface defects. A combination of two terraces or two steps may be applicable to a phase separated or ordered alloy. A step and terrace combination could correspond to the situation of clusters of one metal supported by the terrace of the second metal or a crystallographic defect on a flat

surface. Moreover, we made no assumption which excludes the rise of a bi-functionality effect from the exchange of adsorbates between closely situated nanoparticles [34].

Two general remarks follow:

1. Fig. 6 shows how surface irregularities give rise to bi-functionallity [55]. Most of the alloys presented include steps, a supportive argument for the importance of considering steps (or defects for that matter) in an attempt for modeling MOR catalysts.
2. Pt is a component in both two alloys that successfully fulfill all the requirements of the screening process while any non-noble catalyst is flagged as possibly unstable. Stabilization of the catalyst surface against the hostile electrochemical environment of the DMFC through ligand effects is suggested to be a requisite if the complete replacement of Pt is desired.

The screening process is based on an approximate estimation of the overpontential. The success of a theoretical screening process depends on the careful choice of model surfaces and assumptions. The good qualitative agreement between our findings and experiments, reinforces the validity of our methodology in its entirety. Identified promising alloys are examined more thoroughly by performing additional calculations to validate the initial screening and further investigate issues such as the actual geometry of the surface and its stoichiometry.

We do so for the two alloys with the lowest estimated overpotential, i.e. Ir_sCu_s and Pt_sCu_s. Since both combinations include only steps we chose to model the alloy surfaces also as steps. More specifically, we construct model $L1_2(211)$ surfaces of the Cu_3Ir, Ir_3Cu, Cu_3Pt and Pt_3Cu alloys for two different step configurations (we use the notation 'AB' and 'BB' to distinguish between them) as well as two fcc(211) Pt and Ir slabs, Pt_2Cu/Pt and Ir_2Cu/Ir respectively, where the step atoms were substituted with Cu (Fig. 4c-e). The alloys are then positioned on the volcano plot of Fig. 5 after calculating the strength of CO and OH binding on each surface.

Quick inspection of the volcano eliminates from the list of promising candidates all the IrCu alloys but Ir_2Cu/Ir. Both of CO and OH bind strongly bind on Ir. Ir_2Cu/Ir performs comparably better since the substitution of the step Ir atoms with Cu eliminates any strongly binding sites but still its reactivity is far from optimal and what the initial screening suggested.

PtCu alloys show overall much more promising reactivity than the IrCu alloys, especially $Cu_3Pt(AB)$ and Pt_2Cu/Pt. Encouraged by this fact, we proceed to evaluate their stability. We calculate the energy barrier

associated with atomic diffusion by swapping Pt atoms with nearest neighbor Cu atoms (see also supporting information). We find such processes energetically unfavorable in all cases. CO adsorption induced segregation is found to be potentially an issue for the Pt_2Cu/Pt surface. We thus focus only on the Cu_3Pt(AB) alloy.

We look into the MOR on the Cu_3Pt(AB) surface in more detail after calculating a complete set of adsorption free energies of the reaction intermediates. We calcualte the potentials relevant to each reaction step of Eqn. 2 together with the potentials U_{MOR} for the direct and indirect mechanism(Table 2, see also supporting information Fig. S3 for a constructed reaction free energy diagram).

Surface	U_{CO} (V)	U_{OH} (V)	U_{CO_2} (V)	U^{i}_{MOR} (V)	U^{d}_{MOR} (V)
Cu_3Pt(AB)	0.47	0.34	0.51	0.51	0.47

Table 2 Potentials relevant to the direct and indirect mechanism for the Cu_3Pt(AB) alloy.

By a quick comparison between Tables 1 and 2 we see that these stepped PtCu alloy surfaces show a potential U^{i}_{MOR} which is lower than that of almost any other monometallic catalyst. The PDS is identified to be the final oxidation of CO to CO_2. Interestingly, PtCu electrocatalysts have already been identified to show favorable activity as PEM fuel cell cathode catalysts for the oxygen reduction reaction (ORR) in the form of de-alloyed nanoparticles [59,60]. Controlled dissolution of the non-noble element from a Pt-containing bimetallic alloy leads to activity enhancement by induced compressive strain [61,62]. Dissolution of Cu from a PtCu alloy surface results in a lattice-contracted Pt-rich surface with a substantial amount of irregularities. Reducing the lattice constant of a Pt stepped surface destabilizes the reaction intermediates as the d-band model suggests, shifting the surface up and right on the volcano plot of Fig. 5 towards lower overpotentials. As a consequence, our findings support the experimental observation that PtCu catalysts are susceptible to methanol cross-over effects as much as Pt is [59]. The exact ratio between the MOR and ORR activities is in general dependent on the specifics of the nanoparticle's morphology [63].

Starting from a database of DFT calculated adsorption energies of MOR intermediates on monometallic surfaces we followed a well-defined sequence of steps which led to the identification of at least one alloy of promising catalytic properties. We summarize these steps below:

1) A primary screening identifies alloys of possibly low MOR overpotential with the use of a bi-functionality model. The most promising candidate alloys are then selected for a secondary screening for which appropriate model surfaces are constructed.
2) After showing that monometallic and bimetallic surfaces can be accommodated on the same volcano plot, we calculate the strength of CO and OH binding on each surface and we check with volcano plot for favorable reactivity.
3) If the surface proves to be promising on the basis of the calculated reactivity descriptors, the stability of the surface is evaluated against oxidation and dissolution effects.
4) Finally, a complete set of DFT calculations is performed to get a more accurate insight into the reaction mechanism and a more accurate estimation for the overpotential.

While searching for MOR catalysts of improved catalytic performance, we have gone through a complete design cycle:

1) We started the search for highly active MOR catalysts from evaluating the catalytic performance of a set of materials, i.e. monometallic flat and stepped transition metal surfaces, after constructing appropriate model surfaces. We extracted trends in their reactivity and identified suitable descriptors of it.
2) The need for more degrees of freedom in the design process led us to screen a second generation of catalysts, i.e. bi-functional alloys the performance of which we evaluated by checking against experimental studies. We then constructed model surfaces to investigate the MOR in more depth for selected alloys, singled out by the screening mechanism.

One may then enter a new cycle where the already acquired insight is refined and used to screen a new generation of materials for even higher performance. One may, for example, proceed with enlarging the study set to ternary and quaternary alloys. Since only two alloys were studied in more detail after the screening -only as a proof of concept- a detailed investigation of a more complete set of structures should precede any subsequent step.

Conclusions

A common framework was introduced for the study of MOR which we used to evaluate the catalytic performance of monometallic and bimetallic transition metal model surfaces, flat and stepped, including overlayer structures and modified edges. Under a unified methodology, a theoretical design cycle was followed in the search for

effective DMFC anode catalysts. In the process, we showed how bi-functionality effects can be exploited for the identification of bimetallic alloys of enhanced performance. By employing a screening mechanism we narrowed the initial number of candidate catalysts down to a few promising ones which we further investigated following a well defined sequence of steps singling out PtCu alloy surfaces as promising electro-catalysts.

In the same time, we have demonstrated the importance of modeling low-coordinated surface sites (here as stepped surfaces) as a means for bridging the structure gap between single crystal surfaces and realistic nanoparticles, where size effects emerge from the increase in the number of defects. The improved fundamental understanding of defect effects also comes to provide directions for the design of shape-controlled catalytic nanoparticles [64,65]: By controlling the ratio of low-coordinated surface sites over well-ordered domains in a rational way, the energetics of transition metal surfaces can be tuned towards enhanced MOR catalytic activity.

Acknowledgements

CAMD (Center for Atomic-scale Materials Design) is funded by the Lundbeck Foundation. This work was supported by the Danish Center for Scientific Computing.

References

[1] C. Lamy, A. Lima, V. LeRhun, F. Delime, C. Coutanceau, and J. Léger, Journal of Power Sources **105**, 283-296 (2002).
[2] A. S. Aricò, S. Srinivasan, and V. Antonucci, Fuel Cells **1**, 133-161 (2001).
[3] S. Wasmus and A. Küver, Journal of Electroanalytical Chemistry **461**, 14-31 (1999).
[4] T. Iwasita, Electrochimica Acta **47**, 3663-3674 (2002).
[5] H. Liu, C. Song, L. Zhang, J. Zhang, H. Wang, and D. P. Wilkinson, Journal of Power Sources **155**, 95-110 (2006).
[6] B. Hammer, O. Nielsen, and J. Nørskov, Catalysis Letters **46**, 31-35 (1997).
[7] H. A. Gasteiger and N. M. Marković, Science **324**, 48-49 (2009).
[8] J. Kua and W. Goddard III, Journal of the American Chemical Society **121**, 10928-10941 (1999).
[9] A. Lima, C. Coutanceau, J. LÉger, and C. Lamy, Journal of Applied Electrochemistry **31**, 379-386 (2001).
[10] P. Strasser, Q. Fan, M. Devenney, W. Weinberg, P. Liu, and J. Nørskov, Journal of Physical Chemistry B **107**, 11013-11021 (2003).
[11] B. Gurau, R. Viswanathan, R. Liu, T. Lafrenz, K. Ley, E. Smotkin, E. Reddington, A. Sapienza, B. Chan, T. Mallouk, and S. Sarangapani, Journal of Physical Chemistry B **102**, 9997-10003 (1998).
[12] J. Solla-Gullón, F. Vidal-Iglesias, A. López-Cudero, E. Garnier, J. Feliu, and A. Aldaz, Physical Chemistry Chemical Physics **10**, 3689-3698 (2008).
[13] N. Lebedeva, M. Koper, J. Feliu, and R. Van Santen, Journal of Physical Chemistry B **106**, 12938-12947 (2002).

[14] S. W. Lee, S. Chen, W. Sheng, N. Yabuuchi, Y. Kim, T. Mitani, E. Vescovo, and Y. Shao-Horn, Journal of the American Chemical Society **131**, 15669-15677 (2009).
[15] H. A. Gasteiger, S. S. Kocha, B. Sompalli, and F. T. Wagner, Applied Catalysis B: Environmental **56**, 9-35 (2005).
[16] A. Hamnett, Catalysis Today **38**, 445-457 (1997).
[17] M. Neurock, M. Janik, and A. Wieckowski, Faraday Discussions **140**, 363-378 (2008).
[18] E. Batista, G. Malpass, A. Motheo, and T. Iwasita, Journal of Electroanalytical Chemistry **571**, 273-282 (2004).
[19] V. Bagotzky, Y. Vassiliev, and O. Khazova, Journal of Electroanalytical Chemistry **81**, 229-238 (1977).
[20] Y. Okamoto, O. Sugino, Y. Mochizuki, T. Ikeshoji, and Y. Morikawa, Chemical Physics Letters **377**, 236-242 (2003).
[21] J. Spendelow and A. Wieckowski, Physical Chemistry Chemical Physics **6**, 5094-5118 (2004).
[22] T. D. Jarvi, S. Sriramulu, and E. M. Stuve, Colloids and Surfaces A: Physicochemical and Engineering Aspects **134**, 145-153 (1998).
[23] P. Ferrin, A. U. Nilekar, J. Greeley, M. Mavrikakis, and J. Rossmeisl, Surface Science **602**, 3424-3431 (2008).
[24] E. Skúlason, G. S. Karlberg, J. Rossmeisl, T. Bligaard, J. Greeley, H. Jónsson, and J. K. Nørskov, Phys. Chem. Chem. Phys. **9**, 3241-3250 (2007).
[25] J. K. Nørskov, J. Rossmeisl, A. Logadottir, L. Lindqvist, J. R. Kitchin, T. Bligaard, and H. Jónsson, The Journal of Physical Chemistry B **108**, 17886-17892 (2004).
[26] S. K. Desai, M. Neurock, and K. Kourtakis, The Journal of Physical Chemistry B **106**, 2559-2568 (2002).
[27] C. Hartnig and E. Spohr, Chemical Physics **319**, 185-191 (2005).
[28] F. Abild-Pedersen, Phys. Rev. Lett. **99**, (2007).
[29] B. Hammer and J. Nørskov, Advances in Catalysis **45**, 71 (2000).
[30] T. H. M. Housmans and M. T. M. Koper, The Journal of Physical Chemistry B **107**, 8557-8567 (2003).
[31] A. Kuzume, E. Herrero, and J. Feliu, Journal of Electroanalytical Chemistry **599**, 333-343 (2007).
[32] J. Yates Jr., Journal of Vacuum Science and Technology A: Vacuum, Surfaces and Films **13**, 1359-1367 (1995).
[33] L. Vattuone, L. Savio, and M. Rocca, Surface Science Reports **63**, 101-168 (2008).
[34] K. Bergamaski, A. Pinheiro, E. Teixeira-Neto, and F. Nart, Journal of Physical Chemistry B **110**, 19271-19279 (2006).
[35] C. Burda, X. Chen, R. Narayanan, and M. El-Sayed, Chemical Reviews **105**, 1025-1102 (2005).
[36] S. Park, Y. Xie, and M. Weaver, Langmuir **18**, 5792-5798 (2002).
[37] K. Kinoshita, Journal of the Electrochemical Society **137**, 845-848 (1990).
[38] P. E. Blöchl, Phys. Rev. B **50**, 17953 (1994).
[39] J. J. Mortensen, L. B. Hansen, and K. W. Jacobsen, Phys. Rev. B **71**, 035109 (2005).
[40] J. Enkovaara, C. Rostgaard, J. Mortensen, J. Chen, M. Dułak, L. Ferrighi, J. Gavnholt, C. Glinsvad, V. Haikola, H. Hansen, H. Kristoffersen, M. Kuisma, A. Larsen, L. Lehtovaara, M. Ljungberg, O. Lopez-Acevedo, P. Moses, J. Ojanen, T. Olsen, V. Petzold, N. Romero, J. Stausholm-Møller, M. Strange, G. Tritsaris, M. Vanin, M. Walter, B. Hammer, H. Häkkinen, G. Madsen, R. Nieminen, J. Nørskov, M. Puska, T. Rantala, J. Schiøtz, K. Thygesen, and K. Jacobsen, Journal of Physics Condensed Matter **22**, (2010).
[41] B. Hammer, L. B. Hansen, and J. K. Nørskov, Phys. Rev. B **59**, 7413 (1999).
[42] A. Peterson, F. Abild-Pedersen, F. Studt, J. Rossmeisl, and J. Nørskov, Energy and Environmental Science **3**, 1311-1315 (2010).
[43] D. Cao, G. Lu, A. Wieckowski, S. A. Wasileski, and M. Neurock, The Journal of Physical Chemistry B **109**, 11622-11633 (2005).

[44] E. Herrero, W. Chrzanowski, and A. Wieckowski, The Journal of Physical Chemistry **99**, 10423-10424 (1995).
[45] P. Ferrin and M. Mavrikakis, Journal of the American Chemical Society **131**, 14381-14389 (2009).
[46] V. Stamenkovic, B. S. Mun, K. J. Mayrhofer, P. N. Ross, N. M. Markovic, J. Rossmeisl, J. Greeley, and J. K. Nørskov, Angewandte Chemie International Edition **45**, 2897-2901 (2006).
[47] M. T. M. Koper, T. E. Shubina, and R. A. van Santen, The Journal of Physical Chemistry B **106**, 686-692 (2002).
[48] N. P. Lebedeva, M. T. M. Koper, E. Herrero, J. M. Feliu, and R. A. van Santen, Journal of Electroanalytical Chemistry **487**, 37-44 (2000).
[49] J. K. Nørskov, J. Rossmeisl, A. Logadottir, L. Lindqvist, J. R. Kitchin, T. Bligaard, and H. Jónsson, The Journal of Physical Chemistry B **108**, 17886-17892 (2004).
[50] H. A. Gasteiger, N. Markovic, P. N. Ross, and E. J. Cairns, The Journal of Physical Chemistry **97**, 12020-12029 (1993).
[51] W. Zhou, Z. Zhou, S. Song, W. Li, G. Sun, P. Tsiakaras, and Q. Xin, Applied Catalysis B: Environmental **46**, 273-285 (2003).
[52] P. Liu, A. Logadottir, and J. K. Nørskov, Electrochimica Acta **48**, 3731-3742 (2003).
[53] *CRC Handbook of Chemistry and Physics* (CRC Press, New York, 1996).
[54] P. Liu and J. K. Nørskov, Fuel Cells **1**, 192-201 (2001).
[55] T. Housmans, A. Wonders, and M. Koper, Journal of Physical Chemistry B **110**, 10021-10031 (2006).
[56] A. Hamnett and B. Kennedy, Electrochimica Acta **33**, 1613-1618 (1988).
[57] D. Stevens, J. Rouleau, R. Mar, A. Bonakdarpour, R. Atanasoski, A. Schmoeckel, M. Debe, and J. Dahn, Journal of the Electrochemical Society **154**, (2007).
[58] W. Tokarz, H. Siwek, P. Piela, and A. Czerwiński, Electrochimica Acta **52**, 5565-5573 (2007).
[59] E. Antolini, T. Lopes, and E. Gonzalez, Journal of Alloys and Compounds **461**, 253-262 (2008).
[60] S. Koh and P. Strasser, Journal of the American Chemical Society **129**, 12624-12625 (2007).
[61] M. Watanabe, K. Tsurumi, T. Mizukami, T. Nakamura, and P. Stonehart, Journal of the Electrochemical Society **141**, 2659-2668 (1994).
[62] V. R. Stamenkovic, B. S. Mun, M. Arenz, K. J. J. Mayrhofer, C. A. Lucas, G. Wang, P. N. Ross, and N. M. Markovic, Nat Mater **6**, 241-247 (2007).
[63] F. Maillard, M. Martin, F. Gloaguen, and J. Léger, Electrochimica Acta **47**, 3431-3440 (2002).
[64] N. Tian, Z. Zhou, S. Sun, Y. Ding, and Z. L. Wang, Science **316**, 732-735 (2007).
[65] S. Han, Y. Song, J. Lee, J. Kim, and K. Park, Electrochemistry Communications **10**, 1044-1047 (2008).

Methanol electro-oxidation catalysis on elemental and bimetallic transition metals surfaces

G. A. Tritsaris, J. Rossmeisl

Department of Physics, Center for Atomic-scale Materials Design,

Technical University of Denmark, DK-2800 Lyngby, Denmark

Supporting information includes a database of DFT calculated adsorption free energies of methanol oxidation reaction (MOR) intermediates, a short discussion on the estimation of the effect of water on the adsorption of the intermediates, the potentials used for the screening of bi-functional surfaces, a list of expressions describing the linear relationships of Fig. 3, lattice constants of the bulk alloys screened, more information on estimating atomic diffusion effects relevant to the bimetallic model surfaces and finally, free energy diagrams for the MOR over the Cu_3Pt alloy.

Database of adsorption energies

A database of adsorption free energies of 13 MOR intermediate species was established on the basis of DFT calculations for the study of the MOR over 22 different monometallic model surfaces (Table S1).

	O	H_2COO	H_2COOH	CO	OH	CHOH	$C(OH)_2$	CHO	CHOO	COOH	COH	CH_2OH	CH_3O
Ag_s	2.09	2.29	1.47	0.53	0.61	2.24	1.89	1.46	0.60	1.32	2.87	1.53	1.06
Ag_t	2.26	2.73	1.69	0.80	0.87	2.46	2.16	1.69	0.93	1.54	2.93	1.74	1.19
Au_s	2.52	3.28	1.83	0.33	0.97	1.80	1.50	0.97	1.04	1.10	2.03	1.07	1.33
Au_t	2.65	3.53	2.33	0.74	1.51	1.96	1.77	1.26	1.45	1.35	2.16	1.33	1.84
Co_s	-0.27	0.50	0.22	-0.79	-0.60	0.59	0.67	0.20	-0.39	0.43	0.26	0.56	-0.22
Co_t	0.10	1.30	0.92	-0.66	0.07	0.92	1.11	0.63	0.32	0.69	0.27	1.13	0.30
Cu_s	0.85	1.38	0.86	-0.04	-0.04	1.34	1.29	0.97	0.10	0.75	1.62	1.07	0.34
Cu_t	1.08	1.90	1.29	0.30	0.44	1.81	1.74	1.37	0.60	1.20	1.73	1.50	0.75
Fe_s	-0.76	-0.15	0.10	-0.76	-0.78	0.72	0.97	0.32	-0.76	0.12	0.28	0.55	-0.46
Fe_t	-0.57	0.30	0.38	-0.84	-0.47	0.58	1.09	0.02	-0.03	0.23	-0.14	0.80	-0.17
Ir_s	0.21	0.73	0.43	-1.46	-0.16	-0.10	-0.07	-0.48	-0.39	-0.37	-0.27	0.02	0.15
Ir_t	0.86	1.68	1.22	-1.09	0.64	0.29	0.24	0.10	0.37	0.25	-0.25	0.56	0.92
Ni_s	0.10	0.88	0.48	-0.93	-0.41	0.37	0.51	0.12	-0.18	0.01	0.06	0.50	-0.06
Ni_t	0.35	1.61	1.12	-0.81	0.30	0.85	1.03	0.52	0.45	0.70	0.13	1.09	0.56
Pd_s	1.47	2.36	1.27	-0.98	0.40	0.32	0.40	0.16	0.49	0.58	0.07	0.58	0.72
Pd_t	1.46	2.57	1.72	-0.88	0.93	0.67	0.85	0.38	0.88	0.68	0.12	0.74	1.24
Pt_s	1.14	2.02	1.13	-1.16	0.27	0.13	0.06	-0.09	0.32	-0.06	-0.23	0.21	0.58
Pt_t	1.46	2.54	1.77	-0.86	1.00	0.20	0.16	0.10	0.92	0.37	-0.31	0.37	1.26
Rh_s	0.64	1.42	0.73	-0.98	-0.08	0.25	0.47	-0.05	-0.10	0.08	-0.02	0.40	0.29
Rh_t	0.86	1.76	1.27	-0.78	0.56	0.73	0.65	0.44	0.41	0.44	0.05	0.78	0.83
Ru_s	-0.04	0.55	0.36	-0.97	-0.49	0.24	0.41	-0.06	-0.58	-0.07	-0.00	0.26	-0.15
Ru_t	0.22	1.05	0.78	-0.79	0.19	0.81	0.77	0.30	-0.00	0.31	0.24	0.76	0.41

Table S1 Most stable site adsorption energies are reported (in eV) for a coverage of 1/4ML and 1/6ML for flat (denoted by the subscript 't') and stepped surfaces ('s') surfaces.

All energies reported in Table S1 are given with reference to the gas-phase energy of H_2O, H_2 and CO_2 after corrected as discussed in the main article. The (corrected) total energy of the reference molecules is calculated as $\Delta E_{H_2O(g)}$ = -14.02eV, $\Delta E_{H_{2(g)}}$ = -6.72eV and $\Delta E_{CO_{2(g)}}$ = -22.19eV respectively. For the intermediates CH_2O and HCOOH, both of which are closed-shell molecules, the (corrected) gas-phase energy was used: $\Delta G_{HCOOH(g)}$ = 0.50eV, $\Delta G_{CH_2O(g)}$ = 0.40eV. For gas-phase methanol the free energy is calculated $\Delta G_{CH_3OH(g)}$ = 0.04eV. For the screening of bimetallic alloys a new set of adsorption free energies was calculated, reported in Table S2.

	O	H_2COO	H_2COOH	CO	OH	CHOH	$C(OH)_2$	CHO	CHOO	COOH	COH	CH_2OH	CH_3O
Ru_3P/Ru				-0.71	0.64								
Pt_3Sn				-0.66	0.66								
$Cu_3Ir(AB)$				-1.66	-0.11								
$Cu_3Ir(BB)$				-1.53	-0.14								
$Ir_3Cu(AB)$				-1.45	-0.20								
$Ir_3Cu(BB)$				-1.39	-0.10								
Ir_2Cu/Ir				-1.19	0.13								
$Cu_3Pt(AB)$	1.19	1.85	1.27	-0.85	0.34	0.63	0.59	0.20	0.55	0.36	0.66	0.51	0.75
$Cu_3Pt(BB)$				-0.59	-0.11								
$Pt_3Cu(AB)$				-1.13	0.20								
$Pt_3Cu(BB)$				-1.09	0.18								
Pt_2Cu/Pt				-0.82	0.23								

Table S2 Most stable site adsorption energies are reported (in eV).

Water effect on adsorption energies

We correct the adsorption energies of all R-OH species and OH by -0.15eV and -0.25eV respectively. The correction for OH is calculated from the difference between the adsorption energy $\Delta G_{OH/H_2O}$ of a 1/3ML of OH embedded in a half-dissociated layer of water and the adsorption energy ΔG_{OH} of 1/4ML of OH binding through the most stable binding site on a clean surface, averaged over 13 different closed-packed surfaces. All the surfaces were modeled as (2x2) or (2x3) (for clean or water-covered surfaces) 4-layer slabs.

	Ag	Au	Co	Cu	Fe	Ir	Mo	Ni	Pd	Pt	Rh	Ru	W
ΔG_{OH}	0.79	1.41	-0.07	0.39	-0.54	0.76	-0.76	0.15	0.87	1.04	0.45	0.11	-0.57
$\Delta G_{OH/H2O}$	0.75	1.21	0.04	0.36	-0.41	0.10	-1.05	0.21	0.60	0.64	0.06	-0.34	-1.11
Δ (ΔG)	-0.03	-0.20	0.11	-0.03	0.13	-0.66	-0.28	0.06	-0.26	-0.40	-0.39	-0.44	-0.53

Table S3 Adsorption energy ΔG_{OH} of OH on clean surfaces (most stable binding site energy is reported) and $\Delta G_{OH/H_2O}$ of OH embedded in a half-dissociated monolayer of water (on top site).

For R-OH the correction was calculated for a Pt fcc(111) surface from the difference in adsorption energy between a 1/6ML of CH_2OH embedded in the water layer and a 1/3ML on a clean surface. The correction was then applied to the adsorption energies of the following species: CH_2OH, COH, COOH, H_2COOH, $C(OH)_2$, and CHOH.

Potentials for the indirect mechanism

Focusing on the indirect pathway, the potentials corresponding to a) methanol oxidation to CO (U_{CO}), b) water activation to form OH (U_{OH}) and c) formation of CO_2 from CO and OH (U_{CO_2}) is all the data used for the estimation of the potential U^{i}_{MOR} of all the bi-functional materials screened. The minimum of each of the potentials between the two respective monometallic surfaces is collected separately and the highest of the final three is used for estimating the overpotential of the bimetallic surface. A negative potential corresponds to a spontaneous process.

	U_{CO}	U_{OH}	U_{CO_2}		U_{CO}	U_{OH}	U_{CO_2}
Ag_s	1.05	0.61	-1.14	Ni_s	0.46	-0.41	1.34
Ag_t	1.28	0.87	-1.67	Ni_t	0.52	0.30	0.51
Au_s	1.03	0.97	-1.30	Pd_s	0.54	0.40	0.58
Au_t	1.29	1.51	-2.26	Pd_t	0.69	0.93	-0.05
Co_s	0.52	-0.60	1.39	Pt_s	0.17	0.27	0.90
Co_t	0.26	0.07	0.59	Pt_t	0.33	1.00	-0.14
Cu_s	0.57	-0.04	0.07	Rh_s	0.36	-0.08	1.06
Cu_t	0.97	0.44	-0.74	Rh_t	0.74	0.56	0.23
Fe_s	0.51	-0.78	1.54	Ru_s	0.22	-0.49	1.46
Fe_t	0.76	-0.47	1.31	Ru_t	0.37	0.19	0.60
Ir_s	-0.02	-0.16	1.62				
Ir_t	0.52	0.64	0.45				

Table S4 Using the data of table S1 the potential corresponding to each of the three distinct processes of the indirect mechanism (Eqn. 2) is given (in V) for all the 22 monometallic model surfaces studied.

Correlations between adsorption energies of methanol oxidation intermediates

The adsorption free energies of the MOR intermediates (Table S1) are linearly correlated with the adsorption energy of either CO or OH. The equations describing these linear relationships are of the $y = ax + b$ form, where the parameters a and b are calculated by fitting over all surfaces. The variable y represents the free energies of the MOR intermediates and x the adsorption free energy of CO or OH for species binding through a C or O atom, respectively. The fitted parameters a and b are summarized in table S5.

		a	b (eV)			a	b (eV)
O-bound	H_2COO	1.53	1.25	C-bound	CHOH	1.09	1.47
	CH_3O	0.99	0.32		$C(OH)_2$	0.88	1.38
	CHOO	0.90	0.06		COOH	0.72	0.92
	H_2COOH	0.97	0.81		CH_2OH	0.62	1.14
					COH	1.55	1.47
					CHO	0.84	0.93

Table S5 Fitted parameters describing linear relationships of the $y = ax + b$ form between the adsorption energies of the methanol oxidation intermediates and CO or OH.

As a specific example, the adsorption energy of H_2COOH is calculated as $\Delta G_{H_2COOH} = 0.97\ \Delta G_{OH} + 0.81$eV

Lattice constants for alloy structures

Table S6 summarizes the lattice constants a_0 of all the bulk $L1_2$ alloys mentioned in the paper.

	Pt_3Cu	Cu_3Pt	Cu_3Ir	Ir_3Cu	Pt_3Sn
a_0 (Å)	3.93	3.78	3.75	3.87	4.10

Table S6 Lattice constants of bulk $L1_2$ structures.

A dense real-space grid of spacing h = ~0.10Å was used for the optimization of lattice constants.

Evaluation of the Cu_3Pt and Pt_2Cu/Pt surfaces stability

We estimate the energy barrier for substitutional atomic diffusion by calculating the energy associated with swapping one Pt atom with an adjacent Cu atom ignoring any entropic contributions. More precisely, for $Cu_3Pt(AB)$ the barrier is calculated from the geometries shown in Fig. S1 as $E_{ab} = (E_a - E_b)$ = -0.29eV where E_a and E_b correspond to the total energy of the a and b structures of Fig. S1 respectively.

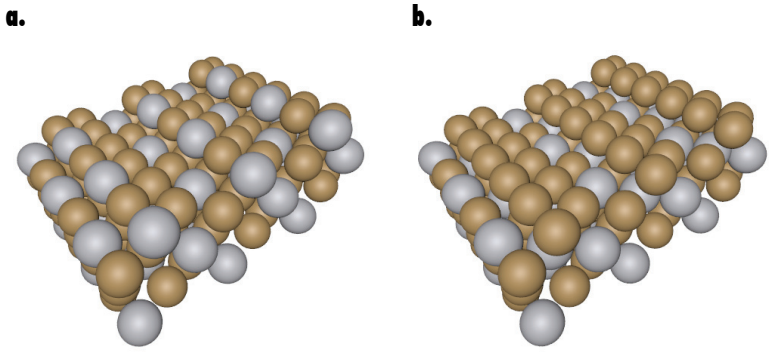

Fig. S1 Geometries used for the calculation of the barrier for substitutional atomic diffusion relevant to the $Cu_3Pt(AB)$ alloy. The unit cell is shown repeated three times along the x and y axes.

For Pt_2Cu/Pt, the energy barriers corresponding to three different possible atomic diffusion processes are calculated in a similar fashion using the geometries of Fig. S2. We calculate E_{ab} = -0.04eV, E_{ac} = -0.22eV and E_{ad} = -0.44eV

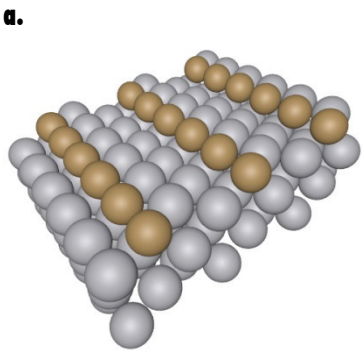

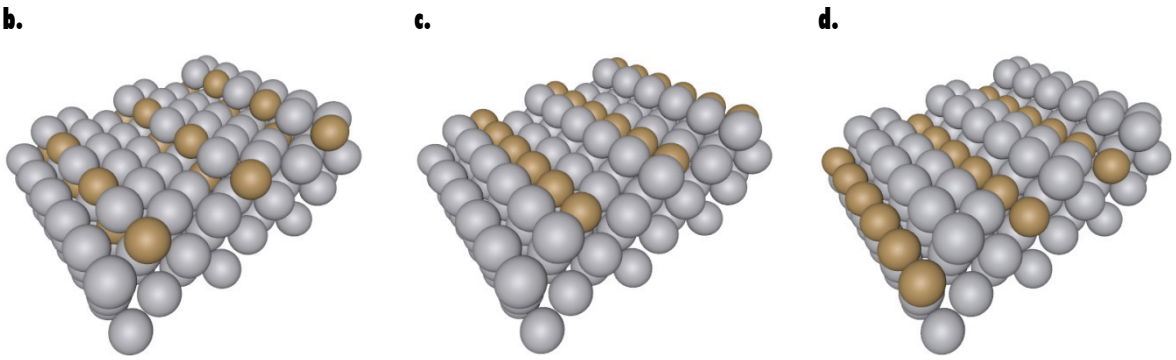

Fig. S2 Geometries used for the calculation of the barrier for substitutional atomic diffusion relevant to the Pt_2Cu/Pt alloy. The unit cell is shown repeated three times along the x and y axes.

For evaluating CO adsorption induced segregation effects we calculate the energy difference between the structures of Fig.2 with CO adsorbed. We then find E_{ab} = -0.96eV in the case of Cu_3Pt(AB). The negative value suggests that no such effects are relevant. However, for two out of the three Pt_2Cu/Pt alloys we find adsorption induced surface reconstruction to be potentially a problem after calculating with E_{ab} = 0.29, E_{ac} = 0.07 and E_{ad} = -0.39.

Free energy diagrams for the methanol oxidation reaction on Cu_3Pt

By using the adsorption energies of Table S2, we reconstruct the free energy diagram for the methanol oxidation reaction over Cu_3Pt.

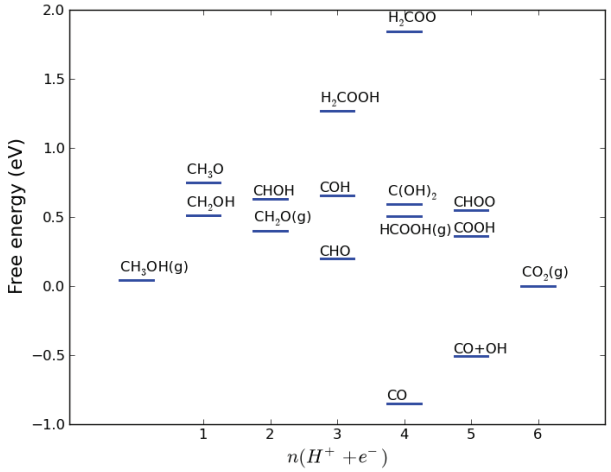

Fig. S3 Free energy diagram for the methanol oxidation reaction over Cu_3Pt.

Paper III

Atomic-scale modeling of particle size effects for oxygen reduction reaction on Pt

Tritsaris G. A., Greeley J., Rossmeisl J., Nørskov J. K. Submitted.

Atomic-scale modeling of particle size effects for the oxygen reduction reaction on Pt

G. A. Tritsaris[a,b] • email: george.tritsaris@fysik.dtu.dk

J. Greeley[c] • email: jgreeley@anl.gov

J. Rossmeisl[a] • email: jross@fysik.dtu.dk

J. K. Nørskov[b,d] • email: norskov@stanford.edu

[a]Center for Atomic-scale Materials Design, Department of Physics, Technical University of Denmark, DK 2800, Denmark

[b]Center for Interface Science and Catalysis, SLAC National Accelerator Laboratory, 2575 Sand Hill Road, Menlo Park, CA 94025, United States

[c]Center for Nanoscale Materials, Argonne National Laboratory, Argonne, IL 60439, United States

[d]Department of Chemical Engineering, Stanford University, Stanford, CA 94305, United States

Abstract

We estimate the activity of the oxygen reduction reaction on Pt nanoparticles of sizes of practical importance while explicitly accounting for the presence of surface irregularities and their effect on the activity of neighboring active sites. The proposed model reproduces the experimentally observed trends in both the specific and mass activities for particles in the range between 2-30 nm. The latter is shown to maximize for particles of a diameter in the range of 2-4nm. Our study demonstrates how an atomic-scale description of the surface microstructure is a key component in understanding particle size effects on the activity of catalytic nanoparticles.

Keywords Particle size effect - Oxygen electroreduction - Platinum catalysis - Low-coordinated active sites - Atomistic modeling

Electronic supplementary material The online version of this article contains supplementary material, which is available to authorized users.

1 Introduction

Several strategies have been employed for enhancing fuel cell (FC) catalysis, including the preparation of cathode catalysts which comprise dispersed nanoparticles of optimum surface-to-volume ratio [1,2]. In that case, the effect of a particle's size and shape on the rate of the oxygen reduction reaction (ORR) becomes of primary importance and the search for efficient and inexpensive catalysts coincides with the optimization of the particle's geometry. For Pt, although the existence of a maximum in mass activity versus particle size is now well established [3,4], efforts to elucidate the origin of such particle size effects are hindered by the lack of models for realistically describing the morphology of catalytic nanoparticles [5]. Traditionally, models of ideal truncated octahedrons have been assumed, but the importance of the effect of surface irregularities on the activity has been acknowledged only recently [6-9]. On the application level, the understanding and effective modeling of particle size effects is a requisite for the rational design and synthesis of new and efficient FC catalysts [10].

Here, we attempt to bring atom-level insight into the origin of particle size effects and the observed maximum in mass ORR activity on Pt. For that, we construct a model for nanoparticle catalysis which explicitly accounts for the defects present on a particle's surface as well as their effect on the activity of neighboring active sites. The agreement with experiment[1,4] highlights the importance of an accurate description of the population of these low-coordinated surface sites.

2 Particle model and computational details

Particles of truncated octahedra were modeled as Wulff constructions of (100) and (111) facets (Figure 1). A ratio between the respective surface free energies of $\gamma_{100} / \gamma_{111} = 1.189$ was used, calculated on the basis of the density functional theory (DFT) surface energies reported in the study of Vitos et al. [11]. Given that the equilibrium dissolution potential and the coordination number of dissolving atoms are correlated [12], every atom on the particle surface facets was considered to be an active site with

the exception of the edge and corner atoms, which are expected to dissolve in solution at low potentials. Two step sites were then assumed to be created for each dissolved atom. Moreover, recent advances in electron microscopy allowed for the direct observation of the atomic structure of the surface of nanoparticles [13,14], supporting the presence of defects in the form our particle model assumes. We ignore any effect of the support on the morphology of the particle[15], and we assume no surface restructuring during the ORR. The activity was averaged over all the different active sites. For the step sites, the activity of a (211) surface was used. The ORR activation energies corresponding to the (100), (111) and (211) surfaces were taken from Greeley et al. [16], estimated from a set of DFT calculated adsorption energies of key ORR intermediate species [17].

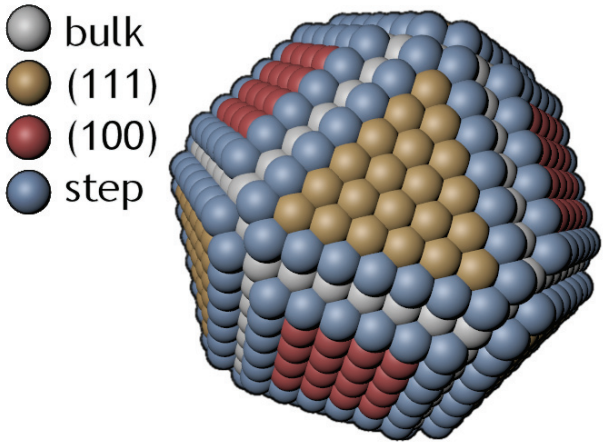

Fig. 1 Model particle of truncated octahedron shape with dissolved edges and corners. Differently colored atoms correspond to active sites of different activity.

Estimating the catalytic activity by simply averaging over a set of activities corresponding to extended surfaces assumes that the effect of steps on the activity of the neighboring sites (and vice versa) is negligible. We support this assumption by investigating the effect of adsorbate - adsorbate interactions [18] on the adsorption free energy of two ORR intermediates, O and OH. For that, we use semi-infinite model slabs describing fcc(544) surfaces: An fcc(544) surface comprises (111) terraces of 9 rows of atoms wide separated by monoatomic steps with the (100) orientation. The wide terrace allows for the calculation of adsorption energies for different distances from the step edge. This way the range of the effect of the step on the nearest active sites was estimated. These total energy calculations

were done with the GPAW package, a DFT implementation based on the projector-augmented wave (all electron, frozen core approximation) method [19], using real-space uniform grids [20]; see Supplementary Material for additional details. For the description of exchange and correlation, the RPBE functional was chosen [21]. Calculated adsorption energies were corrected with zero-point energy and entropic contributions [17].

3 Results and discussion

Figure 2a demonstrates how the adsorption free energy of O and OH changes with respect to the distance from a non-occupied step. Both will strongly bind on the step, a situation attributed to the low-coordination of the step atoms as suggested by the d-band model [18]. Step sites are thus expected to become occupied first. The effect of the step is shown to be localized in nature: Both of the adsorption energies quickly converge to the corresponding terrace values already at the distance of one atomic row. The effect of a half-occupied step by either O or OH on the adsorption free energy of the same adsorbate bound at different distances from the step is shown in Figure 2b. For each separation, the difference in adsorption energy between a half and a non-occupied step is plotted. Both adsorbates become destabilized when bound on a step or on the first adjacent atomic row when the step is already half-occupied, but no such an effect is observed for greater separations. For FC voltages of practical interest for the ORR (~0.9V), the expected surface coverage is ~1/3ML [22]. At this coverage, the ORR intermediates reside embedded in a half-dissociated water layer [23] with every two intermediate species separated by water molecules. Given that the step becomes occupied before any other site, the next atomic row to be occupied by ORR intermediate species is thus the second on which the step has no effect. Defects give rise to inactive step sites (poisoned by strongly bound ORR intermediates), but their presence has no effect on the activity of the adjacent facets.

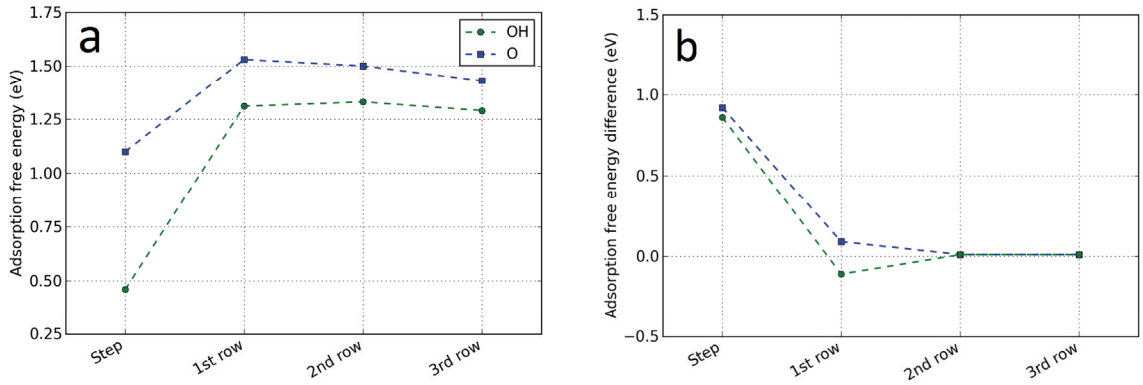

Fig. 2 (a) Adsorption free energy of two oxygen reduction reaction intermediates, O and OH, for different separations from a step. The energies are given with respect to gas-phase H_2O and H_2. The step is expected to become occupied before any other active site. (b) Difference in the adsorption free energy of O and OH between a half-occupied step with the same adsorbate and a non-occupied one. The effect of the step is shown not to extend further than one neighboring row of atoms.

After excluding communication between steps and facets we proceed to estimate the catalytic activity. In Figure 3, the calculated trends in specific activities i_s and mass activities i_m for the ORR are plotted against the particle surface area A_{Pt} for a set of particles with sizes of practical importance (2 - 30nm in diameter d_{Pt}). We calculate d_{Pt} as the average distance between every two opposite particle facets. A_{Pt} is calculated from as $A_{Pt} = 6 / (\rho_{Pt} \times d_{Pt})$ where ρ_{Pt} is the Pt density. The activities for Pt-black (A_{Pt} = ~5m^2/g_{Pt}) and Pt/C catalysts (A_{Pt} > 35m^2/g_{Pt}) at 0.9V and 60^{0}C determined via RDE-measurements in O_2-saturated 0.1M $HClO_4$ are also shown in Figure 3, taken from the work of Gasteiger et al. [1]. Both theoretically and experimentally determined activities are shown normalized with respect to the activity $i^{0,p}$ of the smallest particle of each set. The specific activities calculated with our model are also given normalized to the activity of a fcc(111) surface $i_s^{0,111}$. Figure 3 shows that our model captures the experimentally observed trends in both the specific and mass activity. The ratio between the activities of the biggest and smallest particle is calculated ~4. The maximum in mass activity is also reproduced, found for particle sizes in the range of A_{Pt} = 90 ± 20 m^2/g_{Pt} (d_{Pt} = 3 ± 1nm).

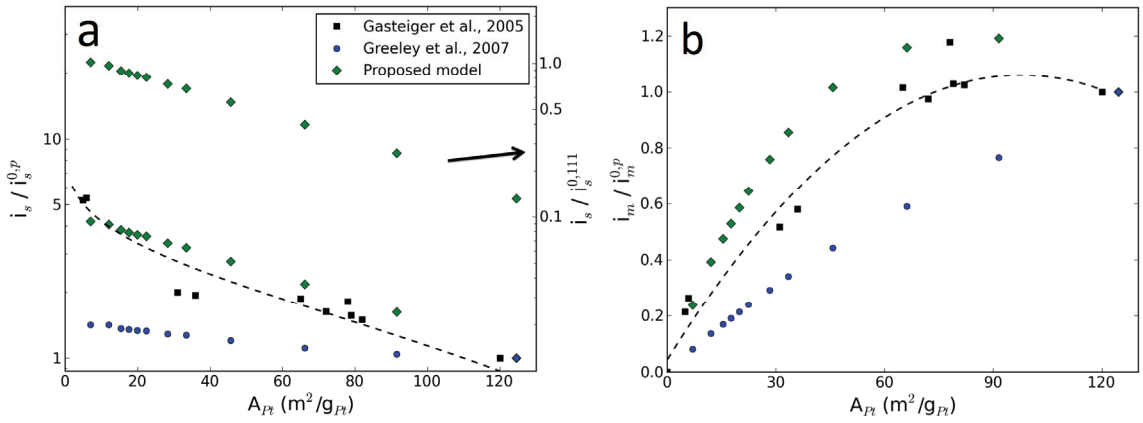

Fig. 3 (a) Specific activities i_s and (b) mass activities i_m for the oxygen reduction reaction on Pt versus particle surface area A_{Pt}. All activities are shown normalized with respect to the activity $i^{0,p}$ of the smallest particle of each data set. The specific activities calculated with our model are also given normalized to the activity of a fcc(111) surface $i_s^{0,111}$. The dashed lines serve as a guide to the eye for the experimental data points. The proposed model (diamonds) captures the experimental trends (squares, see also Figure 8 in Gasteiger et al.[1]) with a maximum in mass activity observed for A_{Pt} = 90 ± 20 m^2/g_{Pt}.

In our previous work [16] we constructed a similar particle model for describing particle size effects on the ORR activity of nanoparticles of different transition metals. One step active site is assumed for every edge atom dissolving. Although trends in specific activity are well captured by this simpler model, the absence of a maximum in mass activity (Figure 3b) and the quantitative agreement of the present model with experiments demonstrate the need for a more detailed description of the microscopic structure of the surface. For example, even better agreement with experiment is possible by assuming less than 100% edge dissolution but for simplicity, only two limiting cases are presented here.

The geometric model introduced corresponds to a mathematical one[24]. The fraction of the different active sites is only dependent on the number of atomic shells, which in turn is a function of the size (diameter) of the nanoparticle. The activity of a Pt nanoparticle is then estimated with the sole input of a set of theoretically estimated activities (or binding energies of reaction intermediates [16,18,17])

corresponding to the different facets and steps. There is no assumption in the model that limits its applicability to the study of ORR, and particle size effects on the rate of other reactions of interest to the operation of FCs [25] may also be studied with an appropriate set of facet/step activities.

The above analysis breaks down for particles of very small sizes ($d_{Pt} \leq$ ~2nm). Quantum-size effects render the use of reaction activities estimated on extended surfaces an invalid assumption. Moreover, although the model reproduces the experimentally measured activities (but for a factor) for d_{Pt} = 2 - 30nm, it cannot describe the significant increase in specific activity observed when extended Pt(111) surfaces are employed[1]. Normalizing to $i_s^{0,111}$, the model significantly overestimates the activity. We therefore stress that this study cannot explain the difference in specific activities between, for example, a 30 nm particle and an extended surface. More precise modeling of the particle's surface and careful consideration of the activity factors are possible directions for closing the gap.

The utilization of catalysts comprising octahedra nanoparticles has been proposed as an alternative route to achieving increased activity[2]. For a model particle of octahedron shape with dissolved edges and corners and ~30nm in diameter, the mass activity is calculated to double.

4 Conclusion

We have demonstrated the need for a detailed description of low-coordinated surface sites for understanding particle size effects. We constructed a model for nanoparticle catalysis which effectively captures the experimentally observed trends in both the specific and mass ORR activities on Pt. For FC voltages of practical interest for the ORR, dissolved edges and corners were shown to have only a local effect on the activity of adjacent active sites. The mass activity was verified to be maximized for particles of a diameter in the range of 2-4nm. The results allow us to deconvolute the origin of this maximum into two synergistic components: the presence of irregularities in nanoparticles and the structure sensitivity of the rate of the ORR.

Acknowledgements CAMD is funded by the Lundbeck Foundation. This work was supported by the Danish Center for Scientific Computing. Work at the Center for Nanoscale Materials at Argonne was

supported by the U.S. Department of Energy, Office of Basic Energy Sciences, under contract No. DE-AC02-06CH11357.

References

[1] Gasteiger H, Kocha S, Sompalli B, Wagner F (2005) Applied Catalysis B: Environmental 56:9-35.
[2] Gasteiger HA, Marković NM (2009) Science 324:48-49.
[3] Yano H, Inukai J, Uchida H, Watanabe M, Babu P, Kobayashi T, Chung J, Oldfield E, Wieckowski A (2006) Physical Chemistry Chemical Physics 8:4932-4939.
[4] Mukerjee S, McBreen J (1998) Journal of Electroanalytical Chemistry 448:163-171.
[5] Mayrhofer K, Blizanac B, Arenz M, Stamenkovic V, Ross P, Markovic N (2005) Journal of Physical Chemistry B 109:14433-14440.
[6] Dahl S, Logadottir A, Egeberg R, Larsen J, Chorkendorff I, Törnqvist E, Nørskov J (1999) Physical Review Letters 83:1814-1817.
[7] Lebedeva NP, Koper MTM, Herrero E, Feliu JM, van Santen RA (2000) Journal of Electroanalytical Chemistry 487:37-44.
[8] Nørskov JK, Bligaard T, Hvolbaek B, Abild-Pedersen F, Chorkendorff I, Christensen CH (2008) Chem. Soc. Rev. 37:2163-2171.
[9] Zambelli T, Wintterlin J, Trost J, Ertl G (1996) Science 273:1688-1690.
[10] Tian N, Zhou Z, Sun S (2008) Journal of Physical Chemistry C 112:19801-19817.
[11] Vitos L, Ruban A, Skriver H, Kollár J (1998) Surface Science 411:186-202.
[12] Greeley J (2010) Electrochimica Acta 55:5545-5550.
[13] Arenz M, Mayrhofer K, Stamenkovic V, Blizanac B, Tomoyuki T, Ross P, Markovic N (2005) Journal of the American Chemical Society 127:6819-6829.
[14] Gontard L, Chang L, Hetherington C, Kirkland A, Ozkaya D, Dunin-Borkowski R (2007) Angewandte Chemie - International Edition 46:3683-3685.
[15] Henry CR (1998) Surface Science Reports 31:231-325.
[16] Greeley J, Rossmeisl J, Hellman A, Nørskov J (2007) Zeitschrift fur Physikalische Chemie 221:1209-1220.
[17] Nørskov JK, Rossmeisl J, Logadottir A, Lindqvist L, Kitchin JR, Bligaard T, Jónsson H (2004) The Journal of Physical Chemistry B 108:17886-17892.
[18] Hammer B, Nørskov J (2000) Advances in Catalysis 45:71.
[19] Blöchl PE (1994) Phys. Rev. B 50:17953.
[20] Enkovaara J, Rostgaard C, Mortensen J, Chen J, Dułak M, Ferrighi L, Gavnholt J, Glinsvad C, Haikola V, Hansen H, Kristoffersen H, Kuisma M, Larsen A, Lehtovaara L, Ljungberg M, Lopez-Acevedo O, Moses P, Ojanen J, Olsen T, Petzold V, Romero N, Stausholm-Møller J, Strange M, Tritsaris G, Vanin M, Walter M, Hammer B, Häkkinen H, Madsen G, Nieminen R, Nørskov J, Puska M, Rantala T, Schiøtz J, Thygesen K, Jacobsen K (2010) Journal of Physics Condensed Matter 22.
[21] Hammer B, Hansen LB, Nørskov JK (1999) Phys. Rev. B 59:7413.
[22] Tripković V, Skúlason E, Siahrostami S, Nørskov JK, Rossmeisl J (2010) Electrochimica Acta 55:7975-7981.
[23] Ogasawara H, Brena B, Nordlund D, Nyberg M, Pelmenschikov A, Pettersson LGM, Nilsson A (2002) Phys. Rev. Lett. 89:276102.
[24] Van Hardeveld R, Hartog F (1969) Surface Science 15:189-230.
[25] Maillard F, Martin M, Gloaguen F, Léger J (2002) Electrochimica Acta 47:3431-3440.

Atomic-scale understanding of particle size effects for the oxygen reduction reaction on Pt

G. A. Tritsaris[a,b], J. Greeley[c], J. Rossmeisl[a], J. K. Nørskov[b,d]

Center for Atomic-scale Materials Design, Department of Physics, Technical University of Denmark, DK 2800, Denmark[a]

Center for Interface Science and Catalysis, SLAC National Accelerator Laboratory, 2575 Sand Hill Road, Menlo Park, CA 94025, United States[b]

Center for Nanoscale Materials, Argonne National Laboratory, Argonne, IL 60439, United States[c]

Department of Chemical Engineering, Stanford University, Stanford, CA 94305, United States[d]

Supplementary material includes particle model and computational details, surfaces activities, binding energies and additional references.

Particle model details

Figure S1 shows the fraction of step, (111) and (100) surface sites versus particle diameter for the particle model of Figure 1.

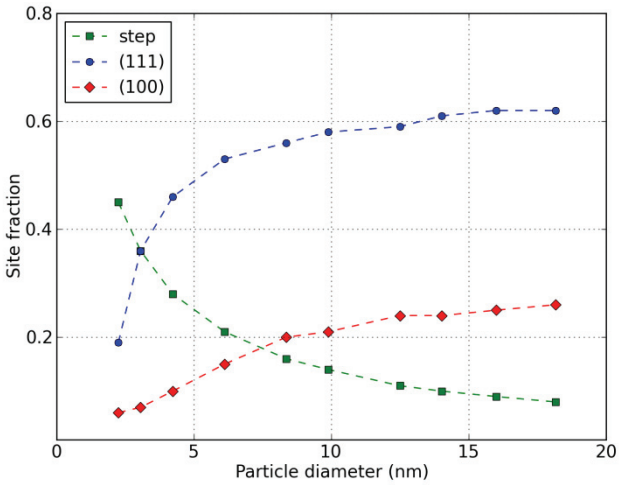

Fig. S1 Population of step, (111) and (100) surface sites versus particle diameter.

Computational details

Extended slabs were constructed for modeling the fcc(544) surface. The slabs comprise three atomic layers thick in the direction perpendicular to the (100) direction, surrounded with 13Å of vacuum in a (1x2) simulation cell. Total energy calculations are done with the GPAW program package, a DFT

implementation based on the projector-augmented wave (all electron, frozen core approximation) method [1], using real-space uniform grids and multigrid methods [2,3]. For the description of exchange and correlation, the RPBE functional [4] is chosen and a Monkhorst-Pack mesh is used for k-space integration resulting in a set of 4 special points for the sampling of the irreducible Brillouin zone. The grid spacing is set to $h = 0.18$Å as a tradeoff between computational efficiency and accuracy and a stencil of $O(h^8)$ accuracy is used to discretize the kinetic energy Laplacian. The energies are converged to 10^{-4} eV per valence electron. For structure optimization, the top 3 slab layers were relaxed by the minimization of all inter-atomic forces to the upper limit of 0.045 eV/Å.

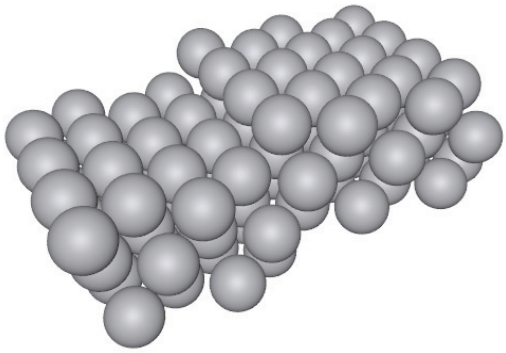

Fig. S2 Slab model of a fcc(544) surface.

Calculated adsorption energies are given with reference to gas-phase H_2O and H_2 energies, $\Delta E_{H_2O(g)} = -14.02$eV and $\Delta E_{H_{2(g)}} = -6.72$eV, corrected with zero-point energy and entropy contributions (see also the work of Nørskov et al. [5]). Thermal corrections to enthalpy are assumed negligible. The corrections are taken from the work of Ferrin et al. [6].

Activities of extended surfaces

Table S1 summarizes the oxygen reduction reaction overpotential estimated for the (211), (111) and (100) extended surfaces, taken from our previous work [7].

	(211) step	(111) facet	(100) facet
Overpotential (V)	1.06	0.46	0.44

Table S1. Estimated oxygen reduction reaction overpotentials.

Adsorption free energies of oxygen reduction intermediates

The adsorption free energies ΔG of the O and OH intermediates used for making the plots shown in Fig. 3 are summarized in Table S2.

	Step coverage	Step	1st row	2nd row	3rd row
ΔG_O	non-occupied	1.10	1.53	1.50	1.43
	half-occupied	2.02	1.62	1.51	1.44
$\Delta\Delta G_O$		0.92	0.09	0.01	0.01
ΔG_{OH}	non-occupied	0.46	1.31	1.33	1.29
	half-occupied	1.32	1.20	1.34	1.30
$\Delta\Delta G_O$		0.86	-0.11	0.01	0.01

Table S2. Adsorption free energies of O and OH on Pt(544).

Additional references

[1] P. E. Blöchl, Phys. Rev. B **50**, 17953 (1994).
[2] J. J. Mortensen, L. B. Hansen, and K. W. Jacobsen, Phys. Rev. B **71**, 035109 (2005).
[3] J. Enkovaara, C. Rostgaard, J. Mortensen, J. Chen, M. Dułak, L. Ferrighi, J. Gavnholt, C. Glinsvad, V. Haikola, H. Hansen, H. Kristoffersen, M. Kuisma, A. Larsen, L. Lehtovaara, M. Ljungberg, O. Lopez-Acevedo, P. Moses, J. Ojanen, T. Olsen, V. Petzold, N. Romero, J. Stausholm-Møller, M. Strange, G. Tritsaris, M. Vanin, M. Walter, B. Hammer, H. Häkkinen, G. Madsen, R. Nieminen, J. Nørskov, M. Puska, T. Rantala, J. Schiøtz, K. Thygesen, and K. Jacobsen, Journal of Physics Condensed Matter **22**, (2010).
[4] B. Hammer, L. B. Hansen, and J. K. Nørskov, Phys. Rev. B **59**, 7413 (1999).
[5] J. K. Nørskov, J. Rossmeisl, A. Logadottir, L. Lindqvist, J. R. Kitchin, T. Bligaard, and H. Jónsson, The Journal of Physical Chemistry B **108**, 17886-17892 (2004).
[6] P. Ferrin, A. U. Nilekar, J. Greeley, M. Mavrikakis, and J. Rossmeisl, Surface Science **602**, 3424-3431 (2008).
[7] J. Greeley, J. Rossmeisl, A. Hellman, and J. Nørskov, Zeitschrift Fur Physikalische Chemie **221**, 1209-1220 (2007).
[8] T. S. Ahmadi, Z. L. Wang, T. C. Green, A. Henglein, and M. A. El-Sayed, Science **272**, 1924-1925 (1996).
[9] C. Burda, X. Chen, R. Narayanan, and M. El-Sayed, Chemical Reviews **105**, 1025-1102 (2005).
[10] P. Ferreira, G. La O', Y. Shao-Horn, D. Morgan, R. Makharia, S. Kocha, and H. Gasteiger, Journal of the Electrochemical Society **152**, (2005).
[11] K. Kinoshita, Journal of the Electrochemical Society **137**, 845-848 (1990).
[12] S. Lee, S. Chen, J. Suntivich, K. Sasaki, R. Adzic, and Y. Shao-Horn, Journal of Physical Chemistry Letters **1**, 1316-1320 (2010).
[13] N. Markovic, H. Gasteiger, and P. Ross, Journal of the Electrochemical Society **144**, 1591-1597 (1997).
[14] K. Mayrhofer, B. Blizanac, M. Arenz, V. Stamenkovic, P. Ross, and N. Markovic, Journal of Physical Chemistry B **109**, 14433-14440 (2005).
[15] V. Stamenkovic, N. M. Markovic, and P. N. Ross, Journal of Electroanalytical Chemistry **500**, 44-51 (2001).
[16] C. Wang, H. Daimon, T. Onodera, T. Koda, and S. Sun, Angewandte Chemie - International Edition **47**, 3588-3591 (2008).